

MOLTEN SALT NANOMATERIALS FOR THERMAL ENERGY STORAGE AND
CONCENTRATED SOLAR POWER APPLICATIONS

A Dissertation

by

DONGHYUN SHIN

Submitted to the Office of Graduate Studies of
Texas A&M University
in partial fulfillment of the requirements for the degree of

DOCTOR OF PHILOSOPHY

August 2011

Major Subject: Mechanical Engineering

Molten Salt Nanomaterials for Thermal Energy Storage and Concentrated Solar Power

Applications

Copyright 2011 Donghyun Shin

MOLTEN SALT NANOMATERIALS FOR THERMAL ENERGY STORAGE AND
CONCENTRATED SOLAR POWER APPLICATIONS

A Dissertation

by

DONGHYUN SHIN

Submitted to the Office of Graduate Studies of
Texas A&M University
in partial fulfillment of the requirements for the degree of

DOCTOR OF PHILOSOPHY

Approved by:

Chair of Committee,	Debjyoti Banerjee
Committee Members,	Je Han
	Raymundo Arroyave
	Jorge Alvarado
Head of Department,	Jerald Caton

August 2011

Major Subject: Mechanical Engineering

ABSTRACT

Molten Salt Nanomaterials for Thermal Energy Storage and Concentrated Solar Power
Applications. (August 2011)

Donghyun Shin, B.S., Hanyang University; M.S., Ohio University

Chair of Advisory Committee: Dr. Debjyoti Banerjee

The thermal efficiency of concentrated solar power (CSP) system depends on the maximum operating temperature of the system which is determined by the operating temperature of the TES device. Organic materials (such as synthetic oil, fatty acid, or paraffin wax) are typically used for TES. This limits the operating temperature of CSP units to below 400 °C. Increasing the operating temperature to 560 °C (i.e., the creeping temperature of stainless steel), can enhance the theoretical thermal efficiency from 54% to 63%. However, very few thermal storage materials are compatible for these high temperatures.

Molten salts are thermally stable up to 600 °C and beyond. Using the molten salts as the TES materials confers several benefits, which include: (1) Higher operating temperature can significantly increase the overall cycle efficiency and resulting costs of power production. (2) Low cost of the molten salt materials can drastically reduce the cost. (3) The molten salts, which are environmentally safe, can also reduce the potential environmental impact. However, these materials suffer from poor thermo-physical properties. Impregnating these materials with nanoparticles can enhance these properties.

Solvents doped with nanoparticles are termed as nanofluids. Nanofluids have been reported in the literature for the anomalous enhancement of their thermo-physical properties. In this study, the poor thermal properties of the molten salts were enhanced dramatically on mixing with nanoparticles. For example the specific heat capacity of these molten salt eutectics was found to be enhanced by as much as $\sim 26\%$ on mixing with nanoparticles at a mass fraction of $\sim 1\%$. The resultant properties of these nanomaterials were found to be highly sensitive to small variations in the synthesis protocols.

Computational models were also developed in this study to explore the fundamental transport mechanisms on the molecular scale for elucidating the anomalous enhancements in the thermo-physical properties that were measured in these experiments.

This study is applicable for thermal energy storage systems utilized for other energy conversion technologies – such as geothermal energy, nuclear energy and a combination of energy generation technologies.

DEDICATION

To my wife

ACKNOWLEDGEMENTS

I would like to thank my committee chair, Dr. Debjyoti Banerjee, and my committee members, Dr. Je Han, Dr. Raymundo Arroyave, and Dr. Jorge Alvarado, for their guidance and support throughout the course of this research.

I would like to thank Dr. Frederic Best and Dr. Michael Schuller for their contribution to the collaborative project sponsored by the Department of Energy (DOE) Solar Energy Technology Program (SETP) for Concentrated Solar Power (CSP) that made this work possible. In addition, I would like to acknowledge the collaboration with the members of their research group (particularly with Mr. Darren Mallek and Mr. Mathew Betts) during the initial phase of the project when we jointly explored and accessed the Differential Scanning Calorimeter (DSC) instruments available on campus. This proved to be a futile exercise but nonetheless was an educational endeavor for me.

I also acknowledge the Material Characterization Facility (MCF) and the Microscopy and Image Center (MIC) at Texas A&M University for access to their facilities. The FE-SEM acquisition was supported by the NSF grant DBI-0016835, the Vice President for Research Office, and the Texas Engineering Experiment Station. I also acknowledge the National Nano-Technology Infrastructure Network (NNIN) for access to the facility.

Thanks also go to my friends and colleagues and the department faculty and staff for making my time at Texas A&M University a great experience.

Finally, thanks to my mother and father for their encouragement and to my wife for her patience and love.

NOMENCLATURE

PV	Photovoltaic
CSP	Concentrating Solar Power
TES	Thermal Energy Storage
HTF	Heat Transfer Fluid
EG	Ethylene Glycol
MD	Molecular Dynamics Simulation
CNT	Carbon Nanotube
SDS	Sodium Dodecyl Sulfonate
DSC	Differential Scanning Calorimeter
SEM	Scanning Electron Microscope
TEM	Transmission Electron Microscope
LFA	Laser Flash Apparatus
ASTM	American Standard Test Method
\dot{Q}	Heat Transfer Rate
ρ_{np}	Density of Nanoparticle
ρ_b	Density of Base Material
ρ_c	Density of Special Sub-Structure
V_{np}	Volume Fraction of Nanoparticle
V_b	Volume Fraction of Base Material
V_c	Volume Fraction of Special Sub-Structure

$C_{p,np}$	Specific Heat Capacity of Nanoparticle
$C_{p,b}$	Specific Heat Capacity of Base Material
$C_{p,c}$	Specific Heat Capacity of Special Sub-Structure
$C_{p,t}$	Specific Heat Capacity of Nanomaterial
A_s	Interfacial Area
R_b	Interfacial Thermal Resistance
T_s	Temperature at Surface
T_f	Temperature of Fluid
τ	Time Constant
k_{eff}	Effective Thermal Conductivity
k_b	Thermal Conductivity of Base Material
k_p	Thermal Conductivity of Particle
α_t	Thermal Diffusivity of Nanomaterial
α_b	Thermal Conductivity of Base Material
d	Diameter

TABLE OF CONTENTS

	Page
ABSTRACT	iii
DEDICATION	v
ACKNOWLEDGEMENTS	vi
NOMENCLATURE	viii
TABLE OF CONTENTS	x
LIST OF FIGURES	xii
LIST OF TABLES	xxi
1. INTRODUCTION	1
1.1 Concentrating Solar Power System: Solar Thermal Energy Storage ...	2
1.2 Molten Salts	3
1.3 Nanomaterials: Nanofluids and Nanocomposites	4
1.4 Nanomaterials: Thermal Conductivity and Specific Heat Capacity	4
1.5 Nanomaterials: Interfacial Thermal Resistance	9
1.6 Molecular Dynamics Simulation	10
1.7 Objective of the Study	11
1.8 Motivation of the Study	11
1.9 Significance of the Study	12
1.10 Summary	13
2. COMPUTATIONAL STUDY	15
2.1 Molecular Dynamics Simulation	15
2.2 Interfacial Thermal Resistance	17
2.3 Size of Nanotube and Nanoparticle	19
2.4 Simulation Setup and Procedure (for Carbon Nanotube)	22
2.5 Simulation Setup and Procedure (for Silica Nanoparticle)	25
3. COMPUTATIONAL RESULTS AND DISCUSSIONS	29
3.1 Interfacial Thermal Resistance and CNT Size Limit	29

	Page
3.2 Interfacial Thermal Resistance and Silica Size Limit	38
3.3 Summary	42
4. EXPERIMENTAL STUDY	44
4.1 Synthesis of Molten Salt Nanomaterials	44
4.2 Specific Heat Capacity Measurement	45
4.3 Electron Microscopy Analysis	47
4.4 Thermal Conductivity Measurement.....	47
5. EXPERIMENTAL RESULTS AND DISCUSSIONS	49
5.1 SiO ₂ / BaCl ₂ -NaCl-CaCl ₂ -LiCl Nanomaterial	49
5.2 SiO ₂ / Li ₂ CO ₃ -K ₂ CO ₃ Nanomaterial	51
5.3 Discussions: Specific Heat Capacity of Nanomaterial.....	68
5.4 SiO ₂ / Li ₂ CO ₃ -K ₂ CO ₃ Nanomaterial with Different Composition.....	77
5.5 Thermal Conductivity Results.....	97
5.6 Discussions: Thermal Conductivity of Nanomaterial	102
5.7 New Nanomaterial Synthesis Method.....	105
6. CONCLUSIONS	151
REFERENCES	156
APPENDIX A	165
APPENDIX B	167
APPENDIX C	173
APPENDIX D	174
VITA	176

LIST OF FIGURES

	Page
Figure 1 The simulation domain used in this study. It consists of a single walled (5,5) carbon nanotube (CNT) lattice consisting of 400 Carbon atoms and the eutectic of Li_2CO_3 and K_2CO_3 (9000 atoms).	24
Figure 2 The simulation domain used in this study. It consists of a silica nanoparticle consisting of 234 atoms and the eutectic of Li_2CO_3 and K_2CO_3 (7200 atoms).	27
Figure 3 Plot of temperature decay of the CNT as a function of time.....	32
Figure 4 Semi-log graph of the temperature difference between the CNT and the molten salt. Inverse of the slope is the time constant required to compute the interfacial thermal resistance. (Equation 6).....	33
Figure 5 The interfacial thermal resistance between the CNT and the molten salt. No significant difference was observed for the variations in the values of the different parameters such as the initial temperature of the nanoparticle, the number of the atoms, and the size of the CNT	34
Figure 6 Density plot of the CNT / molten salt nanofluid	35
Figure 7 Spatial distribution of atomic concentration of different elements within the simulation domain which contains CNT of 6.97Å diameter	36
Figure 8 Temperature decay of the silica nanoparticle as a function of time.....	39
Figure 9 The interfacial thermal resistance between the silica nanoparticle and the molten salt. No significant difference was observed for the predicted results for variations in the size of the silica nanoparticle. The initial temperature difference ranged from 500 ~ 700 K.....	40
Figure 10 The optimum size of the silica nanoparticle was computed using Equation (12) and was predicted by this numerical model to be 22 ~ 26 nm.....	41
Figure 11 Schematic showing the procedure to synthesize eutectic salt nanomaterial	45

	Page
Figure 12 Variation of specific heat capacity with temperature (155 °C ~ 315 °C) for pure eutectic salt of $\text{BaCl}_2\text{-NaCl-CaCl}_2\text{-LiCl}$ and the corresponding SiO_2 nanocomposite samples [37].....	52
Figure 13 Variation of specific heat capacity with temperature (495 °C ~ 555 °C) for pure eutectic salt of $\text{BaCl}_2\text{-NaCl-CaCl}_2\text{-LiCl}$ and the corresponding SiO_2 nanocomposite samples [37].....	54
Figure 14 SEM image of $\text{SiO}_2/\text{BaCl}_2\text{-NaCl-CaCl}_2\text{-LiCl}$ nanomaterial before melting in the DSC. The average diameter of SiO_2 nanoparticles is ~26 nm. The nanoparticles are uniformly dispersed and no agglomeration is observed [37].	56
Figure 15 SEM image of $\text{SiO}_2/\text{BaCl}_2\text{-NaCl-CaCl}_2\text{-LiCl}$ nanomaterial after repeated thermal cycling involving melting and solidification in the DSC. The average diameter of SiO_2 nanoparticles is ~27 nm. The nanoparticles are uniformly dispersed and no agglomeration is observed after repeated thermal cycling involving melting and solidification in the DSC. A special network substructure is observed in the eutectic. The substructure seems to interconnect the SiO_2 nanoparticles, thus forming an interconnected network (“percolation network”) [37].	57
Figure 16 SEM image of the pure eutectic salt of $\text{BaCl}_2\text{-NaCl-CaCl}_2\text{-LiCl}$ after repeated thermal cycling involving melting and solidification in the DSC. A special substructure, which was shown in the nanomaterial (Figure 15), was not observed in the pure material [37]	58
Figure 17 Variation of specific heat capacity with temperature (355 °C ~ 495 °C) for pure eutectic salt of $\text{Li}_2\text{CO}_3\text{-K}_2\text{CO}_3$ and the corresponding SiO_2 nanocomposites. The average specific heat capacity of nanocomposite was enhanced by 11 ~ 14 % over that of the pure molten salt eutectic [36]	60
Figure 18 Variation of the specific heat capacity with temperature (525 °C ~ 555 °C) for pure eutectic salt samples of $\text{Li}_2\text{CO}_3\text{-K}_2\text{CO}_3$ and the corresponding SiO_2 nanofluids samples. The average specific heat capacity of the nanofluid samples was enhanced by 19 ~ 24 % over that of the pure molten salt eutectic [36]	62
Figure 19 SEM image of pure molten salt sample [36]	65

Figure 20 SEM images of $\text{SiO}_2/\text{Li}_2\text{CO}_3\text{-K}_2\text{CO}_3$ nanomaterial, which showed the enhanced specific heat capacity at solid phase and at liquid phase. It was observed that the molten salt eutectic formed a very special structure resembling weave pattern (“percolation network”). This structure is expected to play an important role for the enhancement of the specific heat capacity of nanomaterial [36]	66
Figure 21 Scanning Electron Microscopy (SEM) image of silica nanoparticles in the $\text{SiO}_2/\text{Li}_2\text{CO}_3\text{-K}_2\text{CO}_3$ nanomaterial after thermal cycling in the DSC for multiple times. The image shows that the nanoparticles were not agglomerated and the nominal size of the nanoparticle is 2~20 nm. The sub-structures of lighter color seem to engulf the nanoparticles and form an interconnected network (“percolation network”) [36].	67
Figure 22 (a) Backscattered electron microscopy image of $\text{SiO}_2/\text{Li}_2\text{CO}_3\text{-K}_2\text{CO}_3$. (b) A binary image obtained from (a). (c) A histogram of pixel distribution derived from (b)	74
Figure 23 Plot of calculated value of effective specific heat capacity of nanomaterials for parametric variation in the specific heat capacity of the modified structure using Equation (16). Blue dotted line represents experimentally measured value of the specific heat capacity of nanomaterial and the red line represents the estimated (calculated value) of the effective specific heat capacity of nanomaterial, based on Equation (15).....	74
Figure 24 Plot of molar specific heat capacity as a function of temperature for pure molten salt eutectic and the corresponding silica nanomaterial (nanofluid). The plotted results were obtained from experimental measurements	76
Figure 25 (a) The specific heat capacity of $\text{Li}_2\text{CO}_3\text{-K}_2\text{CO}_3$ salt mixture can be classified into three distinct regions: low C_p region (A), transition region (B), and high C_p region (C). (b) Plot for variation of specific heat capacity with temperature in the transition region shows dramatic decrease in specific heat capacity with temperature and the variability of the measurements is also large (as represented by the error bars in Figure 25a). (c) Plot for the variation of specific heat capacity with temperature for the low C_p region ($\sim 1.6 \text{ J/g-K}$) and is observed to be almost invariant with temperature. (d) Plot for the specific heat capacity with temperature in the high C_p region ($\sim 2.8 \text{ J/gK}$) and is observed to increase significantly with temperature.....	78

	Page
Figure 26 Molar specific heat capacity values derived from Figure 25	79
Figure 27 Variation of specific heat capacity with temperature for (a) solid phase, and (b) liquid phase. The samples tested included pure salt mixture (Li_2CO_3 : K_2CO_3 for 46:54 molar ratio) and the nanomaterial at 1% mass fraction of SiO_2	84
Figure 28 Variation of specific heat capacity with temperature for (a) solid phase, and (b) liquid phase. The samples tested included pure salt mixture (Li_2CO_3 : K_2CO_3 for 54:46 molar ratio) and the nanomaterial at 1% mass fraction of SiO_2	85
Figure 29 Variation of specific heat capacity with temperature for (a) solid phase, and (b) liquid phase. The samples tested included pure salt mixture (Li_2CO_3 : K_2CO_3 for 62:38 molar ratio) and the nanomaterial at 1% mass fraction of SiO_2 [36].	85
Figure 30 Variation of specific heat capacity with temperature for (a) solid phase, and (b) liquid phase. The samples tested included pure salt mixture (Li_2CO_3 : K_2CO_3 for 66:34 molar ratio) and the nanomaterial at 1% mass fraction of SiO_2	86
Figure 31 Variation of specific heat capacity with temperature for (a) solid phase, and (b) liquid phase. The samples tested included pure salt mixture (Li_2CO_3 : K_2CO_3 for 70:30 molar ratio) and the nanomaterial at 1% mass fraction of SiO_2	86
Figure 32 Variation of specific heat capacity with temperature for (a) solid phase, and (b) liquid phase. The samples tested included pure salt mixture (Li_2CO_3 : K_2CO_3 for 78:22 molar ratio) and the nanomaterial at 1% mass fraction of SiO_2	87
Figure 33 Variation in the specific heat capacity with composition of the molten salt (Li_2CO_3 - K_2CO_3) for (a) solid phase; and (b) for liquid phase. The molar ratio of Li_2CO_3 : K_2CO_3 was changed from 46:54 to 78:22. The SiO_2 mass concentration was fixed at 1% for the synthesized nanomaterials	87

Figure 34 (a) Microstructure of pure molten salt, whose composition between Li_2CO_3 and K_2CO_3 is 46:54 by molar ratio. (b) Microstructure of corresponding molten salt nanomaterials (SiO_2 nanoparticle at 1% mass concentration in Li_2CO_3 - K_2CO_3 base salt), whose molten salt composition is 46:54 by molar ratio. It was observed that significant agglomeration of nanoparticles exists in these nanomaterial samples	90
Figure 35 (a) Microstructure of pure molten salt, whose composition between Li_2CO_3 and K_2CO_3 is 54:46 by molar ratio. (b) Microstructure of molten salt nanomaterials (SiO_2 nanoparticle at 1% mass concentration in Li_2CO_3 - K_2CO_3 base salt), whose molten salt composition is 54:46 by molar ratio. It was observed that significant agglomeration of nanoparticles exists in these nanomaterial samples	91
Figure 36 (a) Microstructure of pure molten salt, whose composition between Li_2CO_3 and K_2CO_3 is 70:30 by molar ratio. (b) Microstructure of molten salt nanomaterials (SiO_2 nanoparticle at 1% mass concentration in Li_2CO_3 - K_2CO_3 base salt), whose molten salt composition is 70:30 by molar ratio. Similar to the nanomaterial, whose molten salt composition is 62:38 with 26 % enhancement in specific heat capacity, this nanomaterial was also observed to develop special sub-structures resembling thorn-like shapes. The specific heat capacity was also enhanced by 15 % for this sample compared to that of the base molten salt (70:30).....	91
Figure 37 (a) Microstructure of pure molten salt, whose composition between Li_2CO_3 and K_2CO_3 is 78:22 by molar ratio. (b) Microstructure of molten salt nanomaterials (SiO_2 nanoparticle at 1% mass concentration in Li_2CO_3 - K_2CO_3 base salt), whose molten salt composition is 78:22 by molar ratio. It was observed that significant agglomeration of nanoparticles exists in these nanomaterial samples	92
Figure 38 SEM images of molten salt nanomaterials (SiO_2 nanoparticle at 1% mass concentration in Li_2CO_3 - K_2CO_3 base salt), whose molten salt composition is 78:22 by molar ratio (Figure 32). The formation of special sub-structure was also observed for these nanomaterial samples. No agglomeration of nanoparticles was observed.....	93
Figure 39 Comparison of the specific heat capacity measurements of the base material of lithium carbonate and potassium carbonate (62:38 molar ratio) with that of the nanocomposite (synthesized by addition of SiO_2 nanoparticles at a mass concentration of 1%)	98

Figure 40 Comparison of the thermal diffusivity values of the pure eutectic of lithium carbonate and potassium carbonate (62:38 molar ratio) with that of the nanocomposite (synthesized by addition of SiO_2 nanoparticles at a mass concentration of 1%)	99
Figure 41 Comparison of the thermal conductivity values of the pure eutectic of lithium carbonate and potassium carbonate (62:38 molar ratio) with that of the nanocomposite (synthesized by addition of nanoparticles at a mass concentration of 1%). Theoretical estimates using the Maxwell-Garnett model [47] and the Hamilton-Crosser model [58] are plotted for comparison (This is discussed in section 5.6.)	100
Figure 42 Schematic showing new procedure to synthesize molten salt nanomaterial by evaporation technique in order to prevent boiling of water during drying process (separation method)	106
Figure 43 Image of dry amorphous powder of $\text{SiO}_2/\text{Li}_2\text{CO}_3\text{-K}_2\text{CO}_3$ nanomaterial (at mass concentration of 1.5 %) after the evaporation was completed. The image shows coarse amorphous powder (Type-A) and fine amorphous powder (Type-B)	109
Figure 44 Variation of specific heat capacity with temperature (355 °C ~ 495 °C) for $\text{SiO}_2/\text{Li}_2\text{CO}_3\text{-K}_2\text{CO}_3$ nanocomposites.....	110
Figure 45 Variation of specific heat capacity of $\text{SiO}_2/\text{Li}_2\text{CO}_3\text{-K}_2\text{CO}_3$ nanofluids with temperature (525 °C ~ 555 °C). The average specific heat capacity of Type-B nanofluid was enhanced significantly over that of the pure molten salt eutectic, while no enhancement of specific heat capacity was observed for Type-A nanofluid.....	113
Figure 46 SEM images of Type-A $\text{SiO}_2/\text{Li}_2\text{CO}_3\text{-K}_2\text{CO}_3$ nanomaterial (coarse powder samples).....	117
Figure 47 SEM images of Type-B $\text{SiO}_2/\text{Li}_2\text{CO}_3\text{-K}_2\text{CO}_3$ nanomaterial (fine powder samples), which showed the anomalously enhanced specific heat capacity at solid phase and at liquid phase. It was observed that the molten salt eutectic formed a very special structure resembling a weave-shaped pattern. This structure is potentially responsible for the anomalous enhancement of the specific heat capacity of Type-B nanomaterial, especially in the liquid phase (nanofluids)	118

	Page
Figure 48 Transmission Electron Micrograph (TEM) of silica nanoparticles in the Type-B samples of $\text{SiO}_2/\text{Li}_2\text{CO}_3\text{-K}_2\text{CO}_3$ nanomaterial after thermal cycling in the DSC involving multiple melting and solidification. The image shows that the nanoparticles are not agglomerated and the nominal size of the nanoparticles is 2~20 nm	119
Figure 49 Image of dry amorphous powder of $\text{MgO}/\text{Li}_2\text{CO}_3\text{-K}_2\text{CO}_3$ nanomaterial (at mass concentration of 1.0 %) after complete evaporation during the drying process. The image shows the formation of coarse amorphous powder (Type-A) and fine amorphous powder (Type-B)	120
Figure 50 Variation of specific heat capacity with temperature (355 °C ~ 495 °C) for $\text{MgO}/\text{Li}_2\text{CO}_3\text{-K}_2\text{CO}_3$ nanocomposites. The average specific heat capacity of both nanocomposites were enhanced by 2 ~ 17 % over that of the pure molten salt eutectic	122
Figure 51 Variation of specific heat capacity temperature (525 °C ~ 555 °C) for $\text{MgO}/\text{Li}_2\text{CO}_3\text{-K}_2\text{CO}_3$ nanofluids	125
Figure 52 SEM images of Type-A $\text{MgO}/\text{Li}_2\text{CO}_3\text{-K}_2\text{CO}_3$ nanomaterial (coarse powder samples).....	129
Figure 53 SEM images of Type-B samples of $\text{MgO}/\text{Li}_2\text{CO}_3\text{-K}_2\text{CO}_3$ nanomaterial (fine powder samples), which showed the anomalously enhanced specific heat capacity for the liquid phase. It was observed that the molten salt eutectic formed an interconnected network of needle-shaped micron-scale sub-structures (percolation network). This percolation network is expected to be responsible for the anomalous enhancement of the specific heat capacity of Type-B nanomaterial (nanofluid) samples.....	130
Figure 54 Transmission Electron Microscopy (TEM) image of MgO nanoparticles in the Type-B samples of $\text{MgO}/\text{Li}_2\text{CO}_3\text{-K}_2\text{CO}_3$ nanomaterial after thermal cycling in the DSC. It is observed that the nanoparticles were not agglomerated and the nominal size of the nanoparticles is ~20 nm....	131
Figure 55 Image of dry amorphous powder of $\text{Al}_2\text{O}_3/\text{Li}_2\text{CO}_3\text{-K}_2\text{CO}_3$ (1.0 wt%) nanomaterial after the evaporation was completed. The image shows coarse amorphous powder (Type-A) and fine amorphous powder (Type-B)	133

	Page
Figure 56 Variation of the specific heat capacity with temperature (355 °C ~ 495 °C) for $\text{Al}_2\text{O}_3/\text{Li}_2\text{CO}_3\text{-K}_2\text{CO}_3$ nanocomposites. The average specific heat capacity of both nanocomposites were enhanced by 8~37 % over the pure molten salt eutectic.....	135
Figure 57 Variation of specific heat capacity with temperature (525 °C ~ 555 °C) for $\text{Al}_2\text{O}_3/\text{Li}_2\text{CO}_3\text{-K}_2\text{CO}_3$ nanofluids	138
Figure 58 SEM images of Type-A $\text{Al}_2\text{O}_3/\text{Li}_2\text{CO}_3\text{-K}_2\text{CO}_3$ nanomaterial (coarse powder samples).....	142
Figure 59 SEM images of Type-B $\text{Al}_2\text{O}_3/\text{Li}_2\text{CO}_3\text{-K}_2\text{CO}_3$ nanomaterial (coarse powder samples) showing nanoparticles with no (or minimal) agglomeration. Special threadlike nano-structures were observed	142
Figure 60 TEM images of Type-B $\text{Al}_2\text{O}_3/\text{Li}_2\text{CO}_3\text{-K}_2\text{CO}_3$ powders showing the formation of thread shaped nanostructures. The alumina nanoparticles were observed to be located at the intersection of the thread shaped nanostructures.....	143
Figure 61 High resolution TEM images of the thread shaped nanostructures. It was observed that a group of alumina nanoparticles are located at the intersection of the thread shaped nano-structures. The group of nanoparticles therefore seems to induce the nucleation and germination of the threadlike nanostructures that mutually interconnect with each other. It was also observed that nanoparticles are not agglomerated and the nominal size of the nanoparticle is 1~20 nm.....	143
Figure 62 (a) SEM image of $\text{SiO}_2/\text{Li}_2\text{CO}_3\text{-K}_2\text{CO}_3$ nanomaterial. (b) Histogram plot of the pixel intensities obtained from the SEM image (a). (c) Binary image of the SEM image after setting a threshold intensity of 128. (d) Histogram plot of the binary image after image processing in (c). Based on the image histogram plot, 40.5 % of the image area is covered by the brighter pixels of the woven structures	148
Figure 63 (a) SEM image of $\text{MgO}/\text{Li}_2\text{CO}_3\text{-K}_2\text{CO}_3$ nanomaterial. (b) Histogram plot of the pixel intensities obtained from the SEM image (a). (c) Binary image of the SEM image after setting a threshold intensity of 128. (d) Histogram plot of the binary image after image processing in (c). Based on the image histogram plot, 28.9 % of the image area is covered by the brighter pixels of the woven structures	149

Figure 64 (a) SEM image of $\text{Al}_2\text{O}_3/\text{Li}_2\text{CO}_3\text{-K}_2\text{CO}_3$ nanomaterial. (b) Histogram plot of the pixel intensities obtained from the SEM image (a). (c) Binary image of the SEM image after setting a threshold intensity of 128. (d) Histogram plot of the binary image after image processing in (c). Based on the image histogram plot, 35.6 % of the image area is covered by the brighter pixels of the woven structures	150
Figure 65 Phase diagram of molten salt ($\text{Li}_2\text{CO}_3\text{-K}_2\text{CO}_3$) [61]	166
Figure 66 Nanoparticle agglomerations in the nanomaterial, whose molten salt composition is 46:54 (by molar ratio)	171
Figure 67 Nanoparticle agglomerations in the nanomaterial, whose molten salt composition is 54:46 (by molar ratio)	171
Figure 68 Nanoparticle agglomerations in the nanomaterial, whose molten salt composition is 78:22 (by molar ratio)	172
Figure 69 Specific heat capacity of molten salt at solid phase (Figure 25)	174
Figure 70 Molar specific heat capacity of molten salt at solid phase (Figure 26)	175

LIST OF TABLES

	Page
Table 1 Effective thermal conductivity of nanofluids [22]	7
Table 2 Effective specific heat capacity of nanofluids [22]	8
Table 3 Parameters for potential fields for the MD simulations performed in this study. CNT Parameters were collected from Material Studio (ver 5.0, Accelrys, Inc.). Eutectic parameters were obtained from Costa [44] and Braybrook et al. [45], respectively. (C=0 and D=0 for Born-Mayer-Huggins potential)	25
Table 4 Parameters for potential fields for the MD simulations performed in this study. SiO ₂ Parameters were collected from Tsuneyuki et al. [49] and eutectic parameters were obtained from Costa [44] and Braybrook et al. [45], respectively. Other parameters were collected from Material Studio (Accelrys, Inc., ver. 4.4)	28
Table 5 Interfacial thermal resistance and the corresponding value for optimum size of CNT obtained from each simulation	37
Table 6 Interfacial thermal resistance and the corresponding value for the optimum size of the silica nanoparticle for each simulation	42
Table 7 Specific heat capacity measurements (J /g-K) of pure eutectic salt of BaCl ₂ -NaCl-CaCl ₂ -LiCl and the corresponding SiO ₂ nanocomposite samples. Average specific heat capacity measurements (J /g-K) of the pure eutectic and the nanocomposite at solid phase (155 ~ 315 °C) are listed here. The average specific heat capacity of the nanocomposite was enhanced by 6 ~ 7 % compared with that of the pure eutectic [37]. (ε: standard deviation for all the thermo-cycle data for a sample)	53
Table 8 Specific heat capacity measurements (J /g-K) of pure eutectic salt of BaCl ₂ -NaCl-CaCl ₂ -LiCl and the corresponding SiO ₂ nanofluid samples. Average specific heat capacity measurements (J /g-K) of the pure eutectic and the nanofluid (495 ~ 555 °C) are listed here. The average specific heat capacity of the nanofluid samples were enhanced by 13 % ~ 16 % compared with that of the pure eutectic [37]. (ε: standard deviation for all the thermo-cycle data for a sample)	55

Table 9	Specific heat capacity measurements (J /g-K) of pure eutectic salt of $\text{Li}_2\text{CO}_3\text{-K}_2\text{CO}_3$ and the corresponding SiO_2 nanocomposite samples. Average specific heat capacity measurements (J /g-K) of the pure eutectic and the nanocomposite in the temperature range of 495 ~ 555 °C are listed here. The average specific heat capacity of the nanocomposite samples were enhanced by 11 % ~ 14 % compared with that of the pure eutectic. (ϵ : standard deviation for all the thermo-cycle data for a sample) [36].....	61
Table 10	Specific heat capacity measurements (J /g-K) of pure eutectic salt samples of $\text{Li}_2\text{CO}_3\text{-K}_2\text{CO}_3$ and the corresponding SiO_2 nanofluid samples. Average specific heat capacity measurements (J /g-K) of the pure eutectic and the nanofluid for a temperature range of 495 ~ 555 °C are listed here. The average specific heat capacity of the nanofluid samples were enhanced by 13 % ~ 16 % compared with that of the pure eutectic [36]. (ϵ : standard deviation for all the thermo-cycle data for a sample).....	63
Table 11	Discrepancy between the experimental data and the prediction by the simple mixing model (Equation 14). (*: measurement uncertainty).....	69
Table 12	Average specific heat capacity of molten salts in the solid phase and for the corresponding nanocomposites. (ϵ : measurement uncertainty; * from literature [36]; ** at the transition region, where the specific heat capacity of molten salt is unstable and changes dramatically for each measurement)	83
Table 13	Average specific heat capacity of molten salts in the liquid phase and the corresponding nanofluids. (ϵ : measurement uncertainty; * from literature [36]); ** at the transition ratio, the specific heat capacity of molten salt is unstable and changes dramatically with each measurement).....	84
Table 14	Solid Phase Data. Discrepancy between the the experimental data and the predictions from the simple mixing model (Equation 14). (*: measurement uncertainty).....	96
Table 15	Liquid Phase Data. Discrepancy between the experimental data and the prediction by the simple mixing model (Equation 14). (*: measurement uncertainty).....	96

	Page
Table 16 Density, specific heat capacity, thermal diffusivity, and thermal conductivity of the pure eutectic salt and the SiO ₂ nanocomposite (at mass concentration of 1%)	101
Table 17 Comparison of experimentally measured data with theoretical estimates for the thermal conductivity of SiO ₂ nanocomposite at 1% concentration by weight	104
Table 18 Specific heat capacity measurements (J /g-K) of Type-A SiO ₂ /Li ₂ CO ₃ -K ₂ CO ₃ nanocomposites, which are obtained from the coarse powders of eutectics containing agglomerated nanoparticles. No significant change in the specific heat capacity values were observed – within the bounds of the measurement uncertainty (ε: standard deviation for all the thermo-cycle data for a sample).....	111
Table 19 Specific heat capacity measurements (J /g-K) of Type-B SiO ₂ /Li ₂ CO ₃ -K ₂ CO ₃ nanocomposites, that are obtained from fine amorphous powders of eutectics that contained uniformly dispersed nanoparticles with no (or minimal) agglomeration. (ε: standard deviations for all the thermo-cycle data for a given sample)	112
Table 20 Specific heat capacity measurements (J /g-K) of Type-A SiO ₂ /Li ₂ CO ₃ -K ₂ CO ₃ nanofluids, which are obtained from the coarse powders of eutectics containing agglomerated nanoparticles. No significant change in the specific heat capacity values were observed – within the bounds of the measurement uncertainty (ε: standard deviation for all the thermo-cycle data for a sample).....	114
Table 21 Specific heat capacity measurements (J /g-K) of Type-B SiO ₂ /Li ₂ CO ₃ -K ₂ CO ₃ nanofluids, that are obtained from fine amorphous powders of eutectics that contain uniformly dispersed nanoparticles with no (or minimal) agglomeration. (ε: standard deviations for all the thermo-cycle data for a given sample)	115
Table 22 Specific heat capacity measurements (J /g-K) of Type-A MgO/Li ₂ CO ₃ -K ₂ CO ₃ nanocomposites, which are obtained from the coarse powders of salts containing agglomerated nanoparticles. The average specific heat capacity of Type-A nanocomposites was enhanced by 2~16 % over that of the pure molten salt eutectic. (ε: standard deviation for all the thermo-cycle data for a sample).....	123

	Page
Table 23 Specific heat capacity measurements (J /g-K) of Type-B nanocomposites of Li_2CO_3 - K_2CO_3 , that contain uniformly dispersed MgO nanoparticles with no (or minimal) agglomeration. (ϵ : standard deviations for all the thermo-cycle data for a given sample). Measurement uncertainty is 1.9 %.....	124
Table 24 Specific heat capacity measurements (J /g-K) of Type-A MgO/ Li_2CO_3 - K_2CO_3 nanofluids, which are obtained from the coarse powders of eutectics containing agglomerated nanoparticles. (ϵ : standard deviation for all the thermo-cycle data for a sample).....	126
Table 25 Specific heat capacity measurements (J /g-K) of Type-B MgO/ Li_2CO_3 - K_2CO_3 nanofluids, that were obtained from the fine amorphous powders of eutectics that contain uniformly dispersed nanoparticles with no (or minimal) agglomeration. (ϵ : standard deviations for all the thermo-cycle data for a given sample).....	127
Table 26 Specific heat capacity measurements (J /g-K) of Type-A Al_2O_3 / Li_2CO_3 - K_2CO_3 nanocomposites, which are obtained from the coarse powders of eutectics containing agglomerated nanoparticles. (ϵ : standard deviation for all the thermo-cycle data for a sample).....	136
Table 27 Specific heat capacity measurements (J /g-K) of Type-B Al_2O_3 / Li_2CO_3 - K_2CO_3 nanocomposites, that are obtained from fine amorphous powders of eutectics that contain uniformly dispersed nanoparticles with no (or minimal) agglomeration. (ϵ : standard deviations for all the thermo-cycle data for a given sample).....	137
Table 28 Specific heat capacity measurements (J /g-K) of Type-A Al_2O_3 / Li_2CO_3 - K_2CO_3 nanofluids, which were obtained from the coarse powders of eutectics containing agglomerated nanoparticles. (ϵ : standard deviation for all the thermo-cycle data for a sample).....	139
Table 29 Specific heat capacity measurements (J /g-K) of Type-B Al_2O_3 / Li_2CO_3 - K_2CO_3 nanofluids, that are obtained from fine amorphous powders of eutectics that contain uniformly dispersed nanoparticles with no (or minimal) agglomeration. (ϵ : standard deviations for all the thermo-cycle data for a given sample).....	140
Table 30 ICP test results for Type-A nanomaterials and Type-B nanomaterials. SiO_2 nanoparticles at 1% mass concentration in molten salt of Li_2CO_3 : K_2CO_3 (by molar ratio)	145

	Page
Table 31 Estimated specific heat capacity of the micron-scale sub-structures (percolation network) based on image analysis and using Equation 15 ...	147
Table 32 Specific heat capacity of molten salt and its nanomaterial, whose molten salt composition is 46:54 (by molar ratio)	168
Table 33 Specific heat capacity of molten salt and its nanomaterial, whose molten salt composition is 54:46 (by molar ratio)	169
Table 34 Specific heat capacity of molten salt and its nanomaterial, whose molten salt composition is 78:22 (by molar ratio)	170
Table 35 P-values of each molten salt and its nanomaterial	173

1. INTRODUCTION

Since the industrial revolution from the 18th century, remarkable advances have been achieved in science, engineering, and technology. Utilization of fossil-based energy resources has accelerated this growth. However, the fossil energy resources (such as petroleum, coal, and natural gas) are limited and have associated social costs due to emission of combustion byproducts. Consequently, the world is faced with the depletion of the fossil energy resources and associated issues. For example, the combustion of fossil fuels has been perceived to cause several environmental problems such as global warming (carbon dioxide) and air pollution (nitrogen oxides or sulfur dioxide) [1]. Therefore, research on alternative energy resources such as renewable energy resources has garnered significant attention recently [2].

Solar energy, one of the renewable energy resources, is practically unlimited as well as environmentally clean. Solar energy can be harvested by photovoltaics (PV; direct method) or by concentrating solar power (CSP; indirect method). PV uses semiconductor materials to directly convert the solar energy (radiant light) to electricity. CSP uses solar receivers (mirrors or lenses) to concentrate the solar energy (thermal energy) and the concentrated thermal energy is typically converted to electricity using thermodynamic cycles (Rankine cycle or Stirling cycle). Thermal energy storage (TES) enables the continuous operation of the power plant (e.g., during cloud cover or during

This dissertation follows the style of Journal of Heat Transfer.

night time). TES is typically used to delay the peak in power production (by ~3 hours) to meet the peak in demand for utilities which typically occurs between 4-7 p.m. while the insolation typically peaks between 1-3 p.m. Considering the levelized cost of electricity (LCoE), CSP is competitive with the contemporary peak price of electricity considering the diurnal price variation for electricity supplied by the utilities.

1.1 Concentrating Solar Power System: Solar Thermal Energy Storage

Concentrating solar power (CSP) technology is considered to be an economically attractive option for harnessing renewable energy resources. A power plant using CSP technology typically consists of: (a) an array of solar receivers (lenses, mirrors/heliostats) for collecting and focusing the incident solar energy; (b) a solar tower or collection unit for collecting the focused solar energy; (c) a heat transfer fluid (HTF) system for transferring the collected solar energy; (d) a thermal energy storage (TES) device for storing the excess capacity; and (e) power conversion module for converting the collected thermal energy to electricity. The power conversion module is typically a turbine (e.g., operating on Rankine cycle) or an engine (e.g., operating on Stirling cycle).

The thermodynamic efficiency of the Rankine cycle mainly relies on the difference in temperature between the entry of the turbine (hot) and the condenser (cold). Since it is very expensive to decrease the condenser temperature, increasing the entry temperature is the key for enhancing the overall system efficiency of the CSP. This temperature is limited by the material properties of the TES. Current TES media such as

synthetic oil, paraffin wax, or fatty acid are optimized for the temperature up to 400 °C; therefore, raising the temperature up to 560 °C, which is the approximately initial creep temperature of stainless steel, can improve the theoretical Carnot efficiency from 55 % to 64 %. However, very few materials are compatible at the high temperature (over 500 °C).

1.2 Molten Salts

Molten salts are alkali-nitrate, alkali-carbonate, alkali-chloride (or halogen derivatives), or eutectic mixture of those. The molten salts have a wide range of melting points from 200 °C to 600 °C and they are stable up to 600 °C [2,3]. Using the molten salts as the TES materials confer several benefits [4]. The benefits are as follows: (1) The high temperature stability can increase the operating temperature of the CSP and consequently enhance the thermodynamic cycle efficiency. (2) The molten salts are cheaper than conventional TES materials and therefore the system costs of the CSP can be significantly reduced. (3) The molten salts are environmentally safe. This can obviate the potential costs for environmental remediation. However, the low thermal properties of the molten salts are an impediment for application in TES [2, 5].

1.3 Nanomaterials: Nanofluids and Nanocomposites

Solid particles with better thermo-physical properties (than the liquid solvent) have often been explored by mixing them with liquids to enhance the effective properties of the mixture. However, the stability of the mixture has often been a source of controversy, since these solid particles have a propensity to agglomerate or precipitate in the liquid.

“Nanofluids” are solvents doped with minute concentration of nanometer-sized particles [6]. Since these nanometer-sized particles (“nanoparticles”) have very large surface area to volume ratio, the surface charge of the nanoparticle is very significant compared to micrometer or millimeter sized particles. The increased surface charge enables the nanoparticle to be well dispersed in the liquid and enhances the stability of the resulting mixture. Hence, stable liquid/particle suspensions can be realized by following suitable synthesis technique. Also, dispersed nanoparticles in a matrix (solid phase) are termed as “nanocomposites.”

1.4 Nanomaterials: Thermal Conductivity and Specific Heat Capacity

High thermo-physical properties of the nanoparticles contribute to the enhancement of the effective thermal properties of the nanomaterials. Several studies have been published for enhanced thermal conductivity of nanocomposites. Song and Youn [7] reported 100 % enhancement in the thermal conductivity of carbon nanotube

(CNT) / epoxy nanocomposite for 1.5 % concentration of CNT by weight (in comparison to that of the pure epoxy). Haggenueller et al. [8] reported 700 % enhancement in the thermal conductivity of polyethylene when mixed with CNT (nanocomposite) at a concentration of 20 % by volume. Wang et al. [9] reported 30 % enhancement in the thermal conductivity of CNT / polymer nanocomposite at only 1 % concentration of CNT by weight.

Similar to the investigations reported for nanocomposites, numerous reports have been published for anomalous enhancement of the thermal properties of various nanofluids [10-28]. (Table 1) Effective thermal conductivity of Al_2O_3 / water nanofluid was enhanced by 23 % for only 4.0 % concentration by volume [10]. SiC/water nanofluid showed 17 % enhancement in the effective thermal conductivity at only 4.18 % volume concentration of SiC nanoparticle [11]. CuO/ water nanofluid showed 36 % enhancement in the effective thermal properties for 4.0 % concentration by volume [12]. Cu/ water nanofluid was reported to enhance the effective thermal conductivity by 75% at 7.5 % concentration by volume [13]. Ag/ water nanofluid showed 8 % enhancement in the effective thermal conductivity for only 0.00026 % concentration by volume [14]. Apart from aqueous nanofluids, ethylene glycol (EG)-based nanofluids also showed enhancement in the effective thermal conductivity compared to that of pure EG. CuO/ EG nanofluid showed 54 % enhancement in the effective thermal conductivity for 14.8 % concentration by volume [15]. Fe/EG nanofluid showed 18 % enhancement in the effective thermal conductivity at 0.55 % concentration by volume [16]. Cu/ EG nanofluid showed 10 % enhancement in the effective thermal conductivity at only

0.28 % concentration by volume [17]. A number of investigations have been reported on the anomalously enhanced effective thermal conductivity of these nanofluids. The reports included investigation of several mechanisms such as: Brownian motion of the nanoparticles in the liquids, nano-convection caused by the Brownian movement of the nanoparticles, agglomeration of the nanoparticles, interfacial thermal resistance, and nature of heat transfer within the nanoparticles [18-21]. Recent studies suggest that interconnected network formed by the clustering of the nanoparticles is responsible for the enhanced effective thermal conductivity of the nanofluids [29, 30].

While a wide range of nanomaterials (especially nanofluids) was reported for the enhancement in their effective thermal conductivity, only a few studies have been reported on the specific heat capacity measurements (Table 2). Hence, in contrast, the specific heat capacity measurement of the nanomaterials is a relatively less controversial topic and also has not been explored in as much detail in the literature. Aqueous and EG-based nanofluids showed a net decrease in the specific heat capacity. Al_2O_3 /water nanofluid showed 40 % decrease in specific heat capacity at 21.7 % concentration by volume [31]. SiO_2 /water nanofluid showed 12 % decrease in specific heat capacity at 10 % concentration by volume [32]. ZnO / water-EG nanofluid showed 20 % decrease in the specific heat capacity at 7 % concentration by volume [33].

On the contrary, graphite/polyalphaolefin nanofluid showed 50 % enhancement in the specific heat capacity at only 0.6 % concentration by weight [34]. Shin and Banerjee [35-37] and Shin et al. [38] reported enhanced specific heat capacities of four different nanofluids. These studies were performed primarily for TES applications.

Table 1. Effective thermal conductivity of nanofluids [22]

1st author	Nanoparticle / solvent	Concentration (volume %)	Particle Size	Enhancement (%)
Lee [10]	Al ₂ O ₃ / water	4.0	23.6 nm	23%
Wang [15]	CuO/ ethylene glycol	14.8	23 nm	54%
Xie [11]	SiC/ water	4.18	26 nm	17%
Das [12]	CuO/ water	4.0	28.6 nm	36%
Wen [23]	Al ₂ O ₃ / water	1.59	42 nm	10%
Chon [24]	Al ₂ O ₃ / water	4.0	47 nm	29%
Hong [16]	Fe/ ethylene glycol	0.55	10 nm	18%
Xuan [13]	Cu/ water	7.5	100 nm	75%
Eastman [17]	Cu/ ethylene glycol	0.28	<10 nm	10%
Patel [14]	Ag/ water	0.00026	10~20 nm	8%
Choi [25]	MWCNT/ polyalphaolefin	1.0	25 nm(D) ×50 μm(L)	157%
Xie [26]	MWCNT/ ethylene glycol	1.0	15 nm(D) ×30 μm(L)	13%
Assael [27]	MWCNT/water	0.6	100 nm(D) ×50 μm(L)	38%
Assael [28]	MWCNT/water	0.6	130 nm(D) ×10 μm(L)	28%

Table 2. Effective specific heat capacity of nanofluids [22]

1st author (year)	Nanoparticle / Base fluid	Concentration (%)	Particle Size	Enhancement (%)
Nelson [34]	graphite/polyalphaolefin	0.6 wt.%	20 μm (D) $\times 100$ nm(L)	50%
Shin [35]	SiO ₂ /Li ₂ CO ₃ -K ₂ CO ₃	1.5 wt.%	10 nm	100%
Shin [38]	CNT/Li ₂ CO ₃ -K ₂ CO ₃	0.5 wt.%	30 nm(D) $\times 1.5$ μm (L)	18%
Shin [36]	SiO ₂ /Li ₂ CO ₃ -K ₂ CO ₃	1.0 wt.%	30 nm	26%
Shin [37]	SiO ₂ /BaCl ₂ -NaCl- CaCl ₂ -LiCl	1.0 wt.%	30 nm	19%
Zhou [31]	Al ₂ O ₃ /water	21.7 vol.%	45 nm	-40%
Namburu [32]	SiO ₂ /water	10 vol.%	20 nm	-12%
Vajjha [33]	ZnO/water-ethylene glycol	7 vol.%	77 nm	-20%

1.5 Nanomaterials: Interfacial Thermal Resistance

Interfacial thermal resistance (i.e. Kapitza resistance) is the resistance to thermal transport (i.e., resistance to heat transfer due to different spectral distribution of molecular vibrations or phonon transport in the different media) that typically occurs at the interface between a solid surface and liquid molecules that are located in the vicinity of the solid surface [39]. This should not be confused with thermal contact resistance but is rather the thermal transport resistance that occurs due to different rates of phonon propagation in different materials that are in mutual contact. Thus the Kapitza resistance exists even if two media are in perfect thermal contact (i.e., even if the thermal contact resistance is non-existent). Hence, Kapitza resistance exists due to the difference in vibrational properties between different materials. This resistance is insignificant and is usually neglected for macroscopic heat transfer. However, it plays a significant role for nano-scale heat transfer. Since nanoparticles have exceptionally large surface area, the interfacial area between the surface of the nanoparticle and the surrounding liquid molecules is also very large. The extraordinarily enlarged magnitude of the specific interfacial area significantly increases the effect of the interfacial thermal resistance on the heat transfer within the nanofluid. The interfacial thermal resistance acts as a thermal barrier. If the nanoparticle size decreases, the surface area of the nanoparticle increases and the effect of the interfacial thermal resistance increases, which leads to a decrease of the effective thermal conductivity of the nanofluid. Therefore, a lower limit of the nanoparticle size exists when the effect of the interfacial thermal resistance become

significant. Also, an upper size limit exists for nanoparticles at which the thermophoretic/ chemical (or Brownian) diffusion of the nanoparticles is hampered – leading to degradation in the effective thermal conductivity of the mixture. Hence, an optimum size of the nanoparticles exists for maximizing the effective thermal conductivity of nanofluids.

1.6 Molecular Dynamics Simulation

Molecular dynamics (MD) simulation is a computational method to simulate the temporal and spatial evolution of atoms in a thermodynamic system. It is used for computing the physical and chemical properties of various materials. In a typical MD simulation, the Newton's equation of motion are solved for every atom in a system at every time step by assuming a particular model for the force fields arising from individual atoms due to several types of fundamental material interactions (e.g., van der Waals forces, charge/ electrostatic forces, hydrogen bonding, chemical bonding, etc.). Therefore, positions and velocities of each atom can be obtained at each time step by calculating the mutual interactions based on the assumed force field. These position and velocity information corresponding to each atom in the system are then used to calculate material properties of the system using the space / time correlations available in statistical mechanics [40]. MD simulation is very useful to compute material properties, which are often difficult to measure reliably in experiments. One such example is the interfacial thermal resistance. Since it is difficult to conduct for measuring the interfacial

thermal resistance for individual nanoparticles in a mixture, a number of studies have been published to computationally estimate this parameter using MD simulations. Maruyama et al. [41] computed the interfacial thermal resistance (Kapitza resistance) between single walled carbon nanotube (CNT) and water and reported the resistance to be $1.22 \times 10^{-7} \text{ m}^2 \text{ K/W}$. Shenogin et al. [42] computed the interfacial thermal resistance between carbon nanotubes and octane molecules and reported the Kapitza resistance to be $4.0 \times 10^{-8} \text{ m}^2 \text{ K/W}$. Huxtable et al. [43] simulated carbon nanotubes coated with surfactants (sodium dodecyl sulfate) in water and reported the interfacial thermal resistance between CNT and SDS to be $8.3 \times 10^{-8} \text{ m}^2 \text{ K/W}$.

1.7 Objective of the Study

The aim of the study is to explore the effect of physically mixing nanoparticles with molten salt eutectics on their thermo-physical properties.

1.8 Motivation of the Study

Similar to the previous reports in the literature on nanomaterials, the low thermal properties of the molten salts can potentially be improved by doping with nanoparticles. Addition of nanoparticles at minute concentration can significantly enhance the thermal conductivity as well as the specific heat capacity of the nanomaterials.

In this study, several nanomaterials based on molten salt eutectics were synthesized by using a simple liquid solution synthesis method. The thermal properties of the molten salt nanomaterials were measured experimentally. Computational studies involving molecular dynamics simulations were performed for estimating the interfacial thermal resistance between the nanoparticle and the molten salt eutectics. The effect of the size of the nanoparticle on the effective thermal conductivity was investigated using the simulations for predicting the interfacial thermal resistance values. In the experimental studies, a number of molten salt nanomaterials were synthesized. Specific heat capacity and thermal conductivity measurements were performed to investigate the effect of mixing the nanoparticles with the molten salt. Electron microscopy analyses such as scanning electron microscopy and transmission electron microscopy were performed to observe the morphology of nanoparticles and molten salts before and after the experiments. Hence, the transport mechanisms responsible for the enhancement in the thermo-physical properties of these nanomaterials were explored.

1.9 Significance of the Study

This study will contribute not only to designing advanced nanomaterials for solar thermal energy storage applications but also to the studies on high temperature heat transfer phenomena especially at the nano-scale. The results from this study provide evidences which contradict existing misconceptions in the literature on the effective

thermo-physical properties of nanomaterials. The details of the contribution from this study are listed below:

- Novel synthesis method for molten salt nanomaterials
- The effect of doping nanoparticles on specific heat capacity of nanomaterials
- The effect of doping nanoparticles on thermal conductivity of nanomaterials
- The effect of phase change on the specific heat capacity of nanomaterials
- The effect of morphology of nanoparticle/molten salt on the resulting properties.
- The effect of interfacial thermal resistance on the thermal conductivity of nanofluids.

1.10 Summary

Computational and experimental studies were performed to explore molten salt nanofluids for solar thermal energy storage applications. The computational study enabled the preliminary design of the molten salt nanofluids, especially for estimating the optimum size of the nanoparticles. The experimental studies showed anomalous enhancement in the specific heat capacity as well as the thermal conductivity.

Section 2 and 3 provide a background of molecular dynamics simulation, interfacial thermal resistance of various molten salt/nanoparticle mixtures, and the effect of nanoparticle size on the properties of the molten salt nanomaterials.

Section 4 and 5 provide information on the synthesis protocols, measurement protocols for the specific heat capacity measurements of the samples, the thermal

conductivity measurement of the nanomaterials, and the electron microscopy techniques that were utilized to observe the morphologies of the various nanomaterials.

Section 6 summarizes the results and conclusions derived from this study as well as the suggested future directions for subsequent investigations.

2. COMPUTATIONAL STUDY

Molecular dynamics simulations were performed to estimate the interfacial thermal resistance between a nanotube (or a nanoparticle) and the surrounding molecules of the molten salt. A single-walled carbon nanotube was dispersed in a eutectic of Li_2CO_3 and K_2CO_3 (62:38 by molar ratio) and the interfacial thermal resistance was evaluated to determine the optimal size of the nanotube for enhancing the effective thermal conductivity of the nanofluid, based on existing models in the literature. Also, Molecular Dynamics (MD) simulations were performed for a silica nanoparticle dispersed in the same eutectic and the interfacial thermal resistance was evaluated in the same manner. This exercise was performed to determine the optimum size of nanotubes (and nanoparticles) for the experiments that were performed subsequently. Hence the MD simulations were performed to enable the design of experiments in this study.

2.1 Molecular Dynamics Simulation

Molecular Dynamics (MD) simulation is typically used to compute the temporal and spatial motion of atoms and molecules in a system. This computational technique is very useful for calculating the material properties of various nanomaterials. MD simulation is especially valuable for computing certain properties, which are experimentally inaccessible (e.g. atomic or molecular scale material transport processes). In MD simulation, position and velocities of atoms or molecules are numerically

calculated by solving the Newton's equations of motion. The position and the velocity information of the individual atoms are then used to obtain different properties of the system using equations of statistical mechanics. The potential energy of a system is usually computed using force fields. The force fields are simple equations and parameter sets, which are used to calculate the potential energy of a system. The force field equations and parameters are usually obtained from experiments or quantum mechanics calculation. A number of force fields are available in the literature. In this study, standard "12/6" Lennard-Jones potential along with Coulomb force interactions (equation 1) and Born-Mayer-Huggins potential (equation 2) were employed for non-bonded interactions as follows:

$$E = \frac{q_i q_j}{r} + 4\epsilon \left[\left(\frac{\sigma}{r} \right)^{12} - \left(\frac{\sigma}{r} \right)^6 \right] \quad (1)$$

$$E = A \exp\left(\frac{\sigma - r}{\rho}\right) - \frac{C}{r^6} + \frac{D}{r^8} + \frac{q_i q_j}{r} \quad (2)$$

For bonded interactions, bond-stretching, bond-bending, and torsional interactions are used (equation 3):

$$E = k_s (r - r_0)^2 + k_b (\theta - \theta_0)^2 + k_t \{1 + d \cos(n\varphi)\} \quad (3)$$

All parameters for non-bonded and bonded interactions were found from various reports in the literature and are listed in the table on page 25 (Material Studio ver. 5.0, Accelrys, Inc.; cf. references [44, 45]).

2.2 Interfacial Thermal Resistance

Interfacial thermal resistance (“Kapitza resistance”) is the resistance to heat transfer (or phonon propagation) at the interface between two different materials [39]. This resistance arises from different rates of phonon propagation in two materials and exists even at interfaces that are in perfect contact (i.e., for zero thermal contact resistance). The interfacial thermal resistance is often neglected for macroscopic heat transfer calculations, yet it is of significant magnitude for nano-scale heat transfer and cannot be neglected for nano-scale heat transfer calculations. Since nanoparticles have very large surface area per unit volume, the total interfacial area for sum total all of the nanoparticles in a nanofluid is also of substantially large magnitude. The exceptionally large interfacial area leads to very high values of the interfacial thermal resistance in the nanofluid (on an unit mass basis). If the size of a nanoparticle decreases, the surface area of the nanoparticle increases (on a unit volume basis), which leads to significant enhancement of the interfacial thermal resistance. If the size of the nanoparticle decreases below a critical value, the large value of the interfacial thermal resistance can lead to degradation of the effective thermal conductivity of the nanofluid. Therefore, it is

necessary to estimate the critical size of the nanoparticle for synthesizing nanofluids and for maximizing (or optimizing) their thermal properties for particular applications.

The interfacial thermal resistance is difficult to measure in experiments and therefore MD simulations are widely used to compute the interfacial thermal resistance. MD simulations for estimating the interfacial thermal resistance for various nanocomposites/ nanofluid mixtures have been reported widely in the literature. Using MD simulations Maruyama et al. [41] reported the interfacial thermal resistance between single walled carbon nanotube and water molecules to be $1.22 \times 10^{-7} \text{ m}^2\text{K/W}$. Shenogin et al. [42] calculated the interfacial thermal resistance between carbon nanotubes and octane molecules using MD simulations and reported the value to be $4.0 \times 10^{-8} \text{ m}^2\text{K/W}$. Huxtable et al. [43] performed MD simulations for carbon nanotubes coated with a surfactant (sodium dodecyl sulfate) that was then dissolved in water and the interfacial thermal resistance between CNT and SDS was reported to be $8.3 \times 10^{-8} \text{ m}^2\text{K/W}$.

A convenient approach for computing the interfacial thermal resistance is the lumped capacitance method. Assuming that a nanoparticle in a fluid (“nanofluid”) is highly conductive (Biot number $\ll 1$), the entire nanoparticle will be at the same temperature as the surface temperature of the nanoparticle. Since the interfacial thermal resistance dominates the heat transfer in nanofluids, the total heat transfer between the nanoparticle and the surrounding fluid can be simplified as follows:

$$\dot{Q} = \rho_{np} V_{np} C_{p,np} \frac{dT}{dt} \approx -\frac{A_s}{R_b} (T_s - T_f) \quad (4)$$

where, t is the time, ρ_{np} is the density of the nanoparticle, V_{np} is the volume of the nanoparticle, $C_{p,np}$ is the specific heat capacity of the nanoparticle, A_s is the interfacial area of the nanoparticle, R_b is the interfacial thermal resistance, T_s is the temperature of the nanoparticle, and T_f is the temperature of the fluid. Integration of the equation (4) yields the following expression:

$$\frac{T_s - T_f}{T_{s,i} - T_f} = e^{-\frac{A_s}{\rho_{np} V_{np} C_{p,np} R_b} t} = e^{-\frac{t}{\tau}} \quad (5)$$

The time constant, τ is then a function of R_b , and is expressed as:

$$\tau = \frac{\rho_{np} V_{np} C_{p,np} R_b}{A_s} \quad (6)$$

2.3 Effect of Size of the Nanoparticle

For a carbon nanotube (CNT) suspension in a fluid - the effective thermal conductivity can be calculated using a model involving a long circular cylinder oriented perpendicular to the direction of heat transfer. This model was proposed by Hasselman and Johnson [46] and is expressed as:

$$\frac{k_{eff}}{k_b} = \frac{\left(\frac{k_{np}}{k_b} - 1 - \frac{2k_{np}R_b}{d}\right) \cdot V_{np} + \left(\frac{k_{np}}{k_b} + 1 + \frac{2k_{np}R_b}{d}\right)}{-\left(\frac{k_{np}}{k_b} - 1 - \frac{2k_{np}R_b}{d}\right) \cdot V_{np} + \left(\frac{k_{np}}{k_b} + 1 + \frac{2k_{np}R_b}{d}\right)} \quad (7)$$

where k_{eff} is the effective thermal conductivity of the nanofluid, k_b is the thermal conductivity of the base fluid, k_{np} is the thermal conductivity of the nanotube, R_b is the interfacial thermal resistance, V_{np} is the volume concentration of the carbon nanotube, and d is the diameter of the carbon nanotube. By assuming $k_{np} \gg k_b$, the equation (7) is simplified as:

$$\frac{k_{eff}}{k_b} = \frac{\left(1 - \frac{2k_b R_b}{d}\right) \cdot V_{np} + \left(1 + \frac{2k_b R_b}{d}\right)}{-\left(1 - \frac{2k_b R_b}{d}\right) \cdot V_{np} + \left(1 + \frac{2k_b R_b}{d}\right)} \quad (8)$$

In the equation (8), the diameter of the nanotube, d , should be higher than $2R_b k_b$ in order to obviate the effect of the interfacial thermal resistance,

$$d_c > 2R_b k_b \quad (9)$$

For a spherical nanoparticle suspension in a fluid, the effective thermal conductivity can be expressed as follows [47]:

$$\frac{k_{eff}}{k_b} = \frac{\left(k_p \left(1 + \frac{4R_b k_b}{d}\right) + 2k_b\right) + 2V_p \left(k_p \left(1 - \frac{2R_b k_b}{d}\right) - k_b\right)}{\left(k_p \left(1 + \frac{4R_b k_b}{d}\right) + 2k_b\right) - V_p \left(k_p \left(1 - \frac{2R_b k_b}{d}\right) - k_b\right)} \quad (10)$$

For enhancing the effective thermal conductivity by mixing with spherical nanoparticles, the following condition should be satisfied:

$$\left(1 - \frac{2R_b k_b}{d_c}\right) > \frac{k_b}{k_p} \quad (11)$$

Hence Equation (11) can be rearranged as:

$$d_c > \frac{2R_b k_b}{1 - \frac{k_b}{k_p}} \quad (12)$$

Equation (9) shows that the optimum diameter (d) of the nanotube is a function of the interfacial thermal resistance (R_b) and the thermal conductivity of the fluid (k_b). Equation (12) shows that the optimum diameter (d) of the nanoparticle is a function of the interfacial thermal resistance (R_b), the thermal conductivity of the fluid (k_b), and the thermal conductivity of the nanoparticle (k_p). The thermal conductivity values of various materials are conveniently available in the literature and in text books. However, the values of interfacial thermal resistance are not as widely reported (or investigated) in the

literature. Hence, it is necessary to compute the interfacial thermal resistance between a nanoparticle and the solvent (fluid) in order to estimate the optimum size of the nanoparticle. In this study, MD simulations were employed to compute the interfacial thermal resistance between a carbon nanotube and molten salt molecules as well as between a silica nanoparticle and molten salt molecules. Hence, the optimum nanoparticle size was estimated for these nanofluids from the MD simulations.

2.4 Simulation Setup and Procedure (for Carbon Nanotube)

In this computational study the molecular dynamics simulation software package distributed by Sandia National Laboratories called “Large-scale Atomic/Molecular Massively Parallel Simulator” (LAMMPS) [48], was used to compute the interfacial thermal resistance between a carbon nanotube and the surrounding molten salt (Li_2CO_3 - K_2CO_3 , 62:38 by molar ratio).

The first step of the simulation is to construct a simulation domain. A commercial material modeling software package (Materials Studio ver 5.0, Accelrys) was used to construct the computational model for a single-walled carbon nanotube (5, 5; armchair lattice structure; 400 atoms). The nanotube was immersed into mixture of Li_2CO_3 and K_2CO_3 (9000 atoms) inside a simulation domain ($50.2 \text{ \AA} \times 50.2 \text{ \AA} \times 50.2 \text{ \AA}$). (Figure 1). The computational model for the MD simulations were developed using the general Lennard-Jones potential along with Coulombic terms for non-bonded interactions (Equation 1). For estimating the non-bonded interactions of the eutectic of

$\text{Li}_2\text{CO}_3\text{-K}_2\text{CO}_3$, Born-Mayer-Huggins potential was used (Equation 2). For bonded interactions, such as bond-stretching, bond-bending, and torsion, Equation (3) was used. All parameters for the non-bonded and bonded interactions were culled from the literature and are listed in Table 3.

The second step of the simulation is to minimize the potential energy of the system. For the energy minimization step the system temperature is decreased to 0 K. In this step non-physical situations are eliminated, such as repositioning any molecules, which are too close to each other or molecules that overlap. The system is then relaxed during NVE integration (micro-canonical ensemble), since the kinetic energy of the system is reduced to zero due to the minimization. During the micro-canonical ensemble, the system is thermally isolated and is supplied with constant magnitude of energy (E) which increases the velocity of atoms, resulting in temperature increase of the system, while the number of atoms (N) and the volume of the system (V) are fixed.

The third step of the simulation is to initialize the system to the starting temperature. During NPT integration (isobaric-isothermal ensemble), the number of the atoms and the pressure of the system are fixed, and the system is allowed to exchange energy with a large heat source at the given temperature. In this study, the starting temperature of the simulation is 800 K, since the melting point of the eutectic is at 761 K.

The last step is to initially increase the temperature of the nanotube up to a certain temperature (1200 K ~ 1500 K in this study) and to release the system during NVE integration. The nanotube then loses heat to the surrounding eutectic and the rate of the temperature decay is monitored for a period of time.

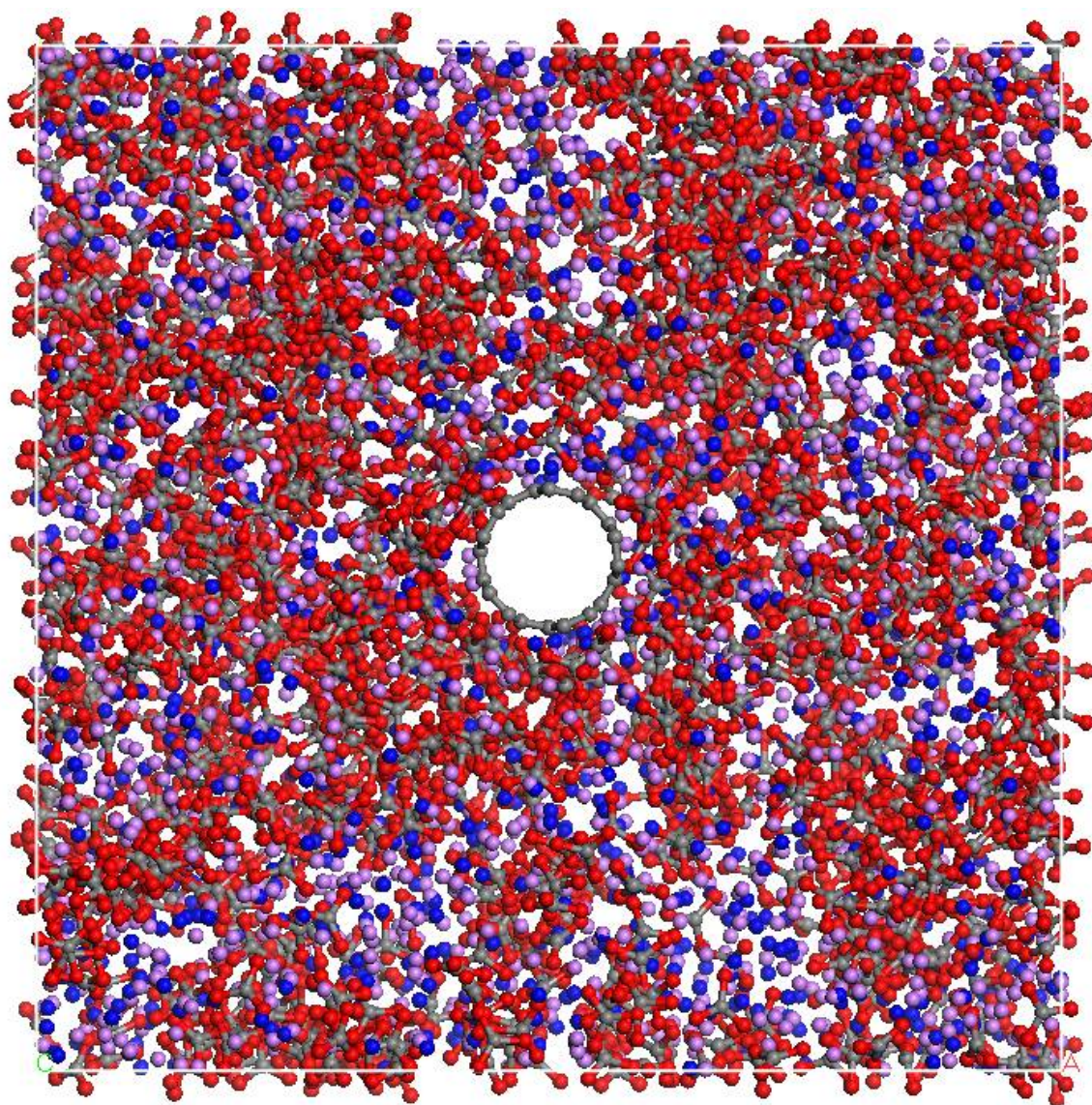


Figure 1. The simulation domain used in this study. It consists of a single walled (5,5) carbon nanotube (CNT) lattice consisting of 400 Carbon atoms and the eutectic of Li_2CO_3 and K_2CO_3 (9000 atoms).

Table 3. Parameters for potential fields for the MD simulations performed in this study. CNT Parameters were collected from Material Studio (ver 5.0, Accelrys, Inc.). Eutectic parameters were obtained from Costa [44] and Braybrook et al. [45], respectively. (C=0 and D=0 for Born-Mayer-Huggins potential)

Short range parameters					Bonding force constants			
Interaction	ϵ (kcal/mol)	σ (Å)	Charge		Bond-stretching	k_s	r_0	
C-C (CNT)	0.148	3.617	0		CNT	480.00000	1.3400	
					carbonate	4612.0000	1.2900	
Interaction	A(kcal/mol)	ρ (Å)	Σ (Å)	Charge	Bond-bending	k_b	θ_0	
C-C (carbonate)	3.27	0.290	2.66	+1.54	CNT	90.000000	120.00	
					carbonate	107.43539	120.00	
O-O	10.96	0.290	2.20	-1.18	torsional	k_t	D	N
Li-Li	9.73	0.290	1.54	+1	CNT	12.370000	-1.00	2
K-K	6.08	0.290	2.78	+1				
					carbonate	1.1392000	-1.00	0

2.5 Simulation Setup and Procedure (for Silica Nanoparticle)

The simulation procedures used to obtain the results presented in this section are described in Section 2.4. Three simulation domains were created with different silica nanoparticle size. Domain #1 (Figure 2) consists of 234 atoms of silica nanoparticle

(d=1.8 nm), 4464 atoms of Li_2CO_3 , and 2736 atoms of K_2CO_3 . Domain #2 consists of 321 atoms of silica nanoparticle (d=2.0 nm), 5952 atoms of Li_2CO_3 , and 3648 atoms of K_2CO_3 . Domain #3 consists of 114 atoms of silica nanoparticle (d=1.4 nm), 4464 atoms of Li_2CO_3 , and 2736 atoms of K_2CO_3 . The MD model was developed using Buckingham potential shown as:

$$E = \frac{q_i q_j}{r} + A e^{-\frac{r}{\rho}} - \frac{C}{r^6} \quad (13)$$

All parameters for the non-bonded and bonded interactions were culled from the literature and are listed in Table 4. The simulation procedure is the same as described in section 2.4.

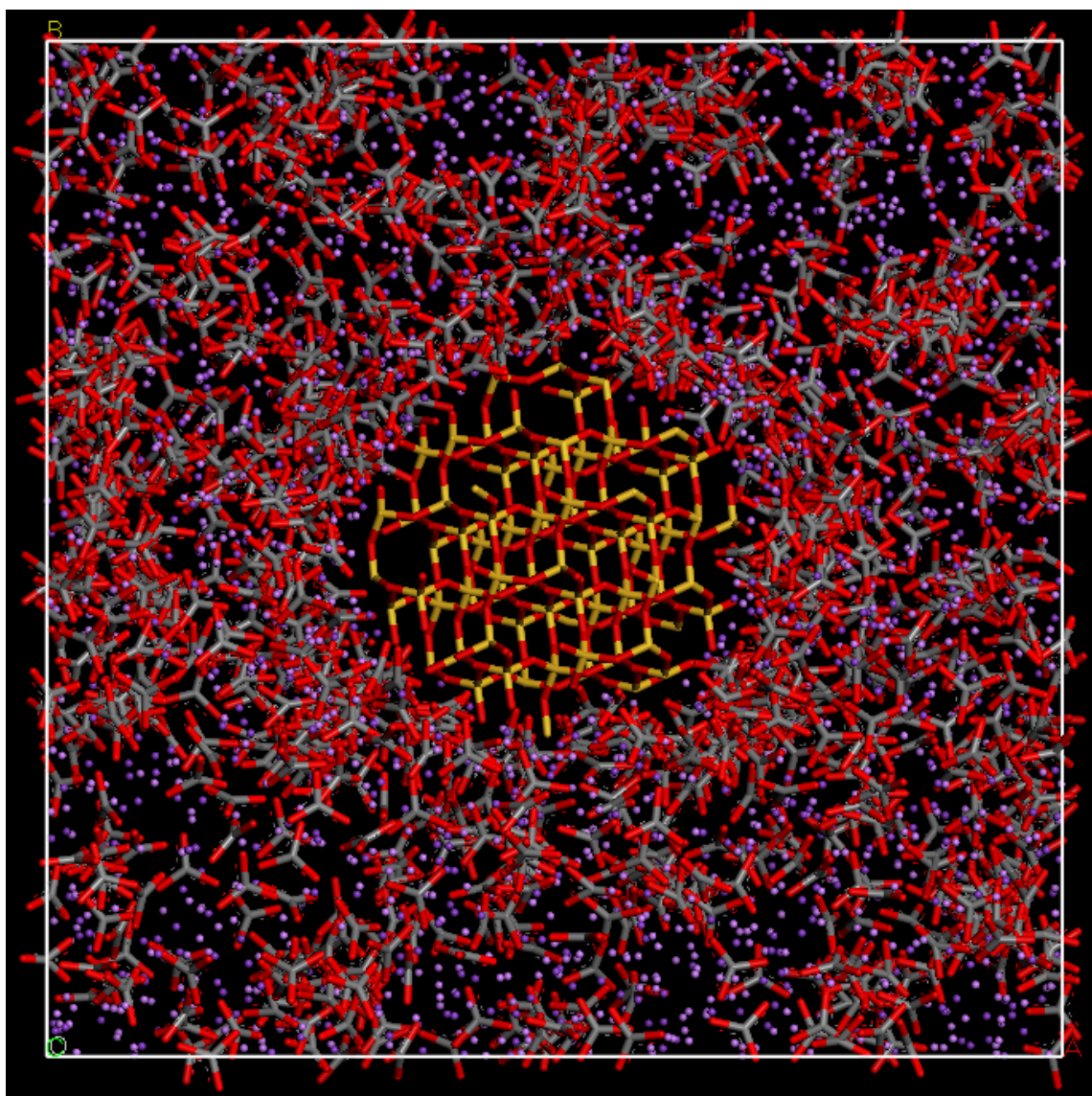


Figure 2. The simulation domain used in this study. It consists of a silica nanoparticle consisting of 234 atoms and the eutectic of Li_2CO_3 and K_2CO_3 (7200 atoms).

Table 4. Parameters for potential fields for the MD simulations performed in this study. SiO₂ Parameters were collected from Tsuneyuki et al. [49] and eutectic parameters were obtained from Costa [44] and Braybrook et al. [45], respectively. Other parameters were collected from Material Studio (Accelrys, Inc., ver. 4.4).

Non-bonded interaction				Bonded interaction			
Interaction	A(kcal/mol)	ρ (\AA^{-1})	Charge	Bond-stretching	k_s	r_0	
Si-Si	27010.0300	0.290	+2.40	SiO ₂	392.8000	1.665	
O-O (SiO ₂)	31587.0235	0.290	-1.20	CO ₃	18448.00	1.290	
C-C	21673.8181	0.290	+1.54	Bond-bending	k_b	θ_0	
O-O (CO ₃)	31587.0235	0.290	-1.18	SiO ₂	42.30000	113.1	
Li-Li	1974.70501	0.290	+1.00	SiO ₂	31.10000	149.8	
K-K	88980.3354	0.290	+1.00	CO ₃	429.7415	120.0	
				Torsional	k_t	d_t	ϕ_t
				SiO ₂	0.300000	1.000	3
				Improper	k_i	d_i	ϕ_i
				SiO ₂	26.26995	-1.000	2
				CO ₃	26.26995	-1.000	2

3. COMPUTATIONAL RESULTS AND DISCUSSIONS

3.1 Interfacial Thermal Resistance and CNT Size Limit

Molecular dynamics simulations were performed to compute the interfacial thermal resistance between a carbon nanotube (CNT) and the surrounding molten salt molecules. The initial CNT temperature was chosen to be 1400 K and 800 K was chosen to be the initial molten salt temperature. The initial difference in temperature is thus 600 K. The decay of the temperature difference between the CNT and the molten salt was monitored as a function of time. Three additional simulations were performed to investigate the effect of the initial temperature difference (400 K, 500 K, and 700 K). Moreover, two more simulations were performed using smaller number of atoms (9400 atoms \rightarrow 4800 atoms) and using a larger CNT size (6.72 Å \rightarrow 9.49 Å in diameter) in order to investigate the effect of the number of atoms and the CNT size on the interfacial thermal resistance, respectively.

Temperature change of the CNT and the molten salt as a function of time are shown in Figure 3. As shown in the figure, the temperature of the CNT gradually decreased with time, while the temperature of the molten salt remained almost constant at 800 K. Figure 4 shows that logarithm of difference in temperature between the CNT and the molten salt. As shown in Figure 4, the temperature difference exponentially decreased and the time constant is obtained from the inverse of the slope of the plot. Based on the time constant, the interfacial thermal resistance between the CNT and the

molten salt can be computed using Equation 6 and the results are shown in Figure 5 and Table 5.

The optimum CNT size can be computed using Equation (9) based on the value of the interfacial thermal resistance. The lower limit of the CNT diameter is shown in Table 5. The interfacial thermal resistance between the CNT and the molten salt ranged from $4.0 \times 10^{-8} \text{ m}^2\text{K/W}$ to $5.2 \times 10^{-8} \text{ m}^2\text{K/W}$. The corresponding CNT diameter is 60 ~ 80 nm. Moreover, the results also demonstrate that the interfacial thermal resistance is independent of the temperature difference or the size of the CNT. The results from another simulation using lower number of atoms were also in good agreement with the previous simulations ($R_b = 5.1 \times 10^{-8} \text{ m}^2\text{K/W}$).

In addition, from the simulation results a density plot was generated to visualize the spatial variation of density within the simulation domain. The density plot along the radial direction from the CNT surface is shown in Figure 6. The first peak at the CNT surface is the carbon atoms at the wall of the CNT. The peak at 3 Å indicates the formation of a layer of molten salt molecules on the surface of the CNT. According to the literature [50], layering of the liquid molecules is one of the factors for the enhanced

effective thermal conductivity of the nanofluids. Furthermore, the peak at 3\AA using small CNT (6.97 \AA in diameter) is identical to that using the bigger CNT (9.49 \AA in diameter), which implies that the formation of the compressed layer (higher density layer) of the liquid molecules around the individual CNT crystals is independent of the size of the individual nanoparticle. It depends on the interaction (potential field) between carbon atoms at the surface of CNT and the liquid molecules (in the molten salt). This is also consistent with the previous statement that the interfacial thermal resistance is independent of the size of the CNT.

Figure 7 shows atomic concentration of each atom that was predicted by the simulation. It was observed that the chemical composition of the Li_2CO_3 molecules and K_2CO_3 molecules in the compressed layer is different from that of the bulk of the eutectic (solvent phase). Since the eutectic has the lowest melting point, the compressed layer is expected to melt at higher temperature than the bulk phase of the eutectic. This result from the numerical models therefore implies the existence of compressed (semi-solid) layer surrounding nanoparticles in the nanofluids.

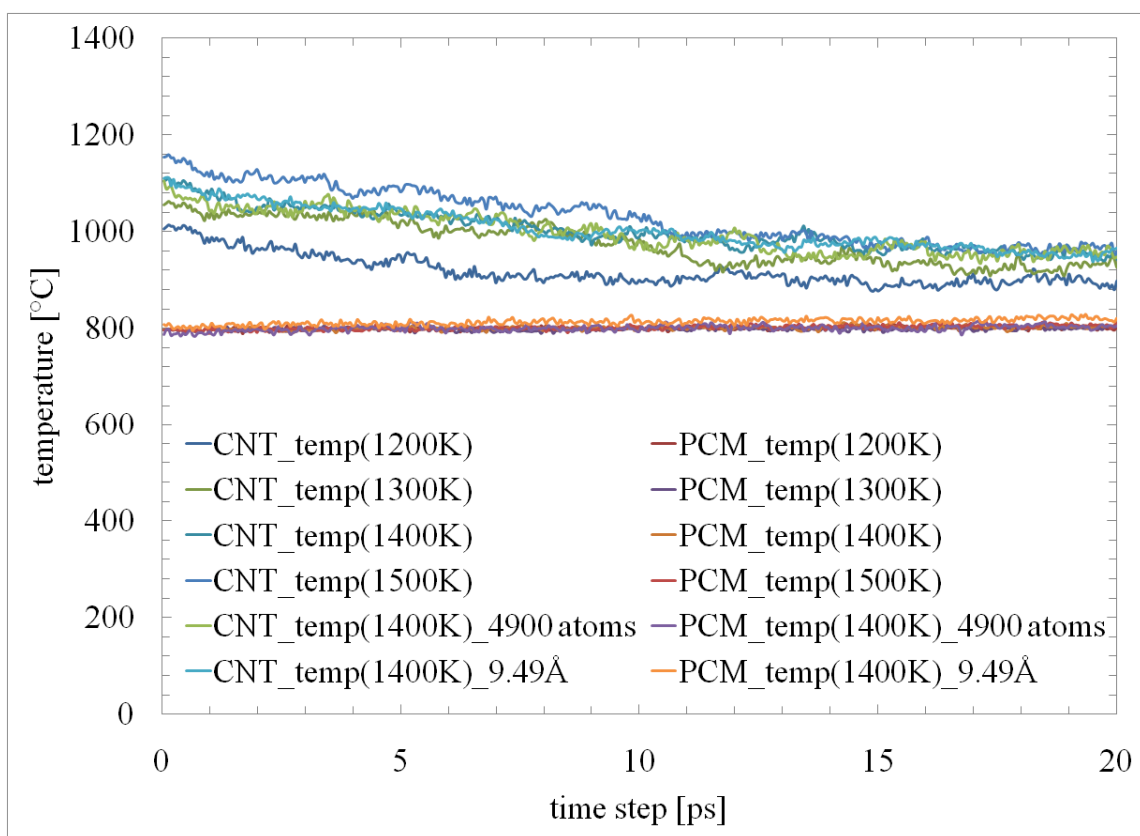


Figure 3. Plot of temperature decay of the CNT as a function of time.

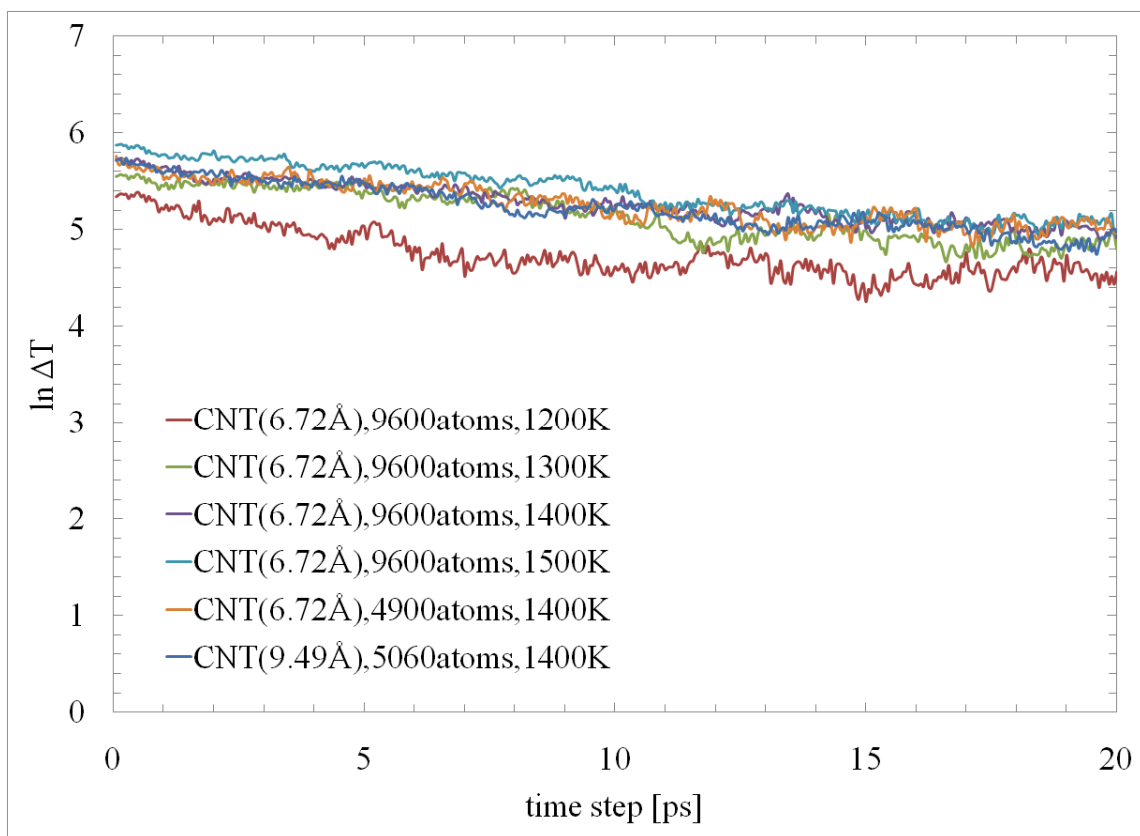


Figure 4. Semi-log graph of the temperature difference between the CNT and the molten salt. Inverse of the slope is the time constant required to compute the interfacial thermal resistance. (Equation 6)

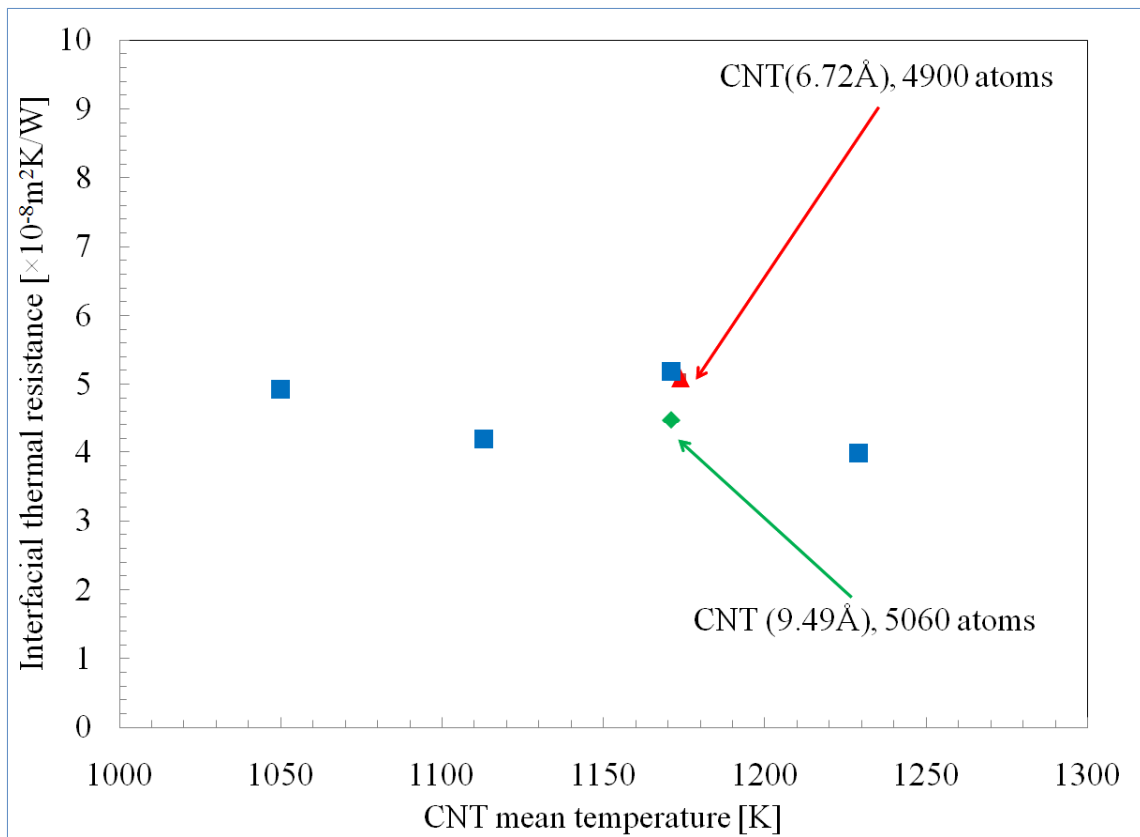


Figure 5. The interfacial thermal resistance between the CNT and the molten salt. No significant difference was observed for the variations in the values of the different parameters such as the initial temperature of the nanoparticle, the number of the atoms, and the size of the CNT.

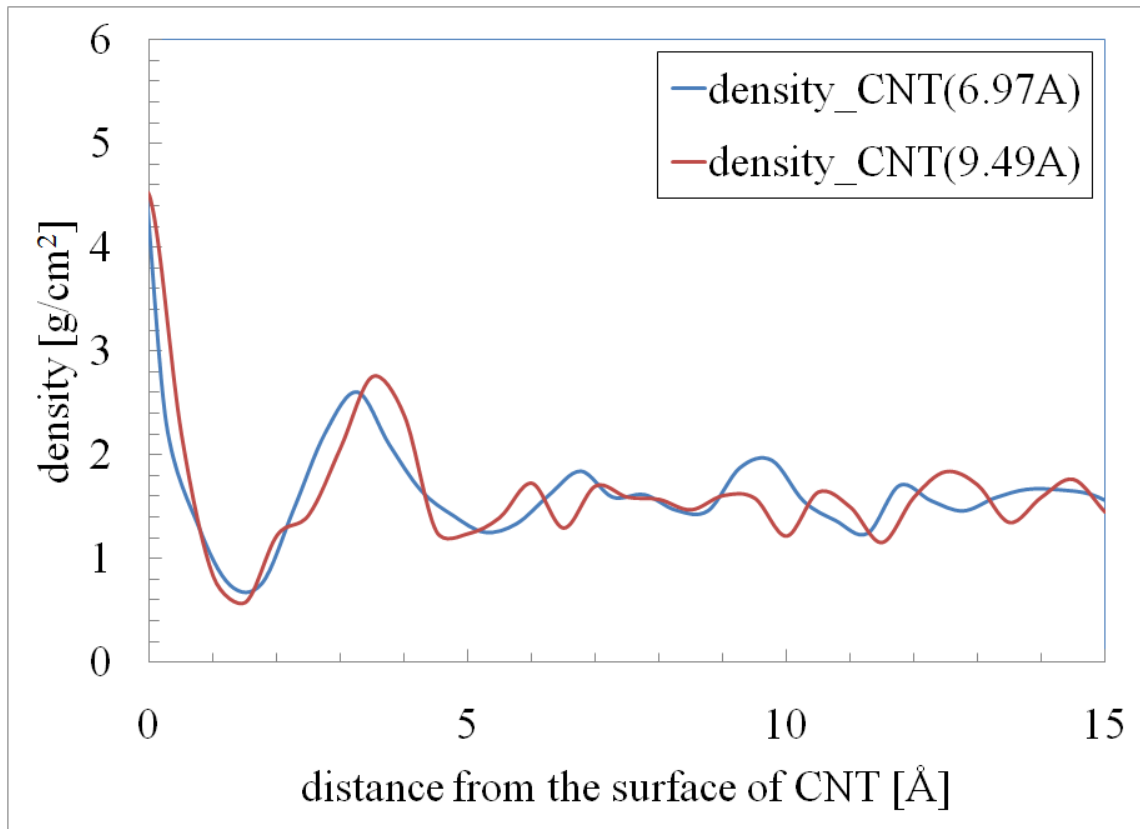


Figure 6. Density plot of the CNT / molten salt nanofluid.

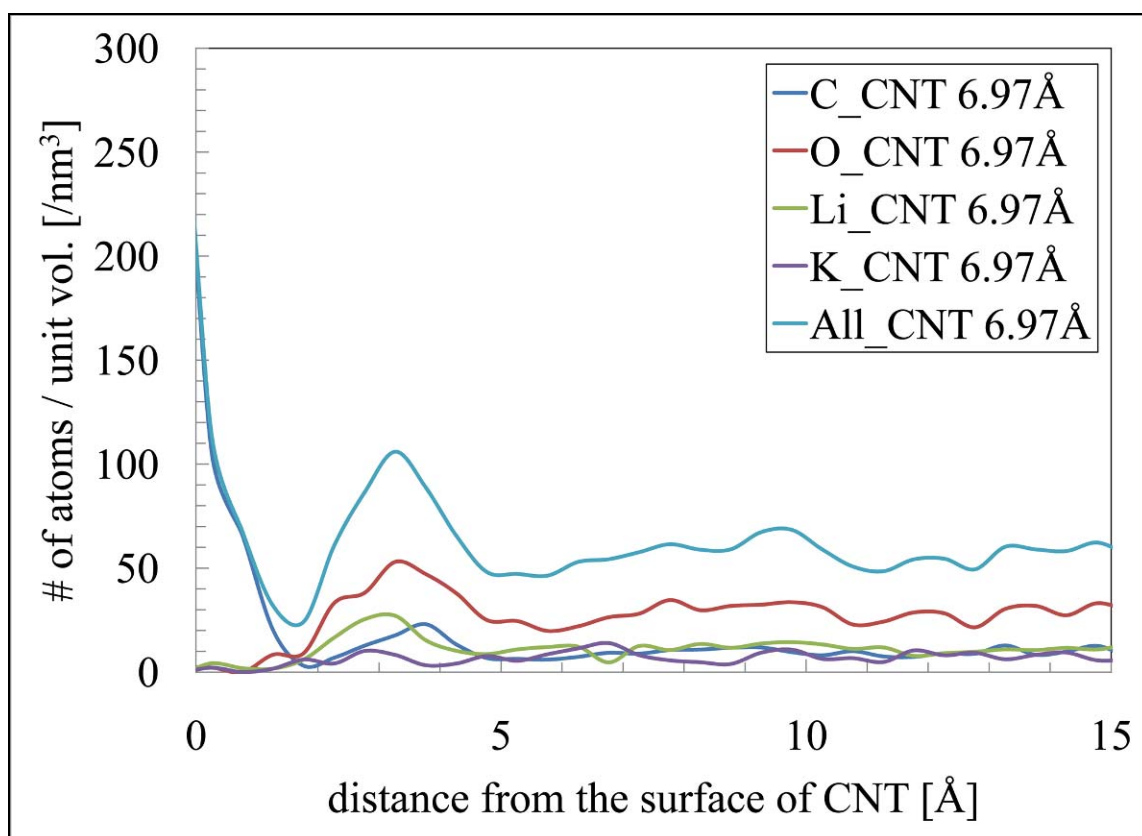


Figure 7. Spatial distribution of atomic concentration of different elements within the simulation domain which contains CNT of 6.97 Å diameter.

Table 5. Interfacial thermal resistance and the corresponding value for optimum size of CNT obtained from each simulation.

Initial condition (Initial temperature and number of solvent atoms)	Final temperature (after 20 ps)	Slope	τ (ps)	R_b ($\times 10^{-8}$ $\text{m}^2\text{K/W}$)	d_c (nm)
CNT(6.72Å) 1200K, 9400atoms	CNT 899 K	-0.0362	27.62	4.93	74
CNT(6.72Å) 1300K, 9400atoms	CNT 926 K	-0.0426	23.47	4.19	63
CNT(6.72Å) 1400K, 9400atoms	CNT 942 K	-0.0344	29.07	5.19	78
CNT(6.72Å) 1500K, 9400atoms	CNT 958 K	-0.0447	22.37	3.99	60
CNT(6.72Å) 1400K, 4800atoms	CNT 948 K	-0.0351	28.49	5.09	76
CNT(9.49Å) 1400K, 5060atoms	CNT 942 K	-0.0399	25.06	4.48	67

3.2 Interfacial Thermal Resistance and Silica Size Limit

Molecular dynamics simulations were performed to compute the interfacial thermal resistance between a silica nanoparticle (1.8 nm) and the surrounding molten salt molecules. The initial temperature of silica nanoparticle was chosen to be 1400 K and the initial temperature of the molten salt was chosen to be 800 K. Hence, the initial difference in temperature is 600 K. The decay of the temperature difference between the silica and the molten salt was monitored as a function of time. Three additional simulations were performed to investigate the effect of the initial temperature difference (400 K, 500 K, 700 K, and 800 K). Moreover, two more simulations were performed using a smaller silica nanoparticle (1.4 nm) and a larger silica nanoparticle (2.0 nm) in order to investigate the effect of the nanoparticle size on the interfacial thermal resistance, respectively.

Temperature change of the silica nanoparticle and the molten salt within the simulation domain are shown in Figure 8. As shown in the figure, the temperature of the silica nanoparticle gradually decreased with time, while the temperature of the molten salt remained virtually unchanged at 800 K. Based on the time constant, the interfacial thermal resistance between the silica nanoparticle and the molten salt can be computed using Equation 6 and the results are shown in Figure 9 and Table 6.

The optimum size of the silica nanoparticle can be computed using Equation (12) based on the value of the interfacial thermal resistance and is shown in Figure 10 and also listed in Table 6. The interfacial thermal resistance between the silica nanoparticle

and the molten salt ranged from $6.3 \times 10^{-8} \text{ m}^2\text{K/W}$ to $7.6 \times 10^{-8} \text{ m}^2\text{K/W}$. The corresponding value of the optimum diameter of the silica nanoparticle is 22 ~ 26 nm. Moreover, the results also demonstrate that the interfacial thermal resistance is independent of the temperature or the size of the silica nanoparticle.

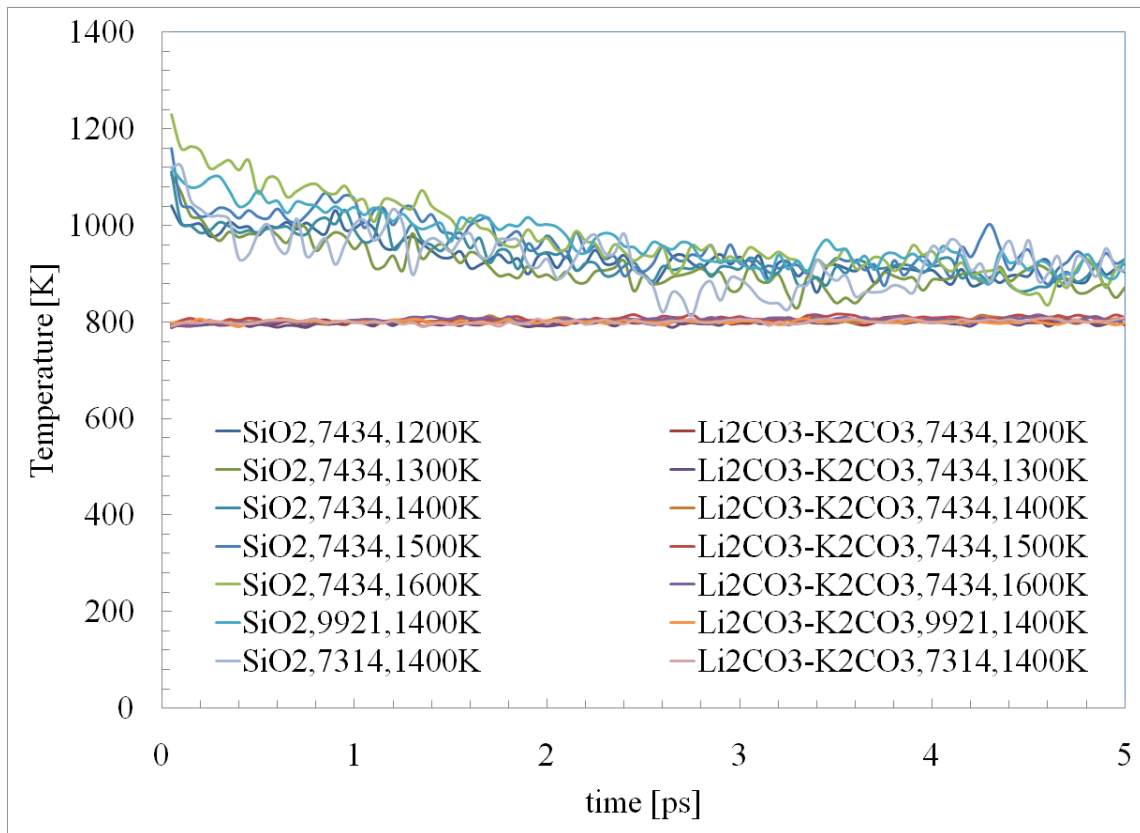


Figure 8. Temperature decay of the silica nanoparticle as a function of time.

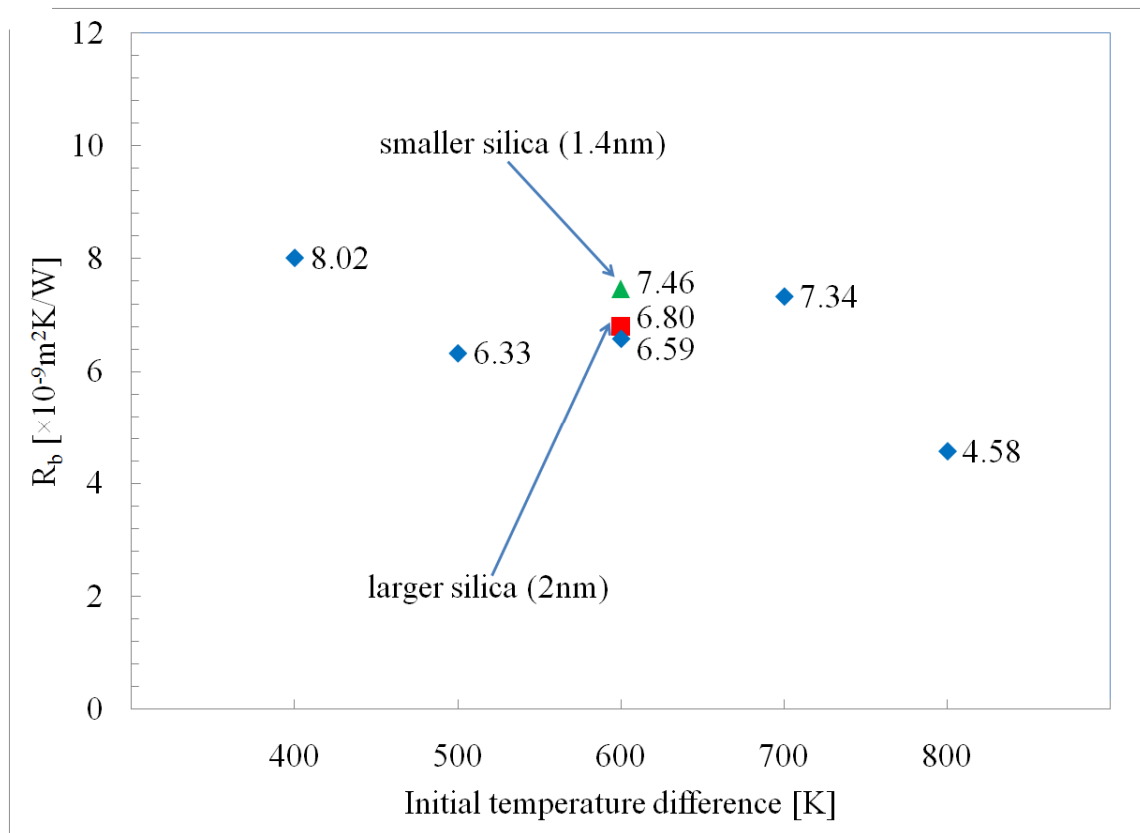


Figure 9. The interfacial thermal resistance between the silica nanoparticle and the molten salt. No significant difference was observed for the predicted results for variations in the size of the silica nanoparticle. The initial temperature difference ranged from 500 ~ 700 K.

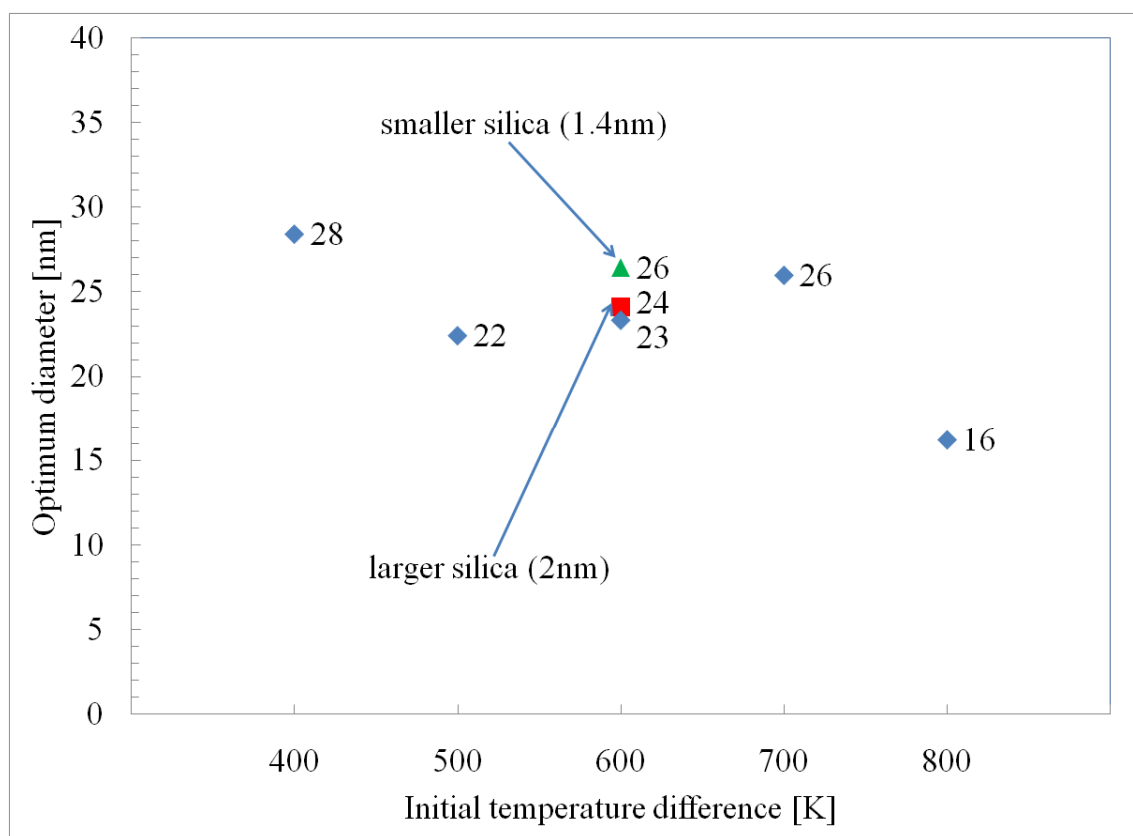


Figure 10. The optimum size of the silica nanoparticle was computed using Equation (12) and was predicted by this numerical model to be 22 ~ 26 nm.

Table 6. Interfacial thermal resistance and the corresponding value for the optimum size of the silica nanoparticle for each simulation.

Number of atoms	Initial temp. difference	Time constant	Interfacial thermal resistance	Optimum diameter
7434	400 K	5.692 ps	$8.02 \times 10^{-9} \text{ m}^2\text{K/W}$	28 nm
7434	500 K	4.492 ps	$6.33 \times 10^{-9} \text{ m}^2\text{K/W}$	22 nm
7434	600 K	4.675 ps	$6.59 \times 10^{-9} \text{ m}^2\text{K/W}$	23 nm
7434	700 K	5.206 ps	$7.34 \times 10^{-9} \text{ m}^2\text{K/W}$	26 nm
7434	800 K	3.249 ps	$4.58 \times 10^{-9} \text{ m}^2\text{K/W}$	16 nm
9921	600 K	4.824 ps	$6.80 \times 10^{-9} \text{ m}^2\text{K/W}$	24 nm
7314	600 K	5.297 ps	$7.46 \times 10^{-9} \text{ m}^2\text{K/W}$	26 nm

3.3 Summary

In summary, molecular dynamics simulations were performed to compute the interfacial thermal resistance (R_b) between a carbon nanotube (and a silica nanoparticle) and molten salt. Since nanoparticles have exceptionally large specific surface area (per unit volume), the interfacial thermal resistance can significantly modify the effective thermal properties of the nanomaterial. Especially, high interfacial thermal resistance acts as a thermal barrier and hinders the enhancement of the effective thermal conductivity of the nanofluid. However, the measurement of the resistance is not easily amenable for experimentation. MD simulations were performed to estimate the

interfacial thermal resistance. Based on the calculated value of the interfacial thermal resistance, the optimum size of the CNT and silica nanoparticle was calculated. The interfacial thermal resistance between the CNT and the molten salt was computed to be $4.65 \times 10^{-8} \text{ m}^2 \text{KW}^{-1}$. The optimum size of the CNT was obtained in this study and ranges from 60 nm ~ 80 nm. The interfacial thermal resistance between the silica nanoparticle and the molten salt was computed to be $7.0 \times 10^{-8} \text{ m}^2 \text{KW}^{-1}$. The optimum size of the silica nanoparticle was obtained in this study and ranges from 22 nm ~ 26 nm.

The interfacial thermal resistance was found to be independent of the size of the CNT and the silica nanoparticle. Moreover, the computational simulations alluded to the formation of a higher density phase of the solvent molecules on the surface of the nanoparticles. This higher density phase (or semi-solid layering) of liquid molecules is expected to modify the thermal interfacial resistance (or Kapitza resistance) between the individual nanoparticles and the solvent molecules, which can also serve as an additional mechanism for storage of energy (internal energy) for the nanomaterial.

4. EXPERIMENTAL STUDY

4.1 Synthesis of Molten Salt Nanomaterials

Molten salt nanomaterials were synthesized by using liquid solution method. Eutectic of Li_2CO_3 - K_2CO_3 (62:38 by molar ratio) and eutectic of BaCl_2 - NaCl - CaCl_2 - LiCl (15.9:20.5:34.5:29.1 by molar ratio) were chosen for the base molten salts and procured from Sigma Aldrich, Co and Spectrum Scientific, Co. SiO_2 nanoparticles were chosen as the additives. SiO_2 nanoparticles were procured from Meliorum Tech. The procedure to synthesize the molten salt nanomaterials is shown schematically in Figure 11. For synthesizing nanomaterial samples at 1 % mass concentration, 2.0 mg of nanoparticles and 198.0 mg of molten salt eutectic were measured precisely using a microbalance (CPA26P, Sartorius AG). The mixture of the nanoparticles and the molten salt eutectic were dissolved in 20 ml of distilled water in a glass bottle (25 ml). The bottle was ultra-sonicated for 200 minutes by an ultra sonicator (Brandson 3510, Brandson Ultrasonics Co.) to homogenize the dispersion of the nanoparticles and the molten salt eutectic. The water solution was then heated on a hot plate (C-MAG HP7, IKA), which was maintained at 200 °C (Figure 11). The dried nanomaterial (which is termed as the nanocomposite in the solid phase, and is termed as the nanofluid in the liquid phase) was then heated to 300 °C for 2 hours to remove the residual chemically bonded water from the nanomaterial. All procedures were performed in a glove box with

filtered clean air circulation for rapid evaporation of the water as well as to minimize any contamination of the samples.

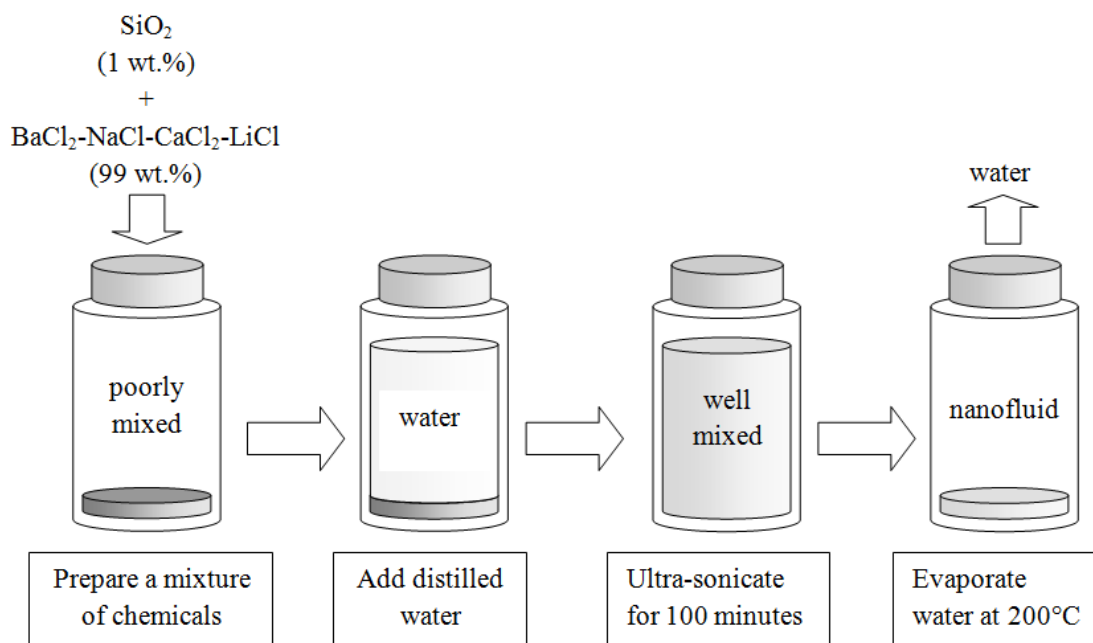


Figure 11. Schematic showing the procedure to synthesize eutectic salt nanomaterial.

4.2 Specific Heat Capacity Measurement

The specific heat capacity measurement was performed using a differential scanning calorimeter (DSC, Q20 TA Instruments, Inc). Tzero hermetic pans and lids were used to store the nanomaterial samples in order to prevent any potential weight loss during the thermal cycling in the DSC (i.e., during repeated melting and solidification for the designed thermal cycles). A customized testing protocol was programmed and implemented in the DSC instrument, to conform to the standard DSC testing method

(ASTM-E1269). The testing protocol was implemented as follows: (1) Initially, the temperature of the sample was maintained at 150 °C for 10 minutes to ensure that steady state thermal conditions were obtained. (2) The sample was then heated at a fixed ramping rate of 20 °C / minute up to 560 °C (this corresponds approximately to the initial creep temperature of stainless steel which is used as a structural material in CSP). The temperature of the sample was then maintained at 560 °C for another 10 minutes for achieving steady state conditions. (3) The sample was then cooled successively using nitrogen and air supply until a temperature of 100 °C was achieved. These three steps were repeated successively 4 ~ 12 times to verify the repeatability of the measurements for each sample. In order to compute the specific heat capacity of the sample, a sapphire standard (25.938 mg) was subjected to thermal cycling in the same manner and the difference in the heat flux was measured as a function of temperature (control measurements). The difference in weight between the sample and the sapphire was then calculated. The specific heat capacity of the sample was then computed by taking the ratio of the differential heat transfer and correcting for the difference in weight of the sample and the sapphire standard. To verify the validity of the specific heat capacity measurements, the pure molten salt eutectic sample was tested following the same procedure and the specific heat capacity of the pure molten salt was compared with the literature data [5].

4.3 Electron Microscopy Analysis

In this study, two scanning electron microscopes (SEM; FEI Quanta 600 FE-SEM, JEOL JSM-7500F) were used to analyze the microstructure of the sample. Furthermore, nanoparticles have a propensity to agglomerate under certain conditions such as change in value of the pH of the solvent. Therefore, it is necessary to verify if the nanoparticles in the samples under consideration were agglomerated or not (before and after the thermal cycling experiments). In this study, a transmission electron microscope (TEM; JEOL JEM-2010) was used to verify that there was minimal agglomeration of the nanoparticles in the samples tested in this study.

4.4 Thermal Conductivity Measurement

Due to instrument limitations in measuring thermal conductivity at high temperatures, the thermal conductivity measurements were restricted to a temperature less than 300 °C. This temperature corresponds to the solid phase of the nanomaterial (nanocomposite). Hence the thermal conductivity of only the nanocomposites were explored in this study. For the thermal conductivity measurements, the specific heat capacity of the pure molten salt and the nanocomposite was measured by using a differential scanning calorimeter (DSC; Q20, TA Instruments, Inc) for a temperature range of 150 °C - 300 °C. The pure molten salt samples and the nanocomposite samples were then shipped to Dynalene Inc for thermal diffusivity measurement using the laser

flash method (Instrument: LFA 447 Nanoflash, Netzsch Instruments N.A. LLC.). As mentioned before, the maximum operating temperature of this LFA instrument is restricted to below 300 °C. The thermal diffusivity measurements from the LFA instrument were then obtained from Dynalene Inc. The thermal conductivity of the samples was then calculated based on the density values listed in the literature, the measured specific heat capacity, and the measured thermal diffusivity of the samples.

5. EXPERIMENTAL RESULTS AND DISCUSSIONS*

5.1 SiO₂ / BaCl₂-NaCl-CaCl₂-LiCl Nanomaterial

Molten salt eutectic of BaCl₂-NaCl-CaCl₂-LiCl (15.9:20.5:34.5:29.1 by molar ratio) was mixed with SiO₂ nanoparticles and the nanomaterial samples were synthesized using the liquid solution method (described in the previous section). The mass concentration of SiO₂ nanoparticles was fixed at 1 %. Distilled water was added into the mixture and the mixture was ultra-sonicated to obtain a homogeneous dispersion of the nanoparticles in the aqueous solution of the eutectic salt. The water solution was then heated on a hot plate (C-MAG HP7, IKA), which was maintained at 200 °C. The dried nanomaterial (which is termed as the nanocomposite in solid phase, and is termed as the nanofluid in the liquid phase) was then heated at 300 °C for 2 hours to remove the residual chemically bonded water from the nanomaterial.

5.1.1 Specific heat capacity results

Two samples of the pure chloride eutectic and two samples of the nanomaterial at 1% mass concentration were synthesized individually and tested using the thermal

*Reprinted with permissions from “Enhanced specific heat of SiO₂ nanofluid” by D. Shin and D. Banerjee, 2011, Journal of Heat Transfer, 133, Copyright 2011 by ASME and from “Enhancement of specific heat capacity of high-temperature silica-nanofluids synthesized in alkali chloride salt eutectics for solar thermal-energy storage applications” by D. Shin and D. Banerjee, 2011, International Journal of Heat and Mass Transfer, 54, Copyright 2010 by Elsevier Ltd.

cycling protocols described in the previous section (Section 4). Figure 12 and Table 7 show the results for the specific heat capacity measurements for the pure eutectic samples and the nanocomposite samples for the lower temperature range below the melting point of the eutectic salt (155 ~ 315 °C). The average specific heat capacity of the nanocomposite at 1% mass concentration was enhanced by 6 ~ 7 % compared to that of the pure eutectic [37]. The measurement uncertainty for this data is estimated to be 0.7 % ~ 1.1 %. Figure 13 and Table 8 show results for the specific heat capacity measurements for the pure eutectic samples and the nanocomposite samples for the higher temperature range above the melting point of the eutectic salt (495 ~ 555 °C). The average specific heat capacity of the nanofluid was enhanced by 13 % ~ 16 % over that of the pure eutectic [37]. The measurement uncertainty for this data is 1.0 % ~ 1.1 %.

5.1.2 SEM / TEM analysis

Nanoparticles have the propensity to agglomerate and precipitate if certain experimental parameters (such as pH of the solvent) are not properly controlled. Hence, it is necessary to verify whether or not nanoparticles are well dispersed and have minimal level of agglomeration (or remain unagglomerated) before and after repeated thermal cycling in the DSC. The high temperature nanomaterial samples underwent repeated melting / solidification, and therefore it was necessary to confirm that the nanoparticles remained agglomerated and well dispersed after the measurements were performed. Figure 14 is an SEM image of the nanomaterial before melting /

solidification in the DSC, while Figure 15 is an SEM image of the nanomaterial after melting / solidification several times in the DSC. Figure 15 shows that the thermal cycling in the DSC did not cause any significant agglomeration of the nanoparticles in the synthesized nanomaterial. The average diameter of SiO_2 nanoparticles before the thermal cycling is ~ 26 nm and that after the thermal cycling is ~ 27 nm. Figure 14 and 15 also show that the nanoparticles are uniformly dispersed in the nanomaterial before and after testing in the DSC. Furthermore, Figure 15 shows that a network substructure forms in the nanomaterial (similar to a percolation network). The substructure seems to interconnect the SiO_2 nanoparticles, thus forming an interconnected network. For comparison, a SEM image of the pure eutectic after multiple thermal cycling is presented in Figure 16. The interconnected network was not observed in the pure eutectic salt (neat solvent material).

5.2 SiO_2 / Li_2CO_3 - K_2CO_3 Nanomaterial

Molten salt (Li_2CO_3 - K_2CO_3)-based SiO_2 nanomaterial was synthesized by the liquid solution method. The mass concentration of SiO_2 nanoparticles was fixed at 1 %. Distilled water was added to the mixture and the resulting solution was ultrasonicated to obtain a homogeneous dispersion of the nanoparticles in the aqueous solution of the eutectic salt. The water was evaporated from a glass vial placed on a hot plate (C-MAG HP7, IKA) which was maintained at 200°C . After complete evaporation, the dried nanomaterial (which is termed as the nanocomposite in the solid phase, and is termed as

the nanofluid in the liquid phase) was then heated to 300 °C for 2 hours to remove the residual chemically bonded water from the nanomaterial (i.e., the chemically hydrated salt).

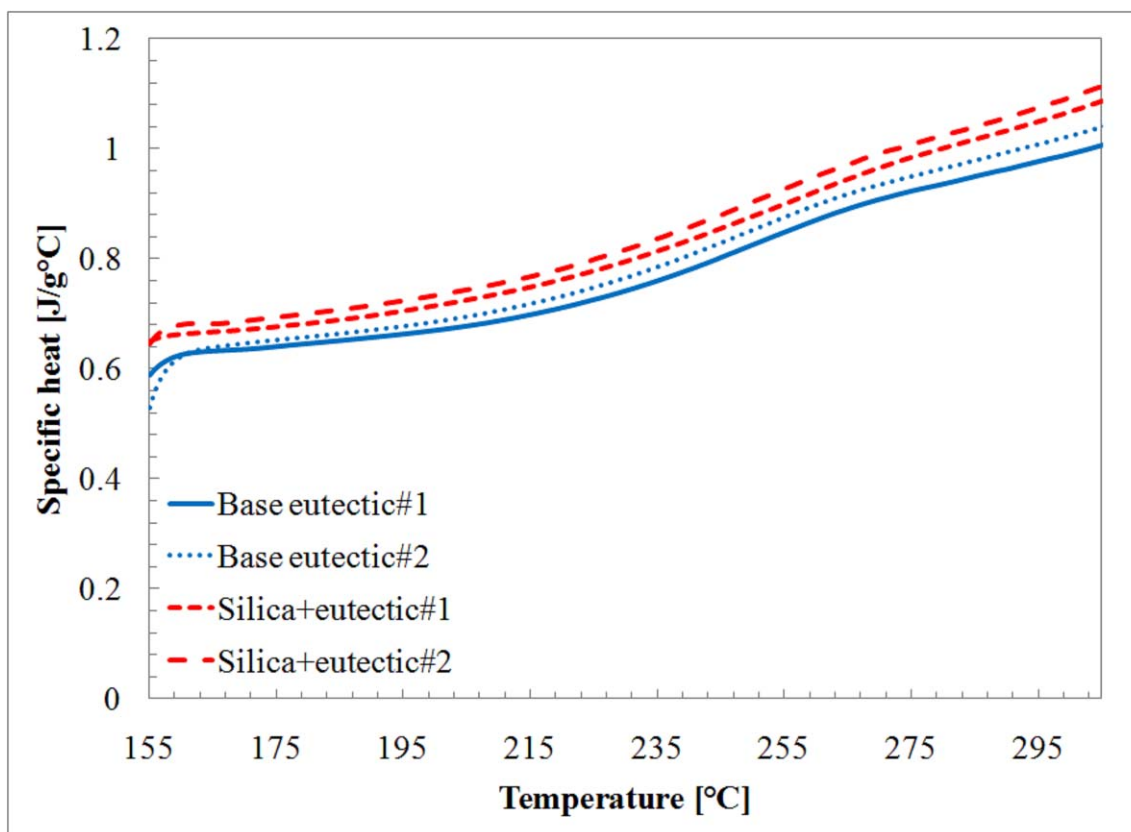


Figure 12. Variation of specific heat capacity with temperature (155 °C ~ 315 °C) for pure eutectic salt of $\text{BaCl}_2\text{-NaCl-CaCl}_2\text{-LiCl}$ and the corresponding SiO_2 nanocomposite samples [37].

Table 7. Specific heat capacity measurements (J /g-K) of pure eutectic salt of BaCl₂-NaCl-CaCl₂-LiCl and the corresponding SiO₂ nanocomposite samples. Average specific heat capacity measurements (J /g-K) of the pure eutectic and the nanocomposite at solid phase (155 ~ 315 °C) are listed here. The average specific heat capacity of the nanocomposite was enhanced by 6 ~ 7 % compared with that of the pure eutectic [37]. (ϵ : standard deviation for all the thermo-cycle data for a sample).

C _p (J/g-K)	Pure eutectic #1	Pure eutectic #2	Nanocomposite #1	Nanocomposite #2
1 st run	0.764	0.786	0.837	0.781
2 nd run	0.757	0.805	0.839	0.830
3 rd run	0.773	0.815	0.849	0.845
4 th run	0.790	0.818	0.852	0.879
5 th run	0.812			0.894
6 th run	0.829			0.896
Average	0.788	0.806	0.844	0.854
Enhancement	-	-	6.0 %	7.2 %
ϵ	0.028	0.015	0.007	0.045

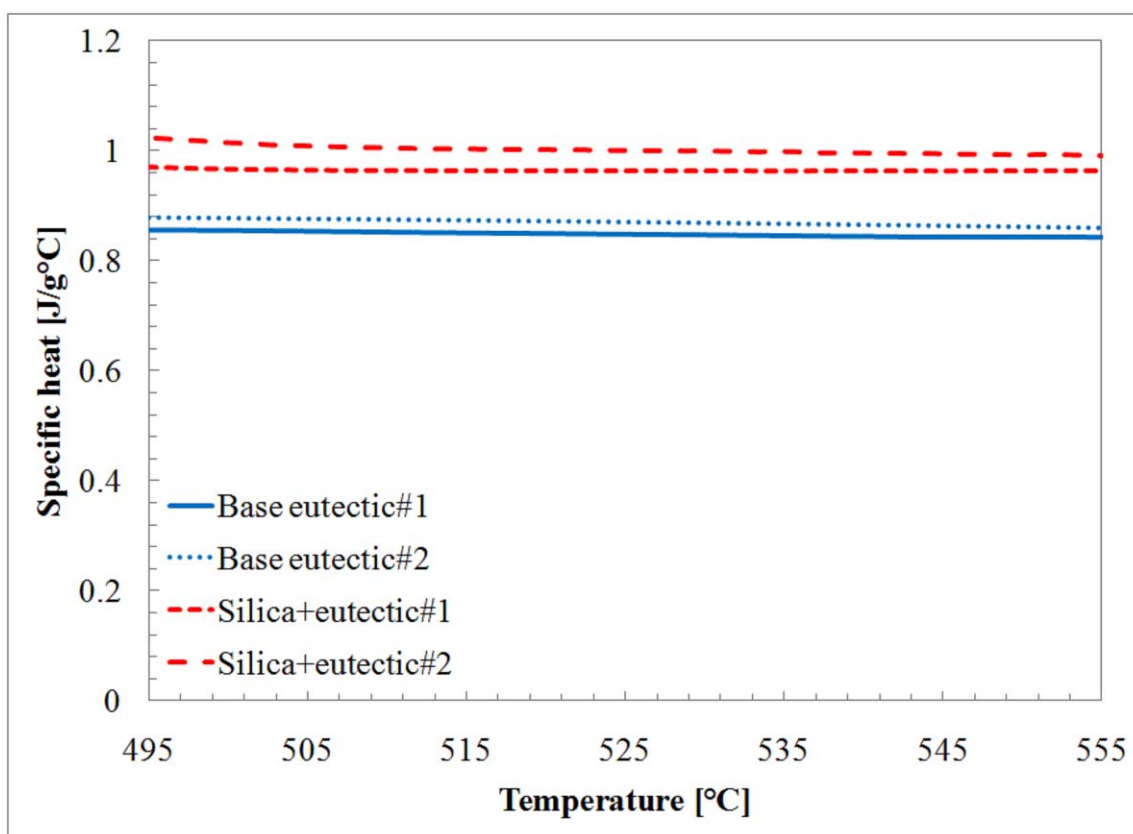


Figure 13. Variation of specific heat capacity with temperature (495 $^\circ\text{C}$ ~ 555 $^\circ\text{C}$) for pure eutectic salt of $\text{BaCl}_2\text{-NaCl-CaCl}_2\text{-LiCl}$ and the corresponding SiO_2 nanocomposite samples [37].

Table 8. Specific heat capacity measurements (J /g-K) of pure eutectic salt of BaCl₂-NaCl-CaCl₂-LiCl and the corresponding SiO₂ nanofluid samples. Average specific heat capacity measurements (J /g-K) of the pure eutectic and the nanofluid (495 ~ 555 °C) are listed here. The average specific heat capacity of the nanofluid samples were enhanced by 13 % ~ 16 % compared with that of the pure eutectic [37]. (ε : standard deviation for all the thermo-cycle data for a sample).

C_p (J/g-K)	Pure eutectic #1	Pure eutectic #2	Nanofluid #1	Nanofluid #2
1 st run	0.818	0.830	0.937	0.931
2 nd run	0.804	0.856	0.959	0.957
3 rd run	0.826	0.869	0.962	0.986
4 th run	0.845	0.885	0.975	1.021
5 th run	0.873			1.033
6 th run	0.896			1.020
Average	0.844	0.860	0.958	0.991
Enhancement	-	-	12.5 %	16.3 %
ε	0.035	0.023	0.016	0.041

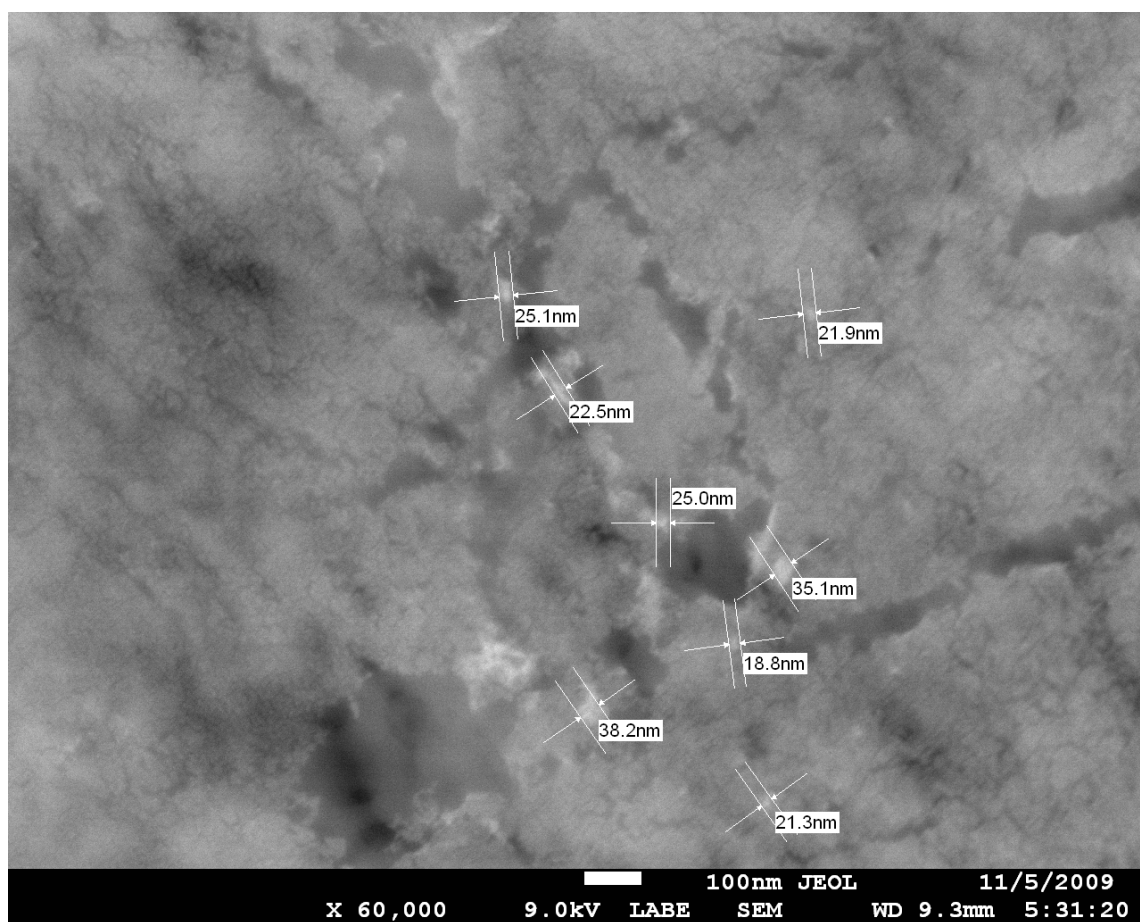


Figure 14. SEM image of $\text{SiO}_2/\text{BaCl}_2\text{-NaCl-CaCl}_2\text{-LiCl}$ nanomaterial before melting in the DSC. The average diameter of SiO_2 nanoparticles is ~ 26 nm. The nanoparticles are uniformly dispersed and no agglomeration is observed [37].

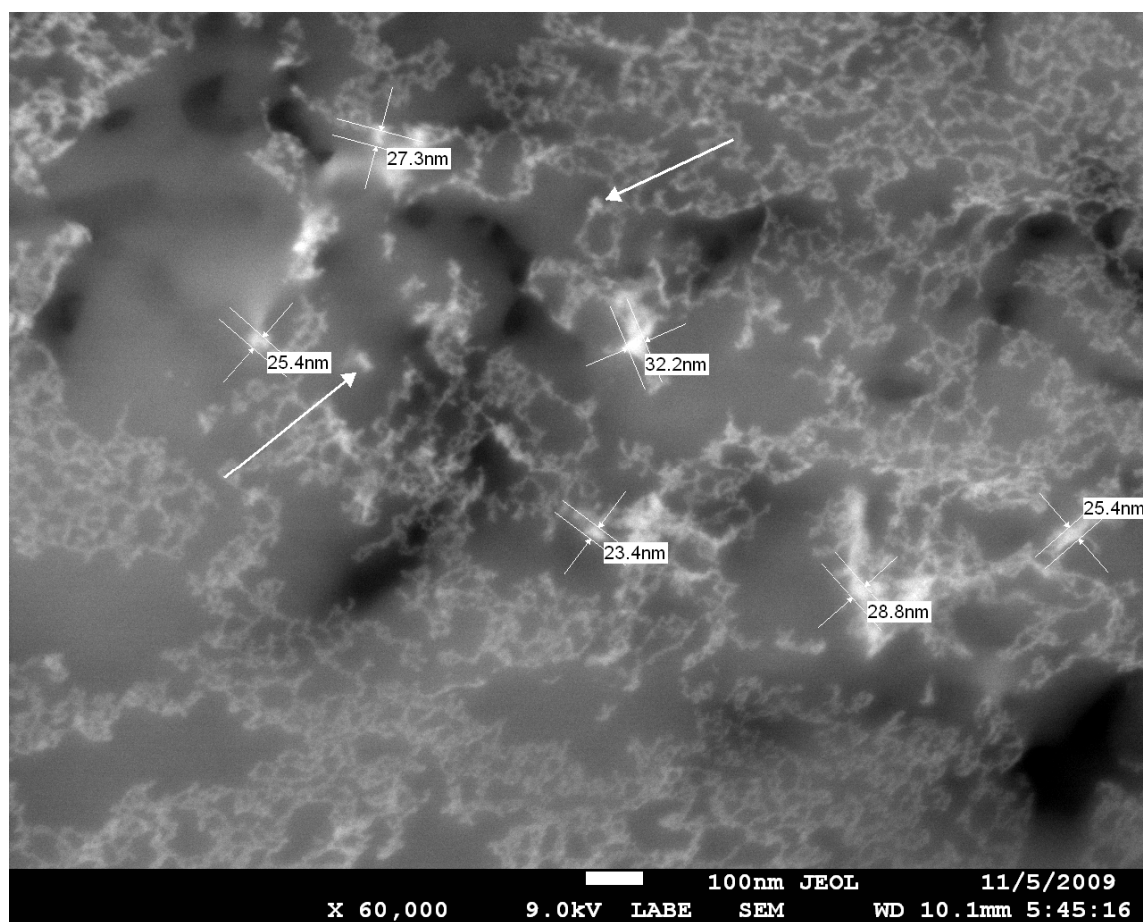


Figure 15. SEM image of $\text{SiO}_2/\text{BaCl}_2\text{-NaCl-CaCl}_2\text{-LiCl}$ nanomaterial after repeated thermal cycling involving melting and solidification in the DSC. The average diameter of SiO_2 nanoparticles is ~ 27 nm. The nanoparticles are uniformly dispersed and no agglomeration is observed after repeated thermal cycling involving melting and solidification in the DSC. A special network substructure is observed in the eutectic. The substructure seems to interconnect the SiO_2 nanoparticles, thus forming an interconnected network (“percolation network”) [37].

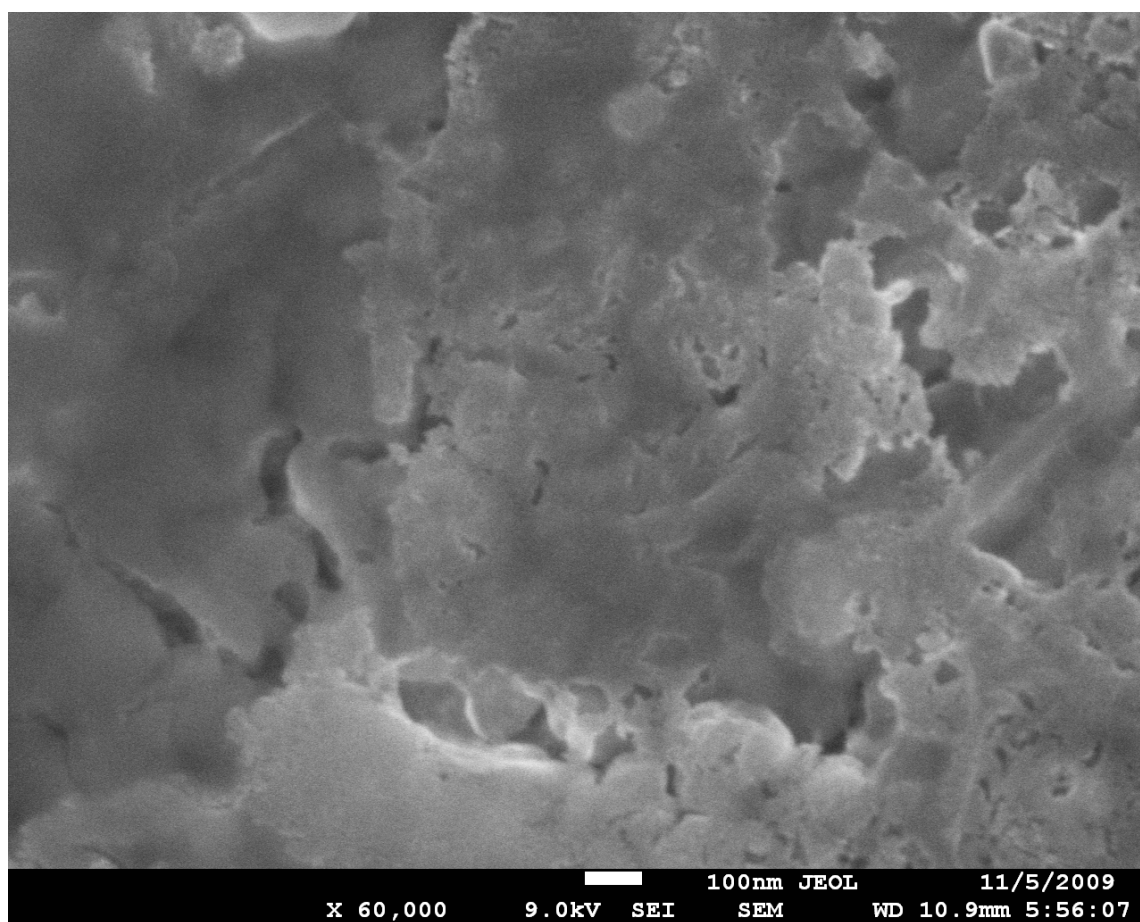


Figure 16. SEM image of the pure eutectic salt of $\text{BaCl}_2\text{-NaCl-CaCl}_2\text{-LiCl}$ after repeated thermal cycling involving melting and solidification in the DSC. A special substructure, which was shown in the nanomaterial (Figure 15), was not observed in the pure material [37].

5.2.1 Specific heat capacity results

Two samples of pure eutectic salt and three samples of silica nanomaterials were tested individually (with repeated thermal cycling involving melting and solidification for each sample) and their specific heat capacity results are shown in Figures 17-18 and in Tables 9-10. Figure 17 compares the specific heat capacity variation with temperature for pure eutectic salts and nanomaterials in the solid phase (“nanocomposites”). The peak at ~ 500 °C is the melting peak of the base eutectic (488 °C). Table 9 shows the average specific heat capacity of nanocomposites between 355 °C and 455 °C, respectively. The average specific heat capacity of nanocomposites was enhanced by 11 % ~ 14 % compared to the specific heat capacity of the eutectic. (The measurement uncertainty is 1.9 % ~ 2.0 %). Figure 18 shows the variation of specific heat capacity with temperature for pure eutectic salts and the nanomaterials in the liquid phase (“nanofluids”). The average specific heat capacity of nanofluids between 525 °C and 555 °C are shown in Table 10. The average specific heat capacity of nanofluids was enhanced by 19 ~ 24 %. (Measurement uncertainty is 2.2 % ~ 2.4 %) [36].

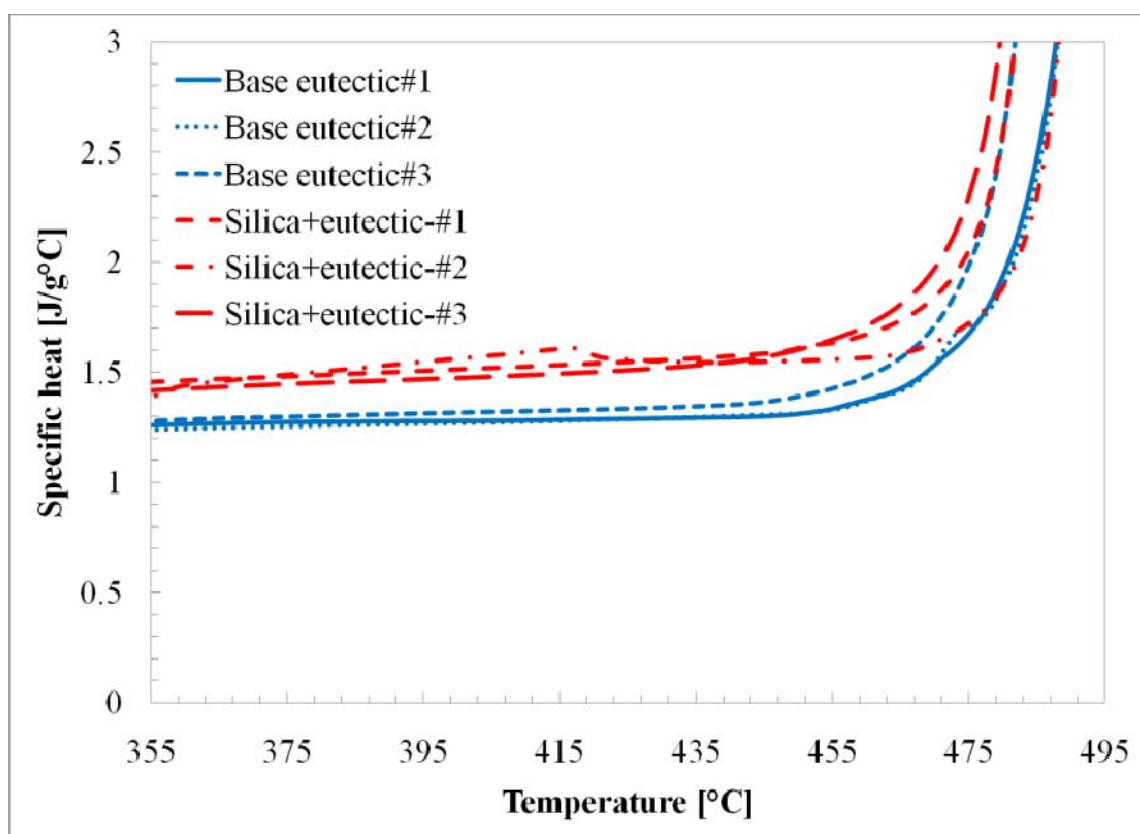


Figure 17. Variation of specific heat capacity with temperature (355 °C ~ 495 °C) for pure eutectic salt of $\text{Li}_2\text{CO}_3\text{-K}_2\text{CO}_3$ and the corresponding SiO_2 nanocomposites. The average specific heat capacity of nanocomposite was enhanced by 11 ~ 14 % over that of the pure molten salt eutectic [36].

Table 9. Specific heat capacity measurements (J /g-K) of pure eutectic salt of Li_2CO_3 - K_2CO_3 and the corresponding SiO_2 nanocomposite samples. Average specific heat capacity measurements (J /g-K) of the pure eutectic and the nanocomposite in the temperature range of 495 ~ 555 °C are listed here. The average specific heat capacity of the nanocomposite samples were enhanced by 11 % ~ 14 % compared with that of the pure eutectic. (ϵ : standard deviation for all the thermo-cycle data for a sample) [36].

C_p (J/g-K)	Pure eutectic #1	Pure eutectic #2	Nano- composite #1	Nano- composite #2	Nano- composite #3
1 st run	1.37	1.38	1.52	1.42	1.50
2 nd run	1.28	1.37	1.52	1.48	1.54
3 rd run	1.23	1.30	1.53	1.50	1.50
4 th run	1.23	1.25	1.53	1.58	1.42
5 th run	-	-	1.53	1.61	-
6 th run	-	-	1.53	1.56	-
7 th run	-	-	1.52	1.57	-
8 th run	-	-	1.51	1.55	-
9 th run	-	-	1.51	1.53	-
Average	1.28	1.33	1.52	1.53	1.49
Enhancement	-	-	13 %	14 %	11 %
ϵ	0.07	0.06	0.01	0.05	0.05

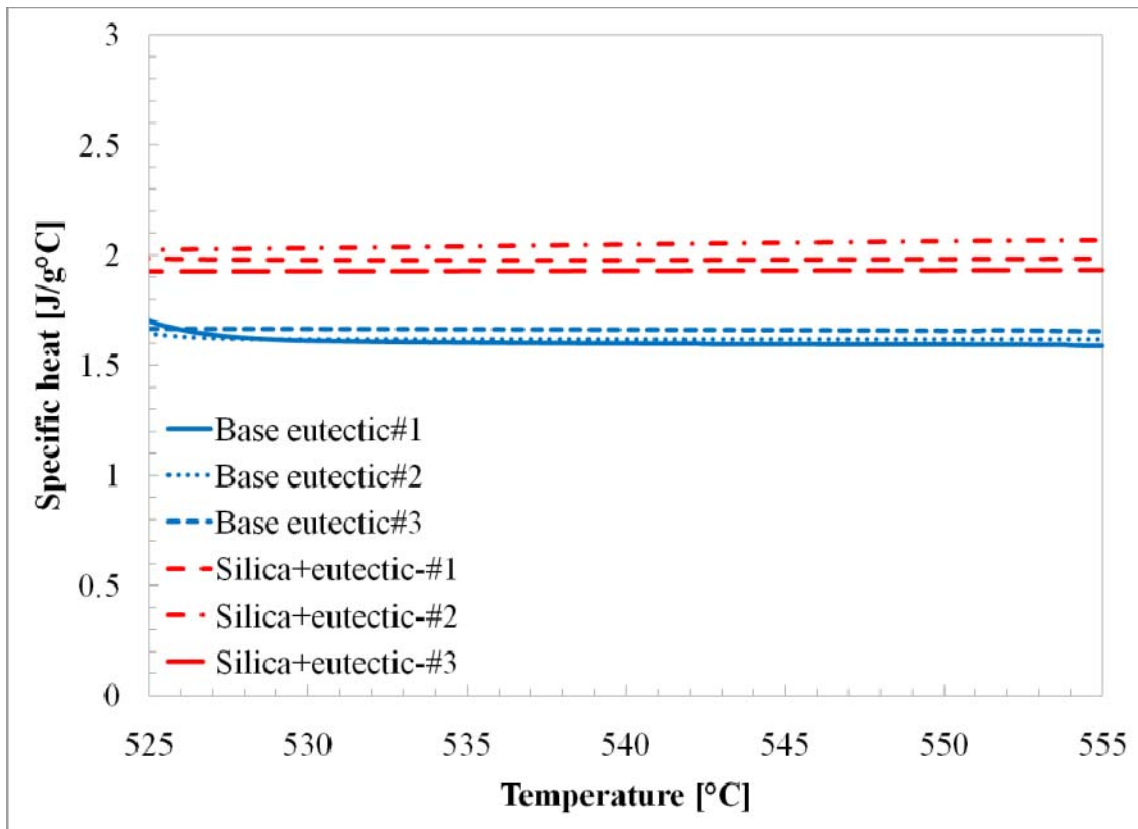


Figure 18. Variation of the specific heat capacity with temperature (525 °C ~ 555 °C) for pure eutectic salt samples of $\text{Li}_2\text{CO}_3\text{-K}_2\text{CO}_3$ and the corresponding SiO_2 nanofluids samples. The average specific heat capacity of the nanofluid samples was enhanced by 19 ~ 24 % over that of the pure molten salt eutectic [36].

Table 10. Specific heat capacity measurements (J /g-K) of pure eutectic salt samples of $\text{Li}_2\text{CO}_3\text{-K}_2\text{CO}_3$ and the corresponding SiO_2 nanofluid samples. Average specific heat capacity measurements (J /g-K) of the pure eutectic and the nanofluid for a temperature range of 495 ~ 555 °C are listed here. The average specific heat capacity of the nanofluid samples were enhanced by 13 % ~ 16 % compared with that of the pure eutectic [36]. (ϵ : standard deviation for all the thermo-cycle data for a sample).

C_p (J/g-K)	Pure eutectic #1	Pure eutectic #2	Nanofluid #1	Nanofluid #2	Nanofluid #3
1 st run	1.73	1.73	1.95	1.85	1.93
2 nd run	1.63	1.72	1.97	1.89	2.00
3 rd run	1.56	1.62	1.98	2.00	1.94
4 th run	1.56	1.55	2.00	1.99	1.84
5 th run	-	-	2.01	2.10	-
6 th run	-	-	2.00	2.15	-
7 th run	-	-	1.98	2.10	-
8 th run	-	-	1.97	2.10	-
9 th run	-	-	1.97	2.10	-
Average	1.62	1.65	1.98	2.03	1.93
Enhancement	-	-	21 %	24 %	19 %
ϵ	0.08	0.09	0.02	0.10	0.07

5.2.2 SEM / TEM analysis

SEM analyses were performed to observe the microstructure of the nanomaterials. Figure 19 shows the SEM image of pure eutectic salt. Figure 20 and 21 shows the microstructure of nanomaterials (which showed 19~24% enhancement in the specific heat capacity). It was observed in Figure 20 that a special sub-structure was formed in the nanomaterial (i.e., “percolation networks” - similar to that observed in the chloride eutectic nanomaterials). It was observed that the special sub-structures form interconnections within individual nanoparticles and form an interconnected network. These modified structures were only observed within the nanomaterial samples that demonstrated enhanced thermo-physical properties. Figure 21 is a high resolution SEM image that was used to observe the distribution of the individual nanoparticles within the nanomaterial sample.

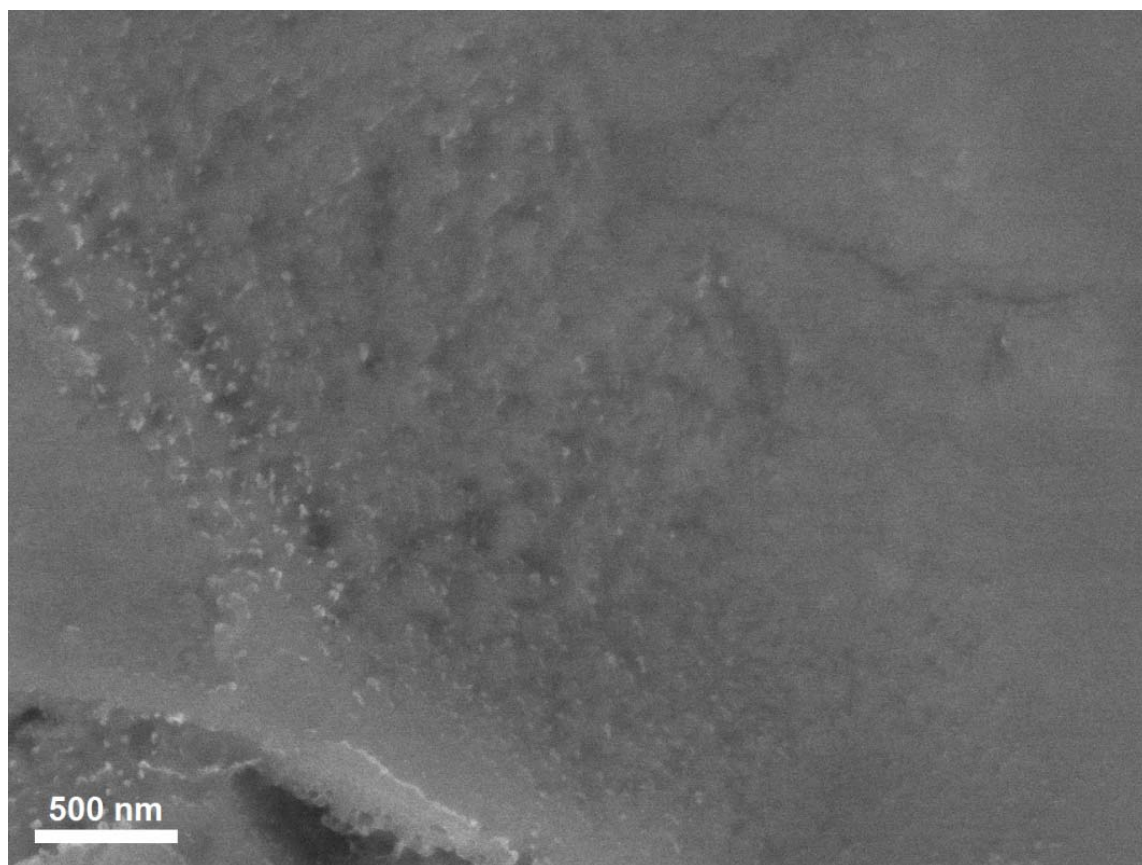


Figure 19. SEM image of pure molten salt sample [36].

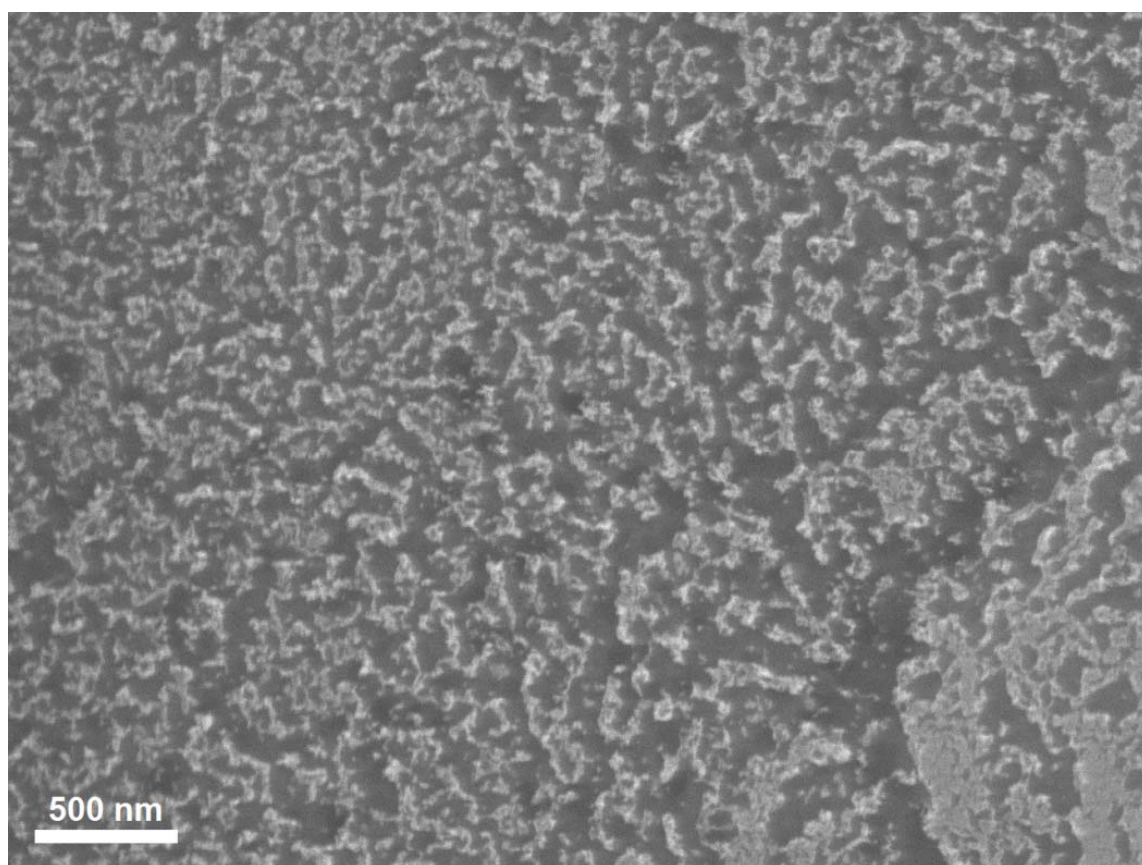


Figure 20. SEM images of SiO₂/Li₂CO₃-K₂CO₃ nanomaterial, which showed the enhanced specific heat capacity at solid phase and at liquid phase. It was observed that the molten salt eutectic formed a very special structure resembling weave pattern (“percolation network”). This structure is expected to play an important role for the enhancement of the specific heat capacity of nanomaterial [36].

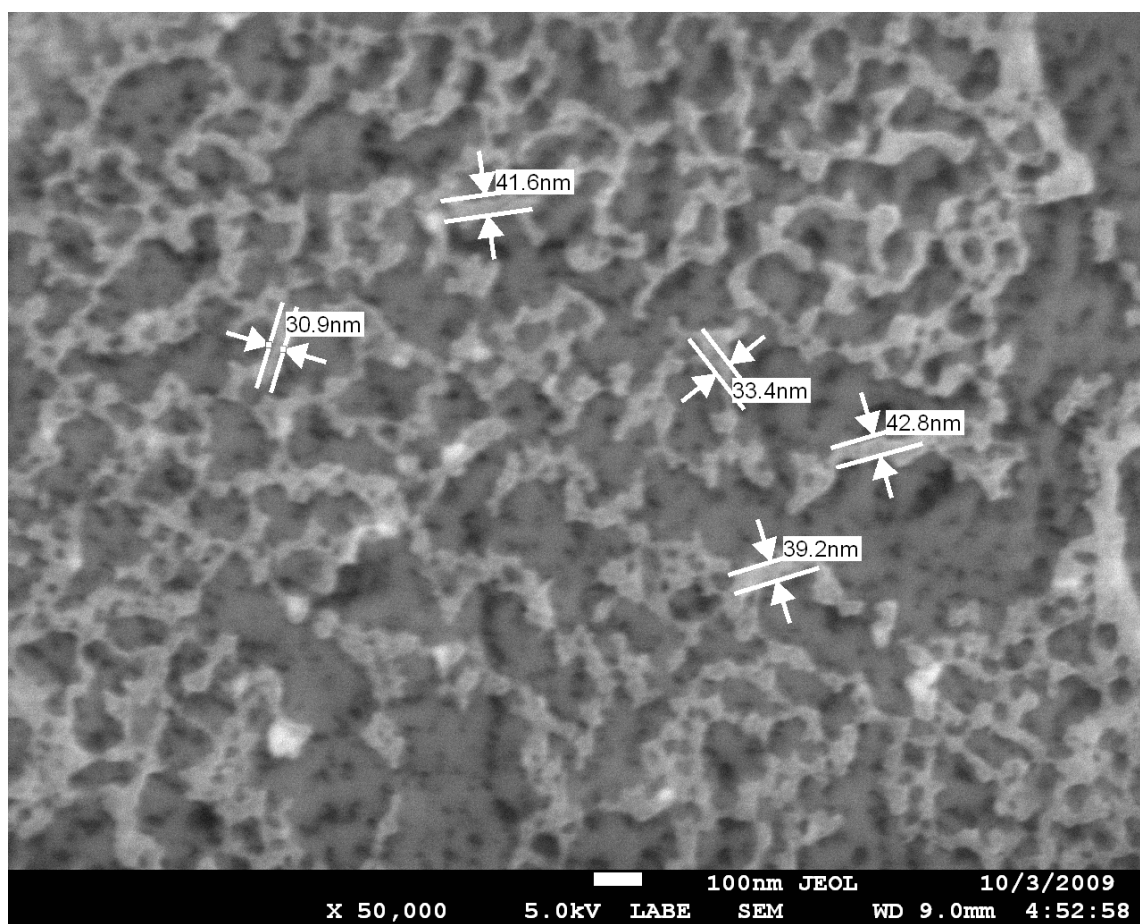


Figure 21. Scanning Electron Microscopy (SEM) image of silica nanoparticles in the $\text{SiO}_2/\text{Li}_2\text{CO}_3\text{-K}_2\text{CO}_3$ nanomaterial after thermal cycling in the DSC for multiple times. The image shows that the nanoparticles were not agglomerated and the nominal size of the nanoparticle is 2~20 nm. The sub-structures of lighter color seem to engulf the nanoparticles and form an interconnected network (“percolation network”) [36].

5.3 Discussions: Specific Heat Capacity of Nanomaterial

5.3.1 Conventional specific heat capacity model

Conventional thermal equilibrium model (macroscopic model, also known as “simple mixing model”) was used to predict the enhancement of the specific heat capacity of nanomaterials. The expression for the model 1 (Equation 14) is:

$$C_{p,t} = \frac{\rho_{np}V_{np}C_{p,np} + \rho_bV_bC_{p,b}}{\rho_{np}V_{np} + \rho_bV_b} \quad (14)$$

where C_p is specific heat capacity, ρ is density, and V is volume fraction. Subscript t , np , and b denote nanomaterials, nanoparticle, and base material. According to the simple mixing model (Equation 14), the specific heat capacity of nanomaterials should be slightly lower than that of the base material, since the specific heat capacity of nanoparticles are lower than that of base material and the concentration is extremely low (1 % by mass). For a nanomaterial, whose molten salt composition is 62:38, the average specific heat capacity of the base material is 1.23 J/g°C for solid phase and 1.63 J/g°C for liquid phase. The specific heat capacity of silica nanoparticles is 0.70 J/g°C [51]. Therefore, the prediction by the model (Equation 14) is ~ 1.23 J/g°C for nanocomposite and ~ 1.63 J/g°C for nanofluid. However, the specific heat capacity of the nanomaterials in our experiments was enhanced by ~ 10 -21 % compared to the base material. This

implies that the specific heat capacity of the nanomaterials cannot be explained by the macroscopic heat transfer theory and therefore a modification to the simple mixing model (Equation 14) should be investigated. The discrepancy between the prediction by the simple mixing model and the experimental data is shown in Table 11.

Table 11. Discrepancy between the experimental data and the prediction by the simple mixing model (Equation 14). (*: measurement uncertainty)

Phase	Experiment (*)	Prediction (Equation 14)	Discrepancy (%)
Solid phase	1.37 (0.1%)	1.23	10 %
Liquid phase	1.98 (1.4%)	1.63	21 %

5.3.2 New specific heat capacity model

This section provides a speculative exercise in predicting the specific heat capacity of the nanomaterials investigated in this study. Several transport mechanisms were proposed in the literature to enumerate the anomalous enhancements in the thermo-physical properties of nanomaterials that were measured experimentally, which include: Brownian movement of nanoparticles, nano-convection due to Brownian motion of nanoparticles, ordering of liquid molecules on surface of nanoparticles, clustering of nanoparticles (percolation network), and interfacial thermal resistance between nanoparticles and surrounding base materials [18-21,29,30].

The enhanced specific heat capacity of nanomaterial in the experiments can be caused by one of aforementioned material energy storage regimes or due to a combination thereof and/or alternate mechanisms not listed here. However, based on the electron microscopy analyses of the samples a simple approach has been formulated in this study to enumerate the energy storage modes that are responsible for the measured enhancements in the specific heat capacity of these high temperature nanomaterials. The SEM and TEM analyses in the previous sections (Sections 5.1 and 5.2) showed the formation of the micron-scale substructures within the bulk phase of the eutectic salt in each nanomaterial. These special structures were observed to engulf the nanoparticles and form an interconnected network (percolation network). Figure 15 and Figure 21 show that these sub-structures connect with other sub-structures and eventually form an interconnected network. The absence of these percolation networks in any nanomaterial sample was also accompanied by the absence of substantial enhancements in the specific heat capacity (over that of the pure eutectic salt samples). Hence the formation of this percolation network is expected to contribute to the enhanced specific heat capacity of nanomaterials.

To elaborate further, it is well known that liquid molecules rearrange on a crystalline surface to form a compressed layer which can span dimensions that are several nano-meters thick [52-55]. The ordering of the liquid molecules and formation of a higher-density semi-solid layer on the nanoparticles can potentially trigger the nucleation as well as growth of a modified structure by inducing phase changes within the molten salt materials on a larger scale (on a scale spanning several hundreds of

microns). The micron-scale sub-structures thus appear to emanate from the surface of the individual nanoparticles in the electron microscopy images. This can, as a result, induce localized change in the chemical composition of the molten salts. These local micro-scale sub-structure regions may have different composition (e.g., higher Li_2CO_3 or higher K_2CO_3) when compared to the composition in the bulk eutectic or for the pure salt eutectic samples. This can lead to separation of molten salts materials with different composition and different thermo-physical properties (e.g., melting points, specific heat capacity and thermal conductivity) in the different phases formed in the bulk of the solvent region (surrounding the nanoparticles). Subsequently, this modified structure within the molten salt materials can form interconnected network (e.g., similar to frost formation on cold surfaces exposed to humid air where nucleating frost particles form interconnected networks). This interconnected network formed due to modification of the chemical composition within the bulk eutectic phase is apparent as micron-scale substructures in the electron microscopy images. This phenomenon seems to be especially sensitive to the enhanced surface area provided by the nanoparticles for inducing the apparent nucleation and phase change within the bulk of the eutectic. Agglomeration of nanoparticles leads to drastic reduction in the available surface area for formation of the compressed layer and also for inducing the nucleation of the phase change process in the eutectic salt. Also, these modified structures (interconnected network) are expected to have enhanced thermo-physical properties than the bulk eutectic salt (due to differences in composition) and consequently lead to the high enhancement of the specific heat capacity of the nanomaterials. Additional energy

storage modes can also exist at the interface between individual nanoparticles and the salt (solvent phase), as well as at the interface between the modified structures (percolation network) and the surrounding molten salt material of different chemical composition.

Assuming that the modified structure (micron-scale structure) has higher thermal properties than the eutectic, the conventional simple mixing model can be modified as model 2 (Equation 15) and is expressed as follows: [56,57]

$$C_{p,t} = \frac{\rho_{np}V_{np}C_{p,np} + \rho_cV_cC_{p,c} + \rho_bV_bC_{p,b}}{\rho_{np}V_{np} + \rho_cV_c + \rho_bV_b} \quad (15)$$

where C_p , ρ , and V are specific heat capacity, density, and volume fraction, respectively. Subscript t , np , c , and b denote nanomaterial (total), nanoparticle, modified structure, and base material, respectively. The specific heat capacity of modified structure is not available in the literature. However, we can estimate the value based on the modified heat capacity model above (Equation 15). Properties of nanoparticles and bulk molten salts are available in the literature, yet those of interconnected network are unknown. In this study, the density of modified structure was assumed to be ~ 2.2 g/cc (solid phase density of bulk molten salt). The volume fraction of modified structure was estimated by image analysis. A backscattered electron image distinguishes different material by contrast. Converting the image into a binary image and counting the number of black pixels and white pixels can give a rough estimate of area fraction of the modified

structure in the image. Assuming the area fraction obtained from the SEM images is representative of the volume fraction of the modified structure, image analysis can be used to estimate the value of the volume fraction of the modified structure (micron-scale substructures forming the percolation network).

Figure 22 shows the backscattered electron microscopy image of $\text{SiO}_2/\text{Li}_2\text{CO}_3\text{-K}_2\text{CO}_3$ nanocomposite, including: (a) its binary image; and (b) histogram of the binary image. From the image analysis, the volume fraction of modified structure was estimated to be $\sim 33\%$. Substituting these values and the experimental specific heat capacity into the model (Equation 15), we can roughly estimate the specific heat capacity of modified structure and the value is $\sim 2.7\text{ J/g-K}$. Figure 23 shows the calculated value of the effective specific heat capacity of nanomaterial with parametric change in the specific heat capacity of modified structure. Figure 23 shows that the model (Equation 15) matches the experimental value for the effective specific heat capacity of the nanomaterial when the modified structure has a specific heat capacity of 2.7 J/g-K . This implies that the modified structure has Li salt content exceeding 70% by molar ratio (further discussions are provided in Section 5.4).

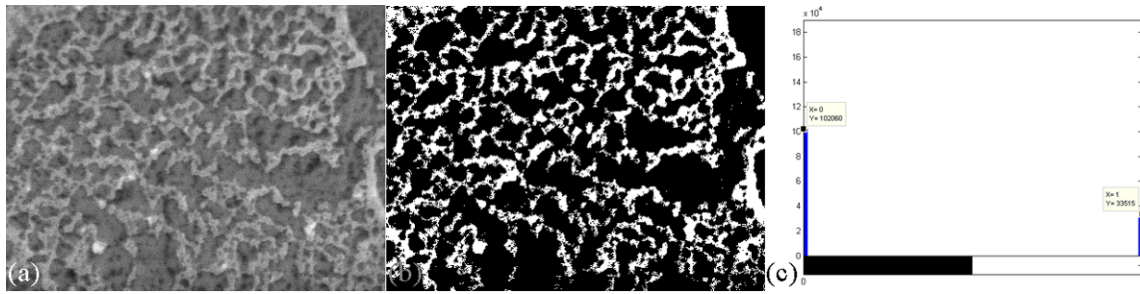


Figure 22. (a) Backscattered electron microscopy image of $\text{SiO}_2/\text{Li}_2\text{CO}_3\text{-K}_2\text{CO}_3$. (b) A binary image obtained from (a). (c) A histogram of pixel distribution derived from (b). The threshold intensity is 128.

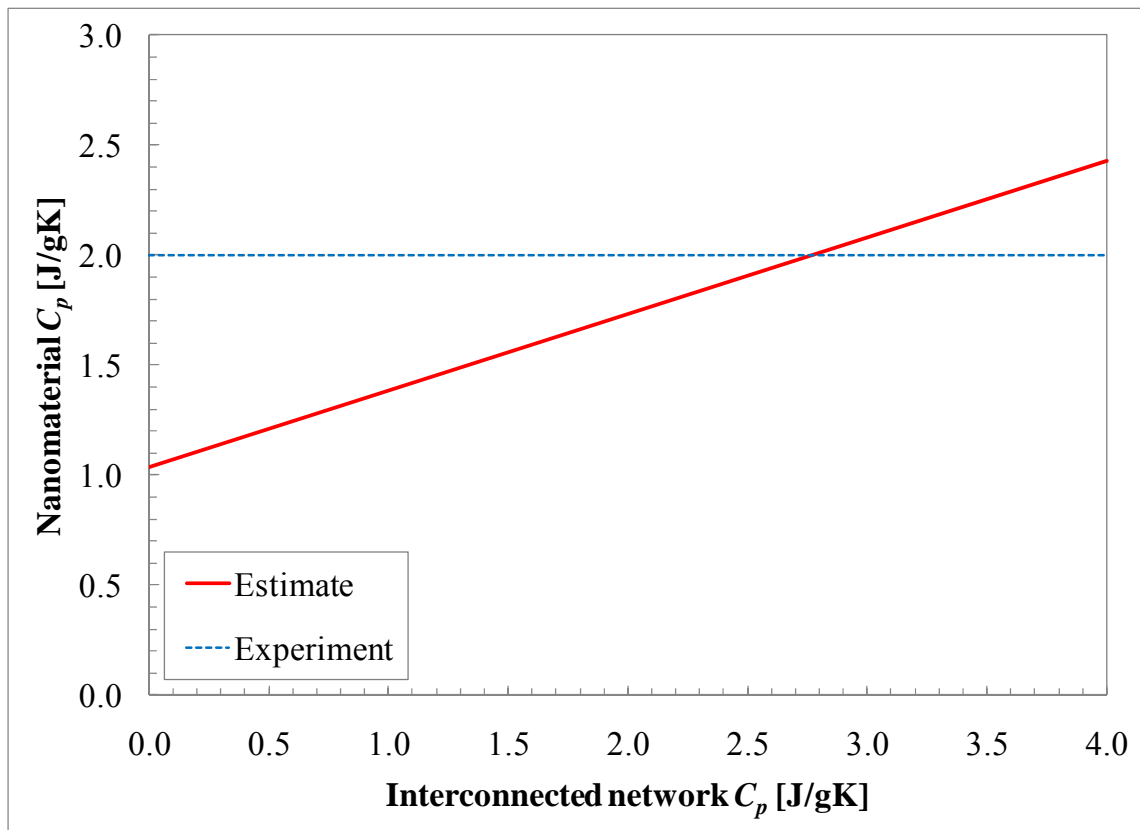


Figure 23. Plot of calculated value of effective specific heat capacity of nanomaterials for parametric variation in the specific heat capacity of the modified structure using Equation (16). Blue dotted line represents experimentally measured value of the specific heat capacity of nanomaterial and the red line represents the estimated (calculated value) of the effective specific heat capacity of nanomaterial, based on Equation (15).

5.3.3 Specific heat capacity according to classical thermodynamics

Theoretical maximum specific heat capacity of a solid in thermodynamics is $3ZR$. Z is the number of atoms in a molecule and R is the molar gas constant (8.314472 J/mol-K). Accordingly, the theoretical maximum specific heat capacity of molten salt ($\text{Li}_2\text{CO}_3\text{-K}_2\text{CO}_3$, whose molten salt composition is 62:38 by molar ratio) is 149.7 J/mol-K . Figure 24 shows the molar heat capacity of molten salt nanomaterials ($\text{SiO}_2/\text{Li}_2\text{CO}_3\text{-K}_2\text{CO}_3$). The maximum heat capacity from the experiments is 152 J/mol-K . In our experiments, the temperature range of interest is very high ($355\sim 455^\circ\text{C}$); therefore, lattice vibrations are accompanied by internal vibrations within the covalent molecules. Hence, the maximum specific heat capacity is expected to be marginally higher than the classical value of $3ZR$.

The experimentally measured values of the specific heat capacity of the pure molten salt eutectic therefore do not violate the classical laws of thermodynamics. However, the specific heat capacity of modified structure calculated in the previous section (5.3.2) is $\sim 2.7 \text{ J/g-K}$, which corresponds to a molar specific heat capacity of $\sim 265 \text{ J/mol-K}$. This value is much higher than the theoretical limit of specific heat capacity of the solid phase of the molten salt eutectic. The results indicate that the chemical composition of the modified structure consists of $\sim 70\% \text{ Li}_2\text{CO}_3$ (cf. Figure 25 and Figure 26). The observed enhancement in the specific heat capacity may therefore result from another mechanism or a combination of the proposed model and alternate

energy storage mechanisms which are currently unknown (which can be the topic of future studies).

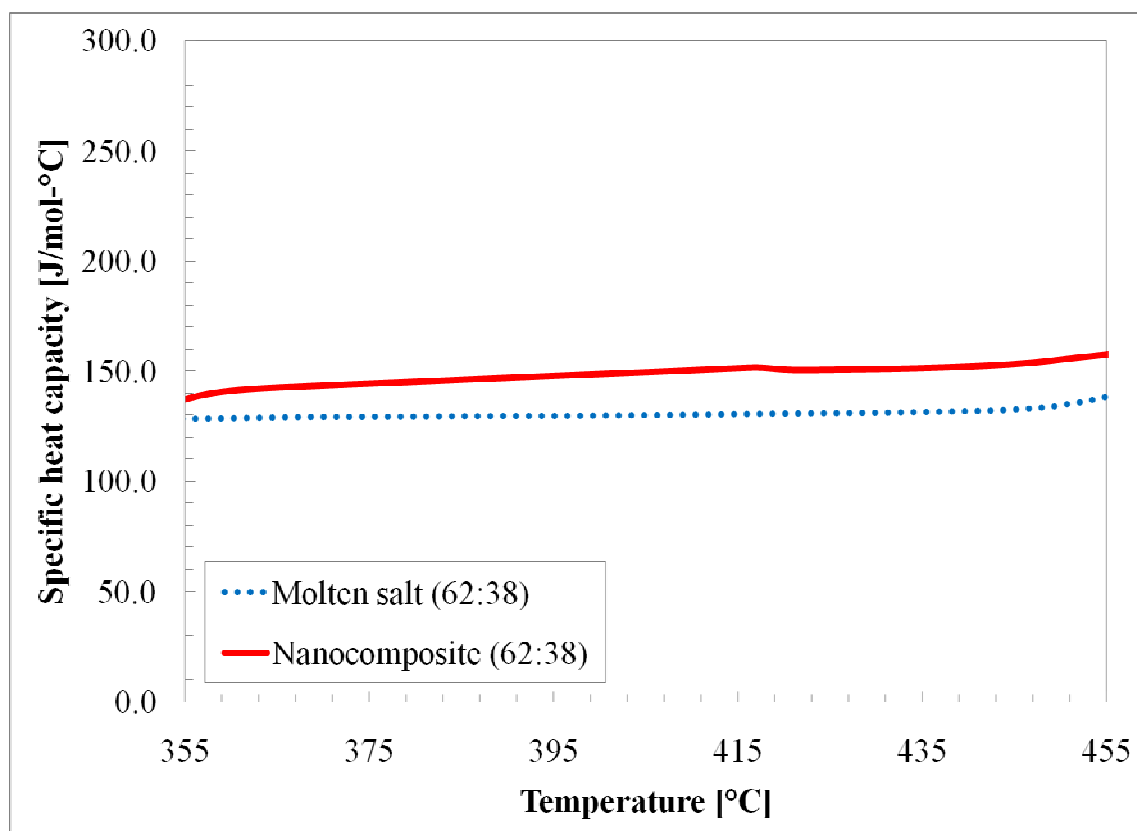


Figure 24. Plot of molar specific heat capacity as a function of temperature for pure molten salt eutectic and the corresponding silica nanomaterial (nanofluid). The plotted results were obtained from experimental measurements.

5.4 SiO₂ / Li₂CO₃-K₂CO₃ Nanomaterial with Different Composition

To explore the role of the compressed phase and the modified structure on the total specific heat capacity of the molten salt nanomaterials, the variation of the effective specific heat capacity was measured for the pure molten salt due to change in the composition of the salt mixture. A mixture of Li₂CO₃ and K₂CO₃ has three different values of the specific heat capacity, based on the molten salt composition (Figure 25).

In Figure 25, for region A (Li salt content < 62% by molar ratio), the specific heat capacity of the molten salt is ~ 1.6 J/gK and is almost invariant with temperature. The measured values in this study is consistent with the literature data for this composition of the molten salt (to within 5%).

In Figure 25, for region B (Li salt content is ~ 66% by molar ratio), the specific heat capacity of the molten salt dramatically decreases with temperature. The measured values for the specific heat capacity as a function of temperature demonstrate very high variability in the measurements which makes it difficult to obtain a single value of specific heat capacity with sufficient precision.

In Figure 25, for region C (Li salt content > 70% by molar ratio), the molten salt has the highest value for the average specific heat capacity (~2.8 J/g-K) and the average value increases marginally with temperature. The measurements performed in this study are also consistent and there was only marginal variation between measurements (less than 3%).

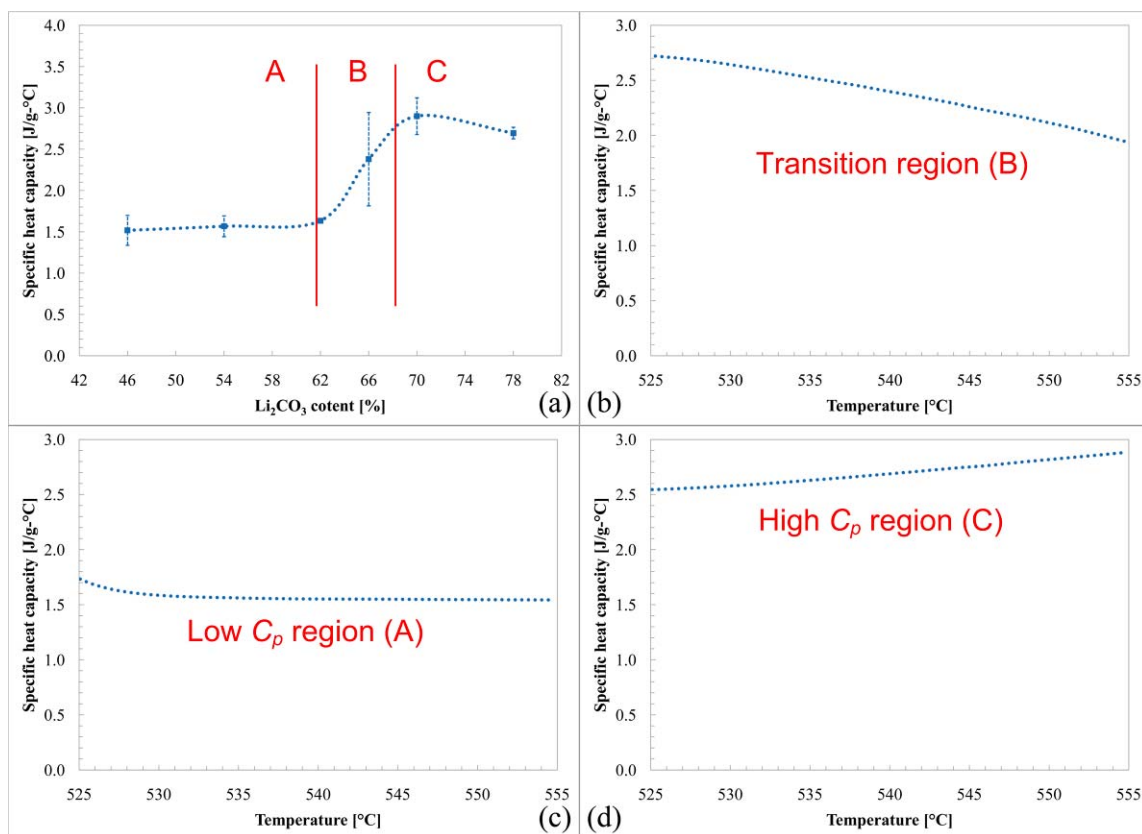


Figure 25. (a) The specific heat capacity of Li_2CO_3 - K_2CO_3 salt mixture can be classified into three distinct regions: low C_p region (A), transition region (B), and high C_p region (C). (b) Plot for variation of specific heat capacity with temperature in the transition region shows dramatic decrease in specific heat capacity with temperature and the variability of the measurements is also large (as represented by the error bars in Figure 25a). (c) Plot for the variation of specific heat capacity with temperature for the low C_p region (~ 1.6 J/g·K) and is observed to be almost invariant with temperature. (d) Plot for the specific heat capacity with temperature in the high C_p region (~ 2.8 J/gK) and is observed to increase significantly with temperature.

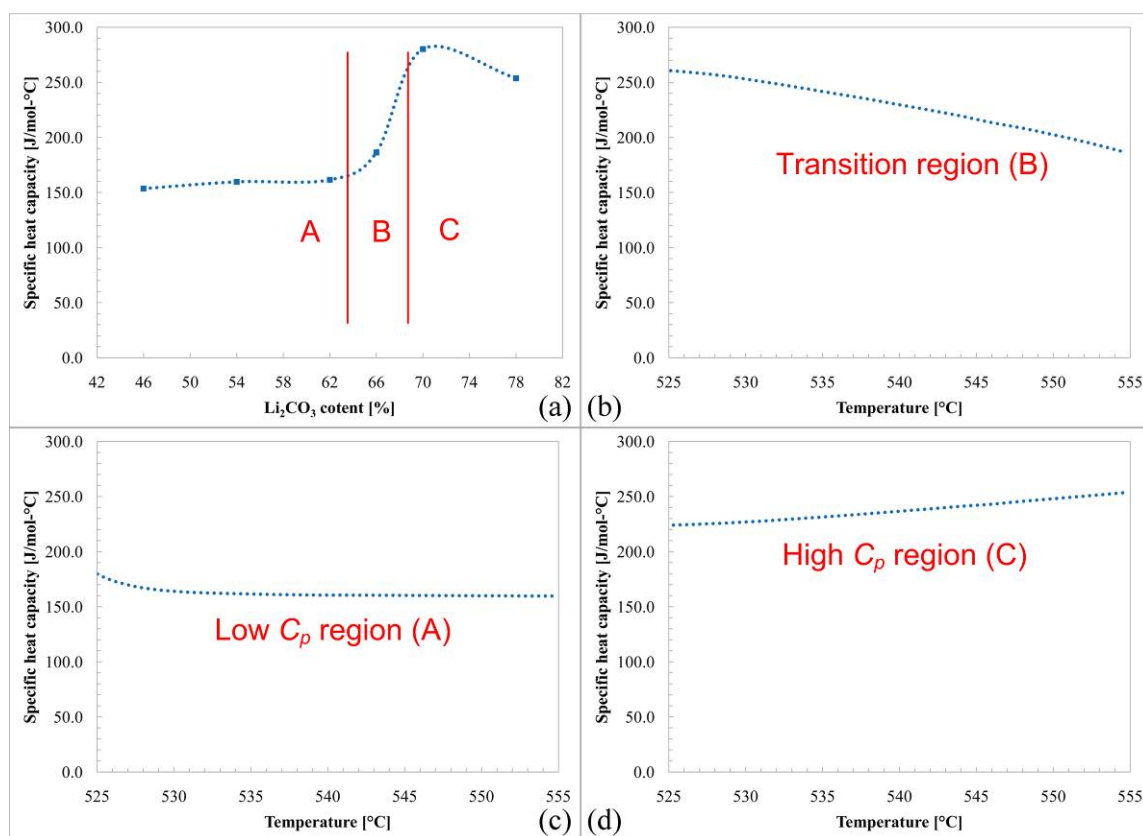


Figure 26. Molar specific heat capacity values derived from Figure 25.

In the previous section (Section 5.3), the specific heat capacity enhancement (19~24 %) of molten salt nanomaterials was reported to be ~19-24%, for a molten salt composition of 62:38 (Li_2CO_3 : K_2CO_3 by molar ratio). In addition to the previous experiments, five different molten salt compositions (46:54, 54:46, 66:34, 70:30, and 78:22) were chosen for testing. To verify repeatability of the measurements, three samples of pure molten salts and three samples of nanomaterials were synthesized separately for each of these compositions. These results are presented next.

5.4.1 Specific heat capacity results for molten salts with different compositions

Tables 12 and 13 list the values of the specific heat capacity measurements for pure molten salts with different compositions as well as for the corresponding nanomaterials synthesized with nanoparticles at 1% mass fraction. Figure 27 shows the variation of specific heat capacity with temperature for molten salt samples with a composition of 46:54 (Li_2CO_3 : K_2CO_3 by molar ratio) and the corresponding nanomaterial with SiO_2 mass concentration of 1%. It was observed that the specific heat capacity of the nanomaterial samples for this composition was slightly lower than that of the pure molten salt samples. At this composition the experimental data is consistent with the conventional heat capacity model (Equation 14) since the specific heat capacity of the silica nanoparticle is slightly lower than that of the molten salts and the concentration of nanoparticles is extremely small (~1 % by weight).

Figure 28 shows specific heat capacity of the molten salt and nanomaterial samples, where the molten salt composition was 54:46 ($\text{Li}_2\text{CO}_3\text{:K}_2\text{CO}_3$ by molar ratio). It was observed that the specific heat capacity of the nanomaterials was slightly lower than that of the pure molten salt. This is also in good agreement with the conventional heat capacity model (mixing rule, Equation 14).

The specific heat capacity of molten salt samples and nanomaterial samples were measured, where the molten salt composition was 62:38 ($\text{Li}_2\text{CO}_3\text{:K}_2\text{CO}_3$ by molar ratio). The results from these measurements were already discussed in the previous section where the specific heat capacity was observed to be enhanced by 26 % (Figure 29) [36].

Figure 30 shows the specific heat capacity of molten salt and nanomaterial samples, where the molten salt composition was 66:34 ($\text{Li}_2\text{CO}_3\text{:K}_2\text{CO}_3$ by molar ratio). The measurement results show that the specific heat capacity of the pure molten salts changed dramatically for each measurement and it was very difficult to measure their specific heat capacity with sufficient precision. The variation of the experiment results was ~ 100 %. Accordingly, the specific heat capacity measurement for nanomaterials was also unstable for this composition of the molten salt.

Figure 31 shows the specific heat capacity of molten salt and nanomaterial samples, where the molten salt composition was 70:30 ($\text{Li}_2\text{CO}_3\text{:K}_2\text{CO}_3$ by molar ratio). The specific heat capacity of the pure molten salt was measured to be substantially high (2.8 J/g-K). The specific heat capacity was also observed to increase monotonically with temperature. The specific heat capacity of nanomaterials was enhanced by ~ 12 % for both the solid phase and liquid phase of the samples. The measurement uncertainty

was estimated to be less than 3 %. The conventional heat capacity model (Equation 14) failed to predict the measured enhancements in the value of specific heat capacity of the nanomaterials.

Figure 32 shows specific heat capacity of molten salt and nanomaterial, whose molten salt composition is (78:22, $\text{Li}_2\text{CO}_3\text{:K}_2\text{CO}_3$ by molar ratio). It was observed that the specific heat capacity of the nanomaterials was slightly lower than that of the pure molten salt. This also makes a very good agreement with conventional heat capacity model.

Figure 33 shows a graph summarizing the effect of salt composition on the specific heat capacity measurements for the pure salt samples and the nanomaterials. In these experiments, specific heat capacity values of the nanomaterials were enhanced only at specific values of the molten salt compositions (62:38 and 70:30 by molar ratio). These salt compositions are in the vicinity of the transition region (66:34 by molar ratio). At these salt compositions the enhancement in the specific heat capacity values for the samples measured in this study exceeded the predictions from the simple mixing rule (Equation 14). In contrast, the nanomaterials with molten salt compositions (46:54, 54:46, and 78:22 by molar ratio) significantly different from that of the transition region (66:34 by molar ratio) did not show any significant enhancement in the values of the specific heat capacity but were in good agreement with the conventional specific heat capacity model (Equation 14).

Table 12. Average specific heat capacity of molten salts in the solid phase and for the corresponding nanocomposites. (ϵ : measurement uncertainty; * from literature [36]; ** at the transition region, where the specific heat capacity of molten salt is unstable and changes dramatically for each measurement)

Molar ratio ($\text{Li}_2\text{CO}_3:\text{K}_2\text{CO}_3$)	Molten salt (ϵ)	Nanocomposite (ϵ)	Enhancement (%)
46:54	1.15 (3.4%)	1.08 (3.4%)	-6 %
54:46	1.22 (2.7%)	1.22 (2.4%)	0 %
62:38	1.24* (0.1%)	1.37* (0.1%)	10 %*
66:34	**	**	**
70:30	1.37 (2.9%)	1.54 (1.8%)	12 %
78:22	1.38 (1.5%)	1.43 (1.0%)	3 %

Table 13. Average specific heat capacity of molten salts in the liquid phase and the corresponding nanofluids. (ϵ : measurement uncertainty; * from literature [36]); ** at the transition ratio, the specific heat capacity of molten salt is unstable and changes dramatically with each measurement)

Molar ratio ($\text{Li}_2\text{CO}_3:\text{K}_2\text{CO}_3$)	Molten salt (ϵ)	Nanofluid (ϵ)	Enhancement (%)
46:54	1.52 (5.2%)	1.44 (5.1%)	-6 %
54:46	1.57 (3.6%)	1.53 (4.9%)	-2 %
62:38	1.64* (0.6%)	1.98* (1.4%)	21 %*
66:34	**	**	**
70:30	2.90 (6.4%)	3.26 (2.8%)	12 %
78:22	2.70 (2.5%)	2.72 (1.3%)	1 %

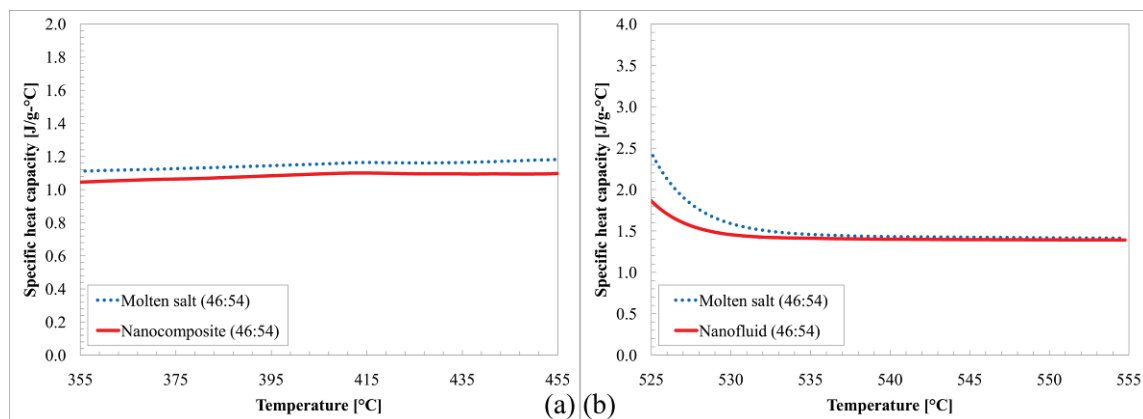


Figure 27. Variation of specific heat capacity with temperature for (a) solid phase, and (b) liquid phase. The samples tested included pure salt mixture ($\text{Li}_2\text{CO}_3 : \text{K}_2\text{CO}_3$ for 46:54 molar ratio) and the nanomaterial at 1% mass fraction of SiO_2 .

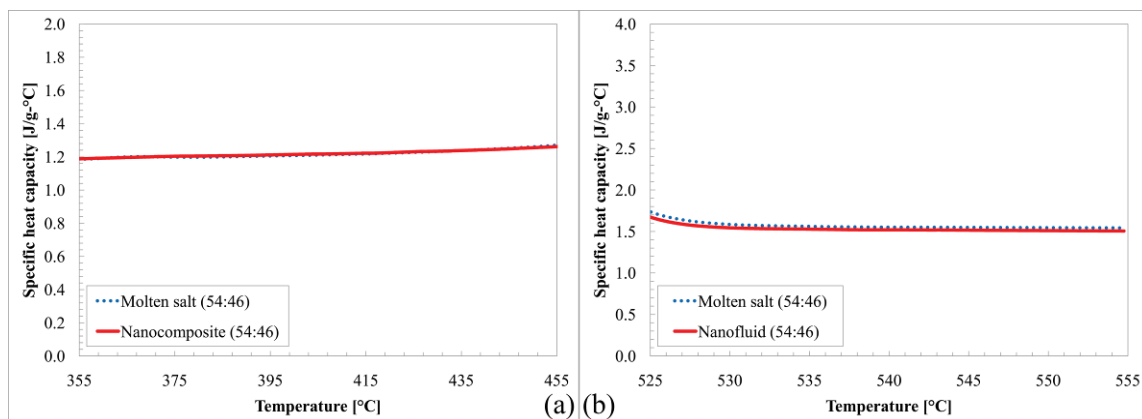


Figure 28. Variation of specific heat capacity with temperature for (a) solid phase, and (b) liquid phase. The samples tested included pure salt mixture (Li_2CO_3 : K_2CO_3 for 54:46 molar ratio) and the nanomaterial at 1% mass fraction of SiO_2 .

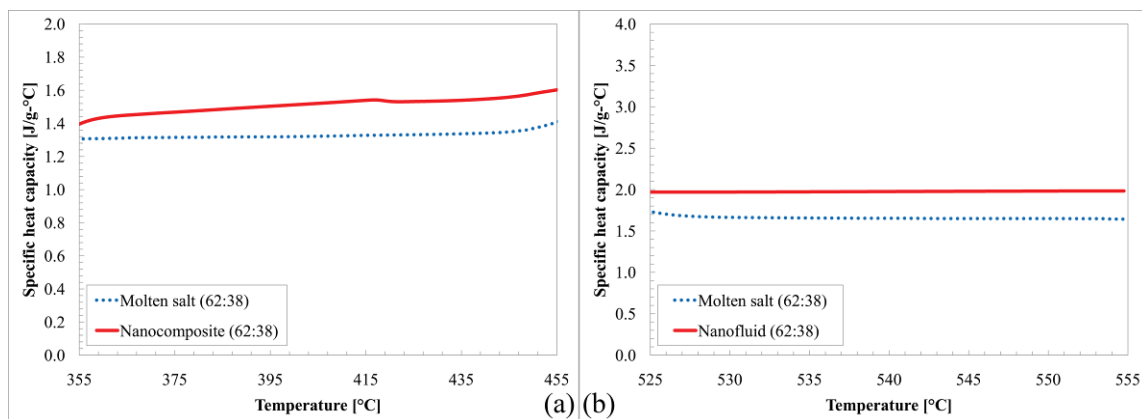


Figure 29. Variation of specific heat capacity with temperature for (a) solid phase, and (b) liquid phase. The samples tested included pure salt mixture (Li_2CO_3 : K_2CO_3 for 62:38 molar ratio) and the nanomaterial at 1% mass fraction of SiO_2 [36].

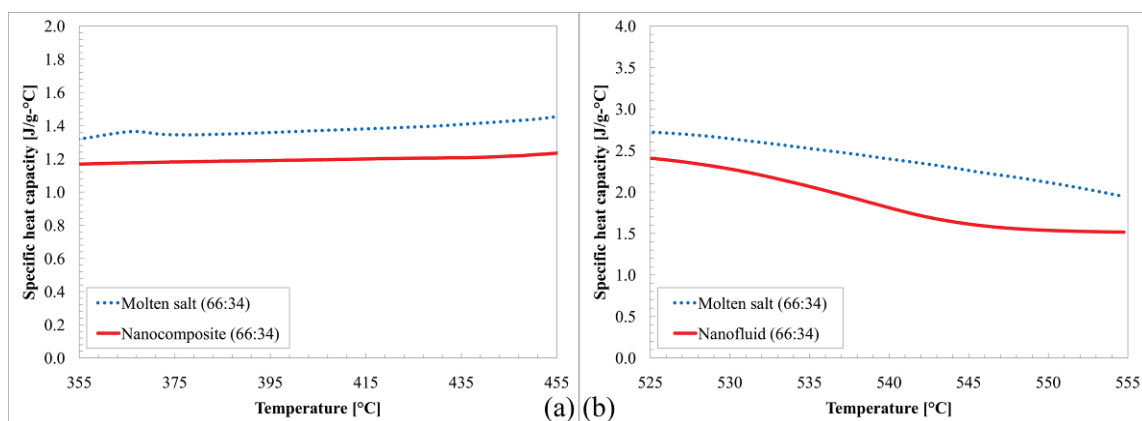


Figure 30. Variation of specific heat capacity with temperature for (a) solid phase, and (b) liquid phase. The samples tested included pure salt mixture (Li_2CO_3 : K_2CO_3 for 66:34 molar ratio) and the nanomaterial at 1% mass fraction of SiO_2 .

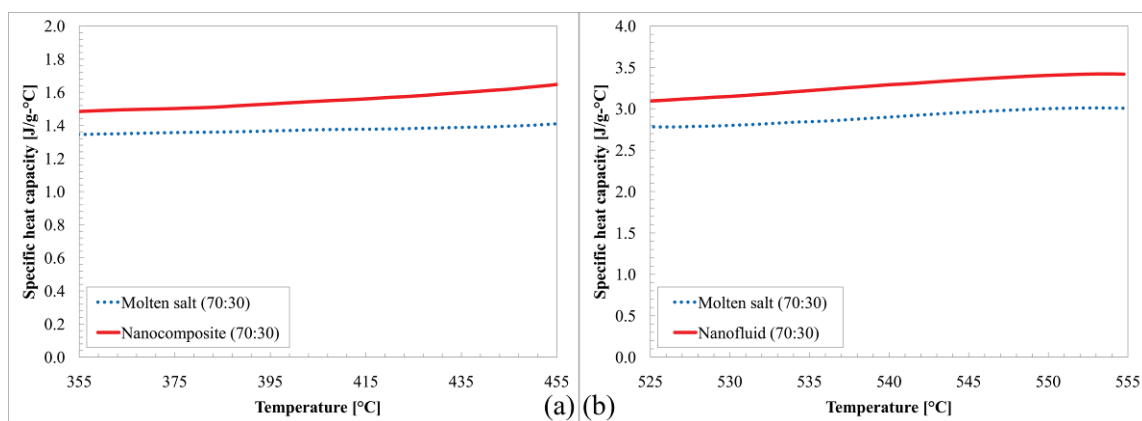


Figure 31. Variation of specific heat capacity with temperature for (a) solid phase, and (b) liquid phase. The samples tested included pure salt mixture (Li_2CO_3 : K_2CO_3 for 70:30 molar ratio) and the nanomaterial at 1% mass fraction of SiO_2 .

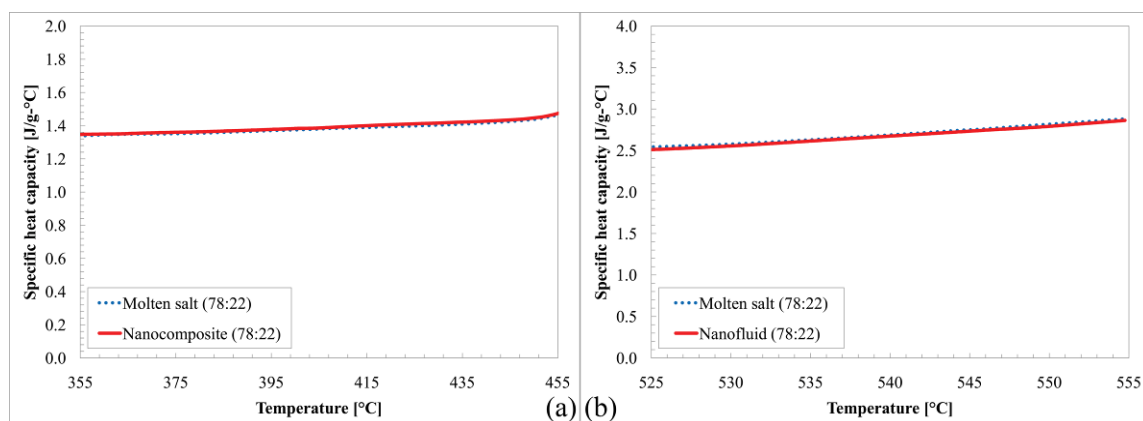


Figure 32. Variation of specific heat capacity with temperature for (a) solid phase, and (b) liquid phase. The samples tested included pure salt mixture ($\text{Li}_2\text{CO}_3 : \text{K}_2\text{CO}_3$ for 78:22 molar ratio) and the nanomaterial at 1% mass fraction of SiO_2 .

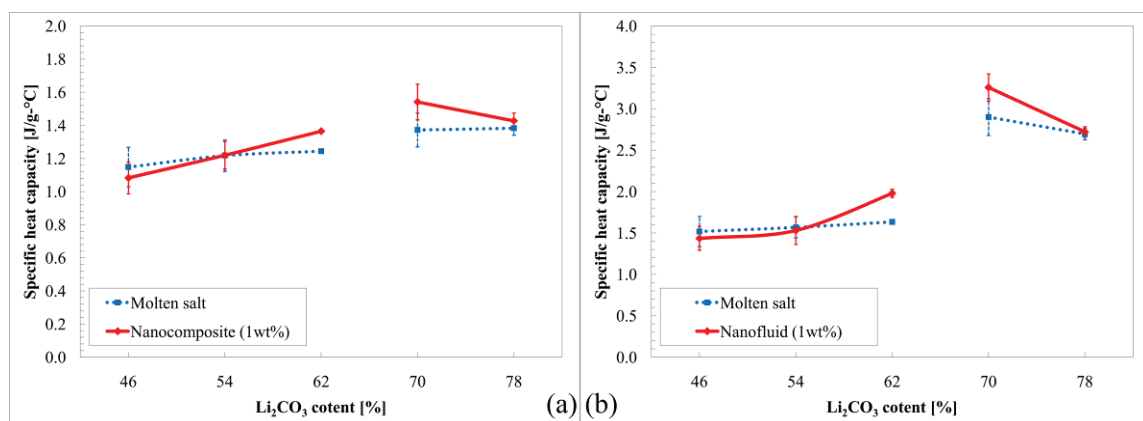


Figure 33. Variation in the specific heat capacity with composition of the molten salt ($\text{Li}_2\text{CO}_3\text{-K}_2\text{CO}_3$) for (a) solid phase; and (b) for liquid phase. The molar ratio of $\text{Li}_2\text{CO}_3\text{:K}_2\text{CO}_3$ was changed from 46:54 to 78:22. The SiO_2 mass concentration was fixed at 1% for the synthesized nanomaterials .

5.4.2 SEM/TEM analyses

Figure 34 shows the microstructure of (a) pure molten salt samples; and (b) for the nanomaterial samples. The molten salt composition was 46:54 (Li_2CO_3 : K_2CO_3 by molar ratio). This particular nanomaterial sample did not show any significant enhancement in the specific heat capacity. From the SEM analysis, it was observed that the nanomaterial contains significant amounts of agglomerated nanoparticles. Figure 34 (b) shows that regions with large amounts of agglomerated nanoparticles are located between the solidified salt crystals. This implies that for this salt composition, nanoparticles are not stable and therefore lead to significant amounts of agglomeration. The agglomerated nanoparticles lead to substantial reduction in the surface area (per unit volume) and cannot thus induce the formation of the modified sub-structures. Hence, the nanomaterial forms a mixture of bulk silica and molten salts. Therefore, for these samples the measured values of the specific heat capacity are consistent with the conventional model or “simple mixing rule” (Equation 14).

Figure 35 shows the microstructures for pure molten salt samples and the nanomaterial samples, for molten salt composition of 54:46 (Li_2CO_3 : K_2CO_3 by molar ratio). This particular nanomaterial also did not exhibit any significant enhancement in the specific heat capacity values. SEM image (Figure 35b) also confirmed significant amount of agglomeration of nanoparticles, which explains the absence of any enhancement in the specific heat capacity of the nanomaterial.

Figure 36 shows microstructures of pure molten salt samples and the nanomaterial samples for a molten salt composition of 70:30 ($\text{Li}_2\text{CO}_3:\text{K}_2\text{CO}_3$ by molar ratio). Contrary to the measurements from the previous samples, this particular nanomaterial exhibited 15 % enhancement in the specific heat capacity values for both solid and liquid phases. Micron-scale sub-structures were observed in the SEM images that resembled thorn-shaped structures. These structures may have different thermo-physical properties (and chemical compositions) compared with that of the bulk molten salt material and may have contributed to the enhancements in the values of the specific heat capacity of the nanomaterial.

Figure 37 shows microstructure of pure molten salt samples and nanomaterial samples for molten salt composition of 78:22 ($\text{Li}_2\text{CO}_3:\text{K}_2\text{CO}_3$ by molar ratio). This particular nanomaterial also did not show any significant enhancement in specific heat capacity. SEM image (Figure 37b) also confirmed that significant agglomeration of nanoparticles occurred for this sample. This explains the absence of any enhancement in the specific heat capacity of the nanomaterial.

Figure 38 shows high resolution SEM images of the special sub-structure observed in Figure 36. The image shows the modified structures resembling thorn-shaped features. The thorn-shaped structures seem to emanate at certain locations (location of nanoparticle). Figure 38 (b) is a back-scattered electron image of the thorn-shaped structures. The contrast in image intensity for the back-scattered electron image can be used to distinguish different materials, compositions, or phases. In the back scattered SEM images it was observed that the thorn-like structure is much brighter than

the surrounding bulk molten salt materials. The difference in contrast indicates that the thorn-like structure has a different composition of the molten salt materials. Hence, these sub-structures have different chemical composition and therefore different thermo-physical properties compared to that of the bulk molten salt material. Hence, it would be logical to conclude that the presence of these sub-structures contributes to the enhanced specific heat capacity of these nanomaterials.

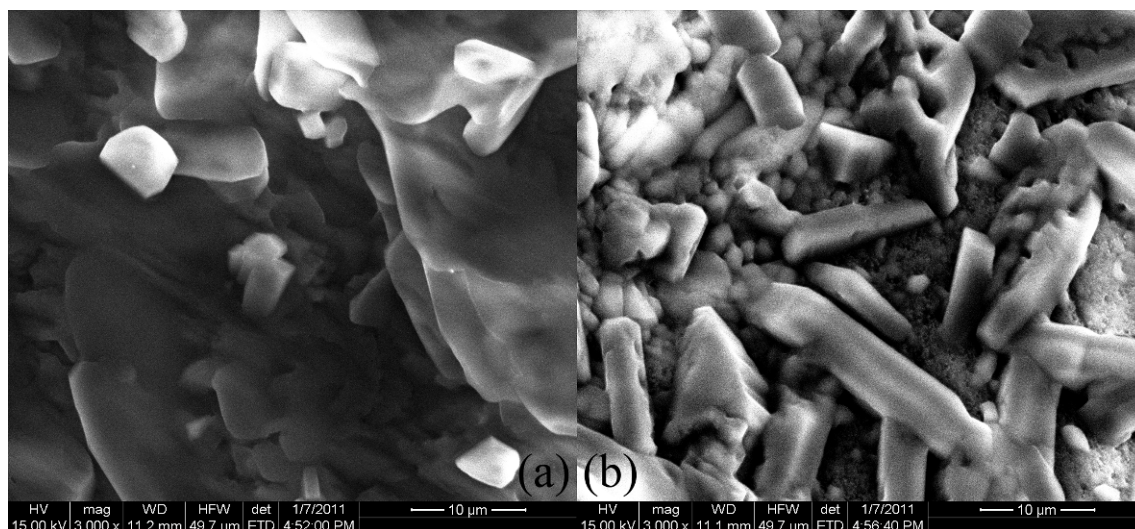


Figure 34. (a) Microstructure of pure molten salt, whose composition between Li_2CO_3 and K_2CO_3 is 46:54 by molar ratio. (b) Microstructure of corresponding molten salt nanomaterials (SiO_2 nanoparticle at 1% mass concentration in Li_2CO_3 - K_2CO_3 base salt), whose molten salt composition is 46:54 by molar ratio. It was observed that significant agglomeration of nanoparticles exists in these nanomaterial samples.

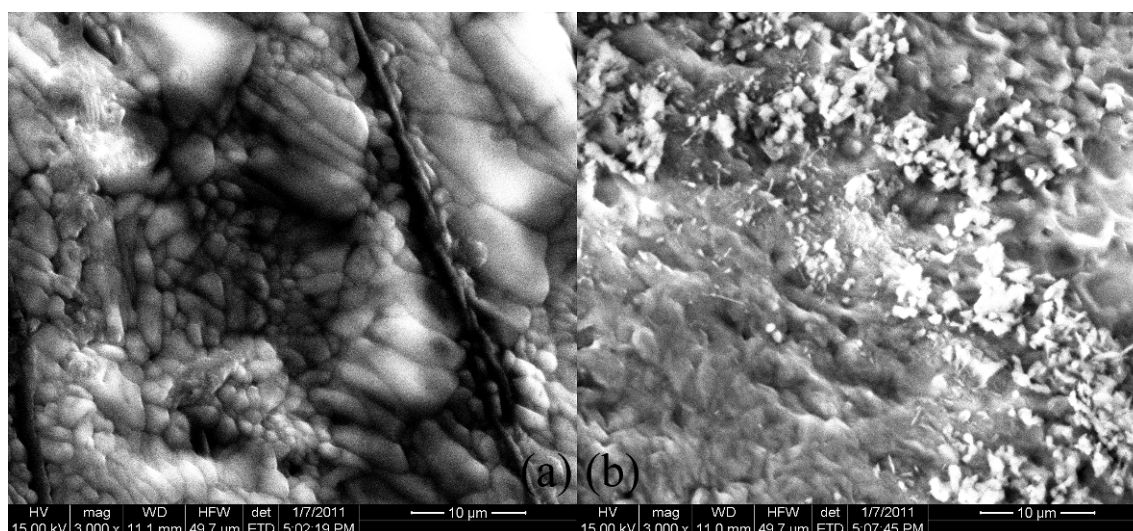


Figure 35. (a) Microstructure of pure molten salt, whose composition between Li_2CO_3 and K_2CO_3 is 54:46 by molar ratio. (b) Microstructure of molten salt nanomaterials (SiO_2 nanoparticle at 1% mass concentration in Li_2CO_3 - K_2CO_3 base salt), whose molten salt composition is 54:46 by molar ratio. It was observed that significant agglomeration of nanoparticles exists in these nanomaterial samples.

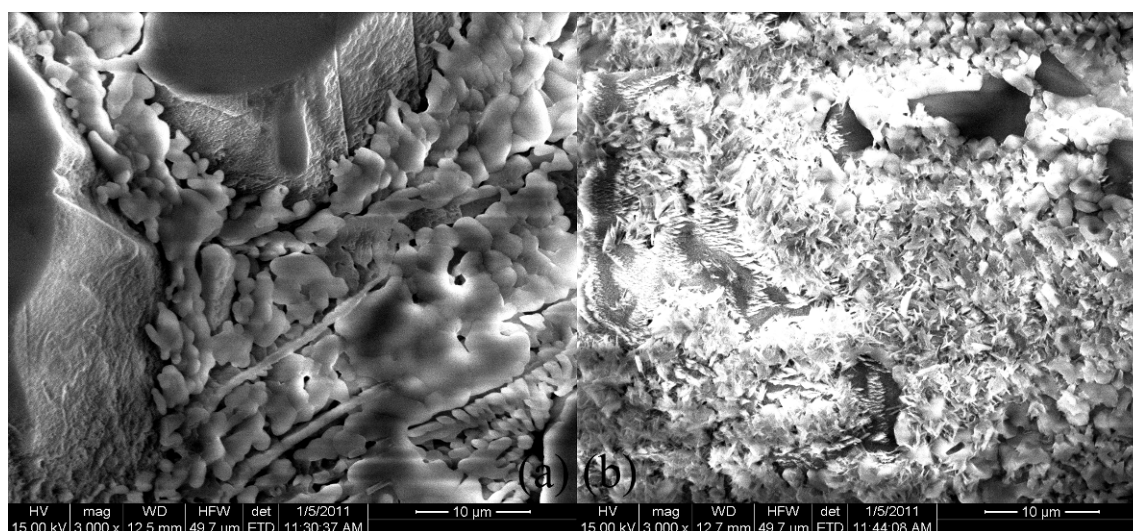


Figure 36. (a) Microstructure of pure molten salt, whose composition between Li_2CO_3 and K_2CO_3 is 70:30 by molar ratio. (b) Microstructure of molten salt nanomaterials (SiO_2 nanoparticle at 1% mass concentration in Li_2CO_3 - K_2CO_3 base salt), whose molten salt composition is 70:30 by molar ratio. Similar to the nanomaterial, whose molten salt composition is 62:38 with 26 % enhancement in specific heat capacity, this nanomaterial was also observed to develop special sub-structures resembling thorn-like shapes. The specific heat capacity was also enhanced by 15 % for this sample compared to that of the base molten salt (70:30).

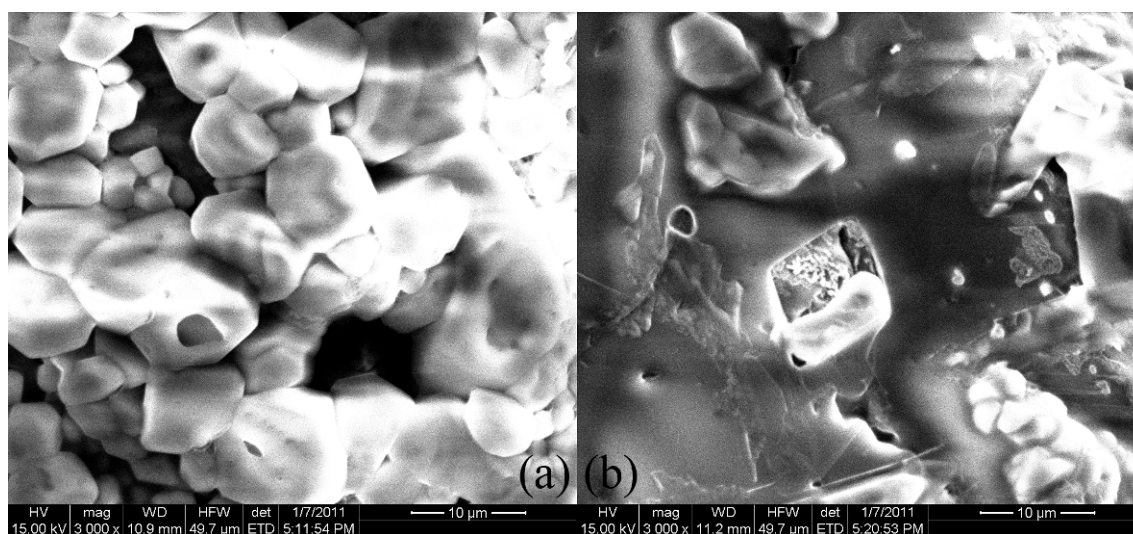


Figure 37. (a) Microstructure of pure molten salt, whose composition between Li_2CO_3 and K_2CO_3 is 78:22 by molar ratio. (b) Microstructure of molten salt nanomaterials (SiO_2 nanoparticle nanoparticle at 1% mass concentration in Li_2CO_3 - K_2CO_3 base salt), whose molten salt composition is 78:22 by molar ratio. It was observed that significant agglomeration of nanoparticles exists in these nanomaterial samples.

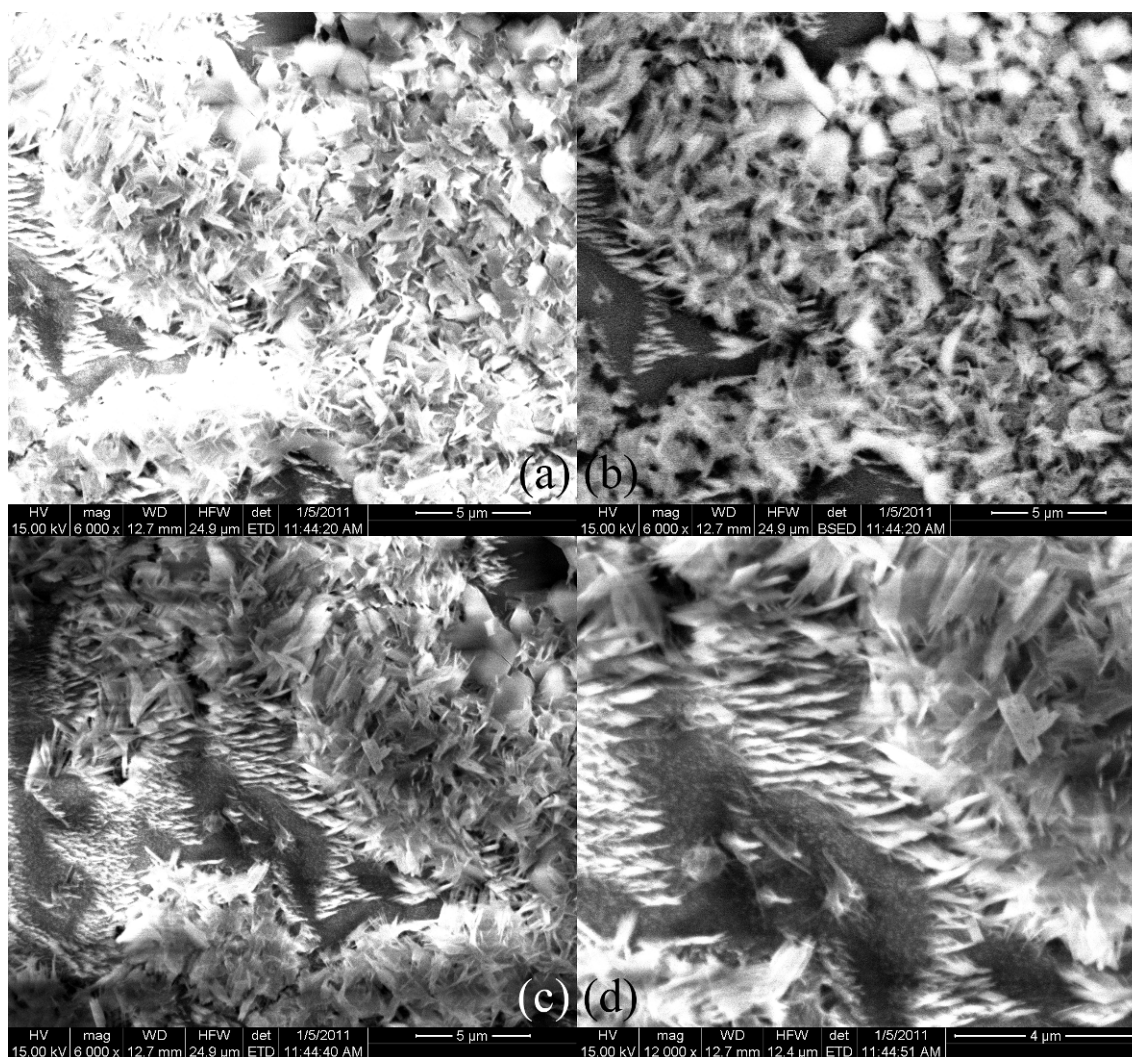


Figure 38. SEM images of molten salt nanomaterials (SiO_2 nanoparticle at 1% mass concentration in $\text{Li}_2\text{CO}_3\text{-K}_2\text{CO}_3$ base salt), whose molten salt composition is 78:22 by molar ratio (Figure 32). The formation of special sub-structure was also observed for these nanomaterial samples. No agglomeration of nanoparticles was observed.

5.4.3 Discussions

Conventional thermal equilibrium model (macroscopic model, also known as “simple mixing model,” cf. Equation 14) was used to predict the enhancement of the specific heat capacity of the nanomaterials. According to the simple mixing model (Equation 14), the specific heat capacity of the nanomaterials should be slightly lower than that of the base material, since the specific heat capacity of the nanoparticles are lower than that of the base material and the mass concentration is extremely low (1 %). Tables 14 and 15 show the comparisons between the predictions by the simple mixing model (Equation 14) and experimental data for solid phase (nanocomposite) and liquid phase (nanofluid), respectively. It was observed that nanomaterials (46:54, 54:46, and 78:22 by molar ratio), whose compositions are far away from the transition region (66 % of Li_2CO_3 content by molar ratio), were in good agreement with the predictions by the simple mixing model (Equation 14). On the other hand, nanomaterials (62:38 and 70:30 by molar ratio), whose compositions are closer to that of the transition region, did not agree with the prediction by the simple mixing model (Equation 14). The enhancement in specific heat capacity of nanomaterial (62:38 by molar ratio) and nanomaterial (70:30 by molar ratio) were 21 % and 12 % at liquid phase (10 % and 12 % at solid phase), respectively. In Section 5.4.2, material characterization analyses were performed using a scanning electron microscopy. It was observed that the nanomaterials (46:54, 54:46, and 78:22 by molar ratio), whose specific heat capacity did not change significantly, contained significant amounts of agglomerated nanoparticles. This

indicates that the nanoparticles in those nanomaterials were unstable and caused significant amounts of agglomeration (and consequently precipitated from the solution formed by the molten salt). In such an event, a simple mixture of molten salts and micron-sized particles were obtained, which no longer qualifies to be termed as a “nanomaterial”.

In contrast, no agglomeration of nanoparticles was observed in the molten salt samples, whose compositions were 62:38 and 70:30. The enhanced specific heat capacity of these nanomaterials can be due to the presence of the modified structure of molten salts (as observed in the electron microscopy images). It is possible that these modified structures enable alternate energy storage mechanisms which were not apparent in this study and can be the topic of future investigations (as mentioned in Section 5.3).

Table 14. Solid Phase Data. Discrepancy between the the experimental data and the predictions from the simple mixing model (Equation 14). (*: measurement uncertainty).

$\text{Li}_2\text{CO}_3\text{:K}_2\text{CO}_3$	Experiment (*)	Model Prediction	Error (%)
46:54	1.08 (3.4%)	1.15	-6 %
54:46	1.22 (2.4%)	1.21	0 %
62:38	1.37 (0.1%)	1.23	10 %
70:30	1.54 (1.8%)	1.36	12 %
78:22	1.43 (1.0%)	1.37	3 %

Table 15. Liquid Phase Data. Discrepancy between the experimental data and the prediction by the simple mixing model (Equation 14). (*: measurement uncertainty)

$\text{Li}_2\text{CO}_3\text{:K}_2\text{CO}_3$	Experiment (*)	Model Prediction	Error (%)
46:54	1.44 (5.1%)	1.51	-6 %
54:46	1.53 (4.9%)	1.56	-2 %
62:38	1.98 (1.4%)	1.63	21 %
70:30	3.26 (2.8%)	2.88	12 %
78:22	2.72 (1.3%)	2.68	1 %

5.5 Thermal Conductivity Results

DSC and LFA instruments were used to measure the specific heat capacity and the thermal diffusivity of the samples, respectively. The thermal conductivity of samples was calculated based on the measured values of the specific heat capacity, the thermal diffusivity, and the density of the samples. In this study the eutectic of $\text{Li}_2\text{CO}_3\text{-K}_2\text{CO}_3$ was explored as the solvent for the SiO_2 nanoparticles. The mass concentration of the nanoparticles was fixed at 1 % to enable consistent comparison with the previous studies in the literature. The specific heat capacity measurements were repeated three times and the thermal diffusivity measurements were repeated five times to ensure the repeatability of the measurements. Figure 39 shows the specific heat capacity of the pure eutectic salt and the nanocomposite at the temperature values of 150 °C, 225 °C, and 300 °C. The specific heat capacity of the nanocomposite sample was enhanced by 5 ~ 15 % over that of the pure eutectic salt sample.

To verify the accuracy of the measurement, the specific heat capacity of the pure eutectic salt samples were compared with the data reported in the literature. As shown in Table 16, the difference in the specific heat capacity between the measurements performed in this study and the literature data was within 1 % ~ 6 %.

The thermal diffusivities of the pure eutectic salt samples and the nanocomposite samples were measured using a LFA by Dynalene Laboratory (the data is presented in Figure 40 and the table on page 111). The thermal diffusivity (for pure eutectic salt as well as the nanocomposite) linearly decreased with temperature. The enhancement of the

thermal diffusivity of the nanocomposite samples was observed to be 25 ~ 28 % over that of the pure eutectic salt samples. The measurement uncertainty was estimated to be less than 1 %.

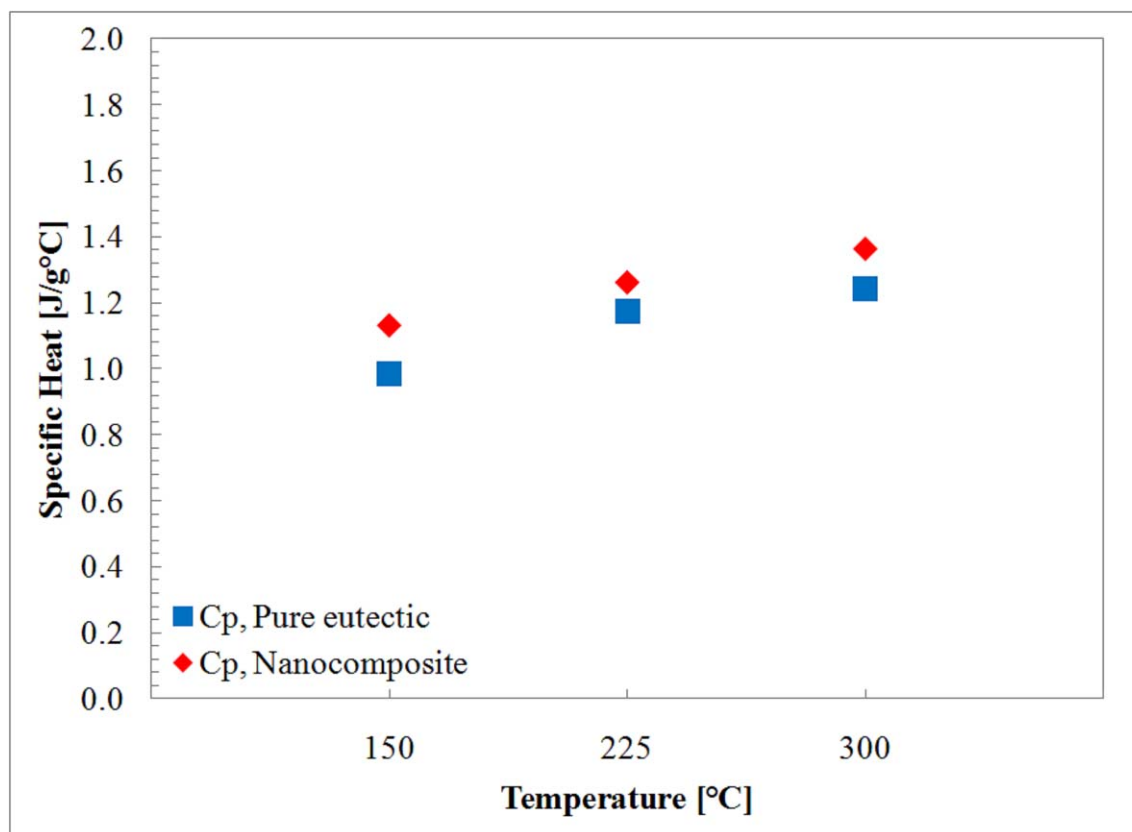


Figure 39. Comparison of the specific heat capacity measurements of the base material of lithium carbonate and potassium carbonate (62:38 molar ratio) with that of the nanocomposite (synthesized by addition of SiO_2 nanoparticles at a mass concentration of 1%).

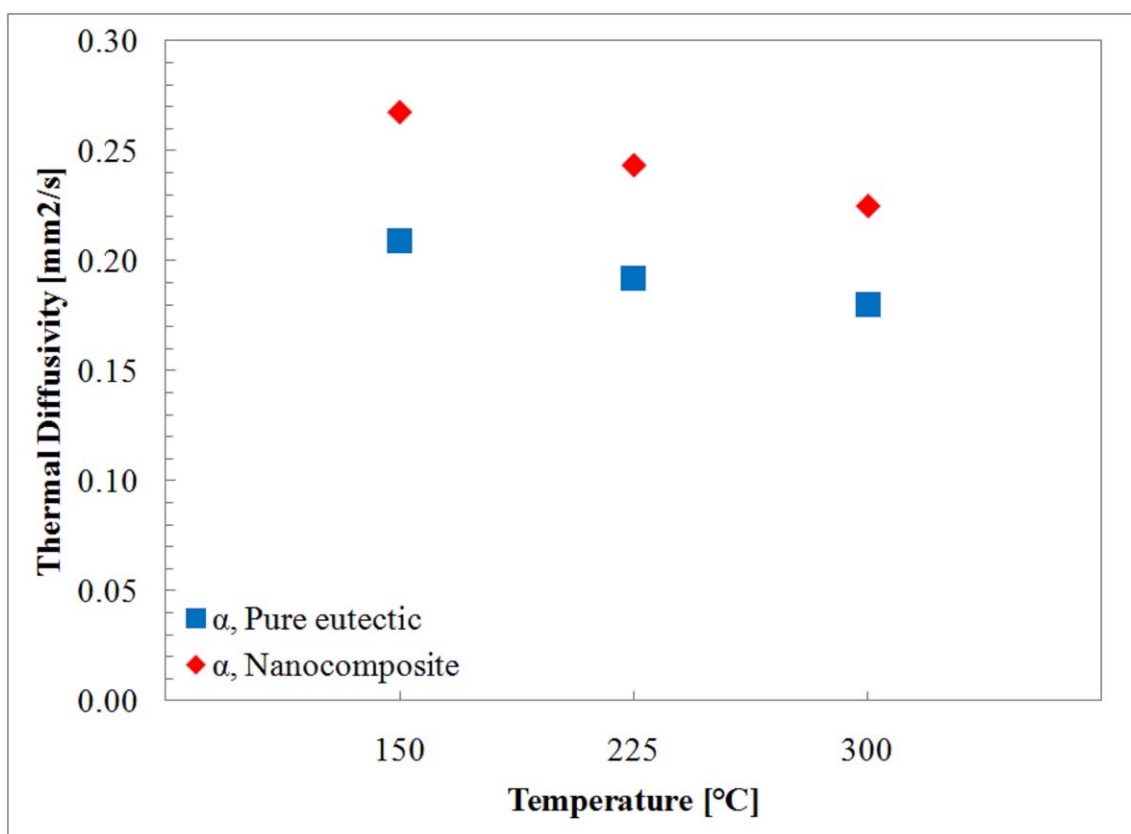


Figure 40. Comparison of the thermal diffusivity values of the pure eutectic of lithium carbonate and potassium carbonate (62:38 molar ratio) with that of the nanocomposite (synthesized by addition of SiO₂ nanoparticles at a mass concentration of 1%).

The thermal conductivity was calculated based on the specific heat capacity and the thermal diffusivity of the pure eutectic samples and the nanocomposite samples. The density of the pure eutectic was obtained from the literature and the density of the nanocomposite was calculated by using a simple mixing rule. The thermal conductivity of the base material and the nanocomposite are shown in Figure 41 and listed in Table 16. The thermal conductivity of the nanocomposite was enhanced by 37 % ~ 47 %.

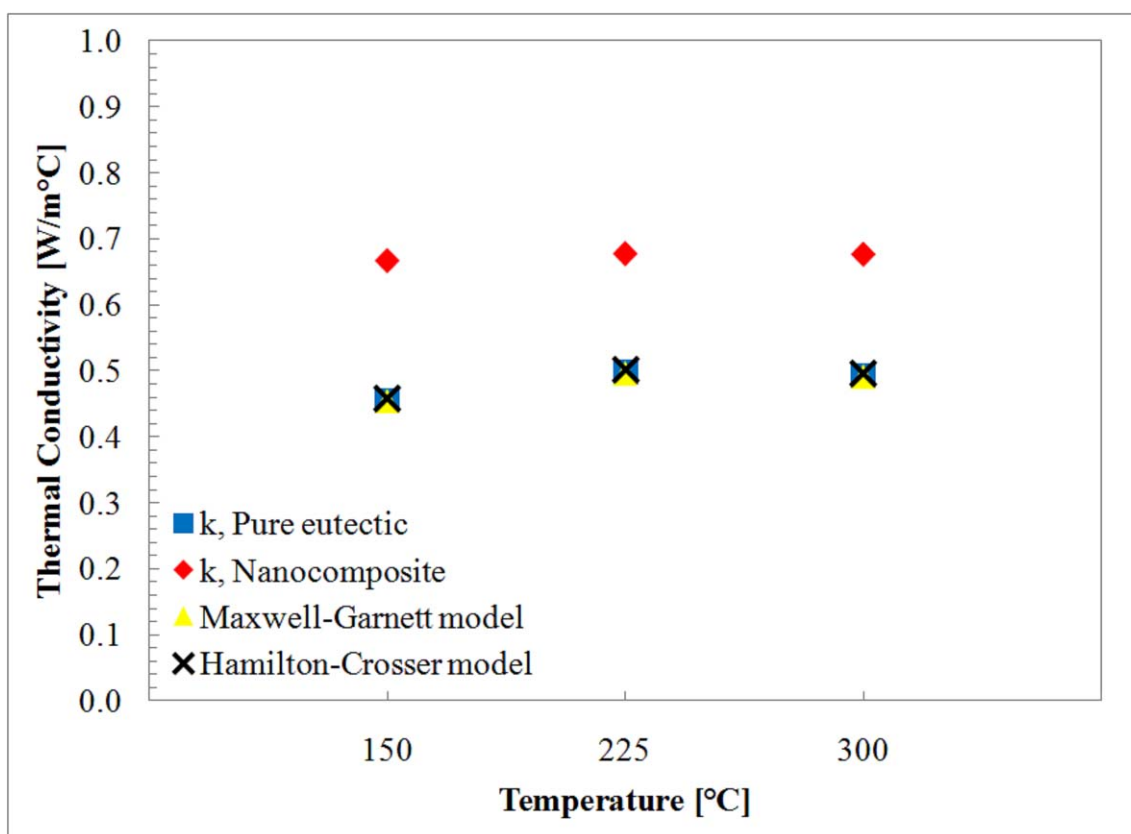


Figure 41. Comparison of the thermal conductivity values of the pure eutectic of lithium carbonate and potassium carbonate (62:38 molar ratio) with that of the nanocomposite (synthesized by addition of nanoparticles at a mass concentration of 1%). Theoretical estimates using the Maxwell-Garnett model [47] and the Hamilton-Crosser model [58] are plotted for comparison (This is discussed in section 5.6.).

Table 16. Density, specific heat capacity, thermal diffusivity, and thermal conductivity of the pure eutectic salt and the SiO₂ nanocomposite (at mass concentration of 1%).

Temperature	150 °C	225 °C	300 °C
ρ_b^*	2.202 g/cm ³	2.202 g/cm ³	2.202 g/cm ³
$C_{P,b}$	0.987 J/gK	1.176 J/gK	1.244 J/gK
(literature data **)	(1.053 J/gK)	(1.140 J/gK)	(1.227 J/gK)
(measurement error, %)	(6%)	(3%)	(1%)
α_b	0.209 mm ² /s	0.192 mm ² /s	0.180 mm ² /s
k_b	0.455 W/mK	0.498 W/mK	0.493 W/mK
ρ_t^*	2.206 g/cm ³	2.206 g/cm ³	2.206 g/cm ³
$C_{p,t}$	1.131 J/gK	1.263 J/gK	1.365 J/gK
(Enhancement %)	(15%)	(7%)	(10%)
α_t	0.267	0.243 mm ² /s	0.225 mm ² /s
(Enhancement %)	(28%)	(27%)	(25%)
k_t	0.668 W/mK	0.678 W/mK	0.677 W/mK
(Enhancement %)	(47%)	(36%)	(37%)

(*: density was assumed to be constant with temperature, **: reference [5])

5.6 Discussions: Thermal Conductivity of Nanomaterial

The measured values of thermal conductivity were compared with the conventional theoretical models, such as Hamilton-Crosser model (Equation 16) and Maxwell-Garnett model (Equation 17).

The Hamilton-Crosser model is expressed as [58]:

$$k_t = k_b \left[\frac{k_{np} + (n-1)k_b - (n-1)V_{np}(k_b - k_{np})}{k_{np} + (n-1)k_b + V_{np}(k_b - k_{np})} \right] \quad (16)$$

where k , n , and V are thermal conductivity, empirical shape factor ($n=3$ for a spherical nanoparticle), and volume fraction, respectively. Subscript t , b , and np denote total (or effective) value for the nanocomposite sample, the solvent material (molten salt eutectic), and the nanoparticle, respectively.

The Maxwell-Garnett model is expressed as [47]:

$$k_t = k_b \left[\frac{(1 + 4 \frac{R_b k_b}{d}) + 2V_{np} (1 - 2 \frac{R_b k_b}{d})}{(1 + 4 \frac{R_b k_b}{d}) - V_{np} (1 - 2 \frac{R_b k_b}{d})} \right] \quad (17)$$

where R_b is interfacial thermal resistance between a nanoparticle and surrounding solvent material, and d is the diameter of the nanoparticle. The interfacial thermal resistance between SiO_2 and eutectic of Li_2CO_3 and K_2CO_3 can be computed numerically and was reported to be $6.8 \times 10^{-9} \text{ m}^2\text{K/W}$ in the computational study (Section 3). The prediction by the two models (Equations 16 and 17) and the experimentally measured thermal conductivity values are listed in Table 17 and also plotted in Figure 41. It was observed that the two models failed to predict the large enhancements in the thermal conductivity values that were measured for the nanocomposite samples. The percolation networks observed in the electronmicroscopy images are potentially responsible for the experimentally measured enhancements in the thermo-physical properties of the nanomaterial samples (i.e., both for thermal conductivity and specific heat capacity).

Table 17. Comparison of experimentally measured data with theoretical estimates for the thermal conductivity of SiO₂ nanocomposite at 1% concentration by weight.

Thermal conductivity, k	150 °C	225 °C	300 °C
Pure Eutectic	0.455 W/mK	0.498 W/mK	0.493 W/mK
Standard deviation	0.026923	0.016275	0.015136
Maxwell-Garnett model	0.455 W/mK	0.497 W/mK	0.492 W/mK
(Enhancement %)	(0%)	(0%)	(0%)
Hamilton-Crosser model	0.458 W/mK	0.501 W/mK	0.496 W/mK
(Enhancement %)	(0%)	(0%)	(0%)
SiO ₂ nanocomposite	0.668 W/mK	0.678 W/mK	0.677 W/mK
(Enhancement %)	(47%)	(36%)	(37%)
Standard deviation	0.179	0.039	0.024

5.7 New Nanomaterial Synthesis Method

A new method was developed for the synthesis of the nanomaterials used in this study. Though this method is not perfect and the technique is subject to judgement of the experimenter in selecting appropriate samples – this is mentioned here nonetheless for the sake of completeness in reporting the experimental protocols developed in this study. In the new method, additional modifications were made for the evaporation technique that was used to prevent water from boiling while enabling rapid evaporation.

After ultra-sonication of the aqueous salt solution mixed with nanoparticles, the aqueous solution was then poured into a large glass petri-dish (10 cm in diameter) and subsequently heated on a hot plate (C-MAG HP7, IKA), which was maintained at 100 °C (Figure 42). Due to the thermal resistance between the hot plate and the container (as well as thermal resistance due to convective heat transfer within the solution), the solution was maintained at 60~70 °C until the water was completely evaporated without causing any nucleation of bubbles or pool boiling. The dried nanomaterial (which is termed as the nanocomposite, for the nanomaterial in the solid phase) was then heated to 300 °C for 2 hours to remove the remaining chemically bonded water from the nanomaterial. All procedures were performed in a glove box with filtered clean air circulation for rapid evaporation of the water as well as to minimize contamination.

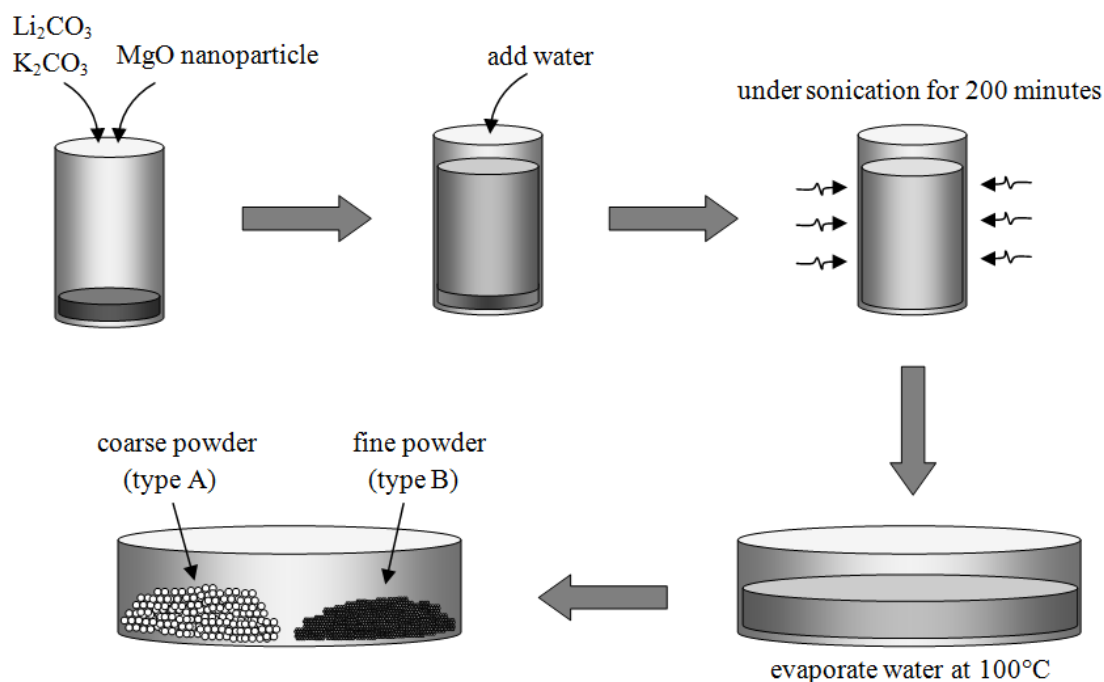


Figure 42. Schematic showing new procedure to synthesize molten salt nanomaterial by evaporation technique in order to prevent boiling of water during drying process (separation method).

5.7.1 SiO_2 / Li_2CO_3 - K_2CO_3 nanomaterial

Molten salt eutectic (Li_2CO_3 - K_2CO_3)-based SiO_2 nanomaterial was synthesized by the liquid solution method. Distilled water was added into the mixture of the pure eutectic salt and silica nanoparticles (at mass concentration of 1%). The aqueous salt solution was ultrasonicated to obtain a homogeneous dispersion of the nanoparticles. The solution was then maintained at 60 ~ 70 °C in a Petri dish to rapidly evaporate the water from the solution. Since the nanoparticles have lower water solubility than the molten salt eutectic, it is possible that a certain amount of the nanoparticles were

segregated from the molten salt eutectic and agglomerated during the later stages of the evaporation process.

Figure 43 shows the image of the dried nanomaterial after the evaporation was completed. It is observed that the nanomaterial formed two distinct types of amorphous powders. A quarter of the Petri dish was covered by very coarse amorphous powder (“Type-A nanomaterial”) and the rest was covered by fine amorphous powder (“Type-B nanomaterial”). Due to the low water solubility of the silica nanoparticles, the nanoparticles were separated and agglomerated at the end of the evaporation process, resulting in coarse amorphous powder. In contrast, the fine amorphous powder seems to have no (or minimal) agglomeration and is associated with uniformly dispersed nanoparticles in the dried salt samples.

5.7.1.1 Specific heat capacity results

Four samples of Type-A nanomaterials and four samples of Type-B nanomaterials were individually tested and their specific heat capacity results are shown in Figures 44 - 45 and Tables 18 - 21. Figure 44 shows the specific heat capacity of Type-A and Type-B nanomaterials at solid phase (“nanocomposites”) with temperature. The peak at ~ 500 °C is the melting peak of the base eutectic (488 °C). Table 18 and Table 19 show the average specific heat capacity of Type-A and Type-B nanocomposites between 355 °C and 455 °C, respectively.

The average specific heat capacity of Type-B nanocomposites was enhanced by 30 ~ 52 % compared to the specific heat capacity of the eutectic, while the average specific heat capacity of Type-A nanocomposites did not significantly change and the difference in the specific heat capacity between Type-A nanocomposite and the base salt eutectic is within the measurement uncertainty. (The measurement uncertainty is 1.9 ~ 2.0 %).

Figure 45 shows the variation of specific heat capacity with temperature for Type-A and Type-B nanomaterials in the liquid phase (“nanofluids”). The average specific heat capacity of Type-A and Type-B nanofluids between 525 °C and 555 °C are shown in Tables 20 - 21. The average specific heat capacity of Type-B nanofluids was enhanced significantly. Type-A nanofluids did not show any significant change in specific heat capacity compared with that of the pure eutectic salt and are within the range of the measurement uncertainty. (Measurement uncertainty is 2.2 ~ 2.4 %).

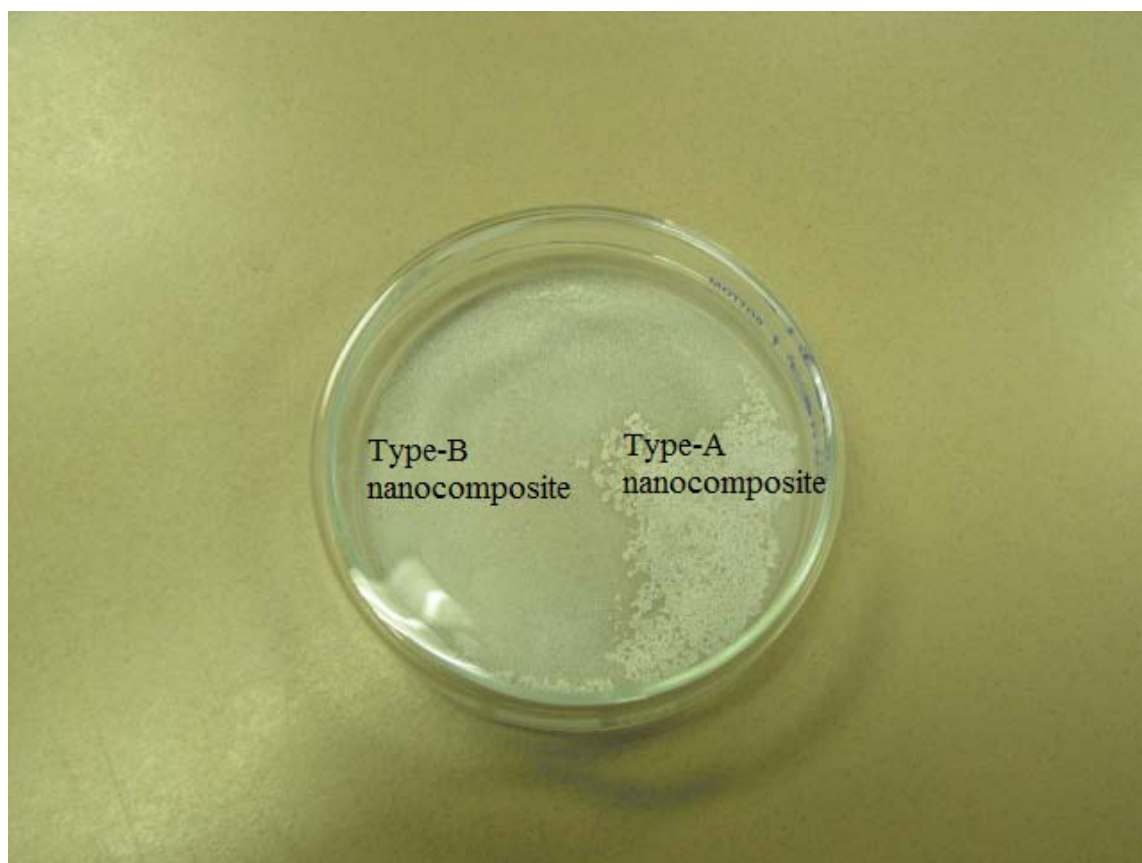


Figure 43. Image of dry amorphous powder of $\text{SiO}_2/\text{Li}_2\text{CO}_3\text{-K}_2\text{CO}_3$ nanomaterial (at mass concentration of 1.5 %) after the evaporation was completed. The image shows coarse amorphous powder (Type-A) and fine amorphous powder (Type-B).

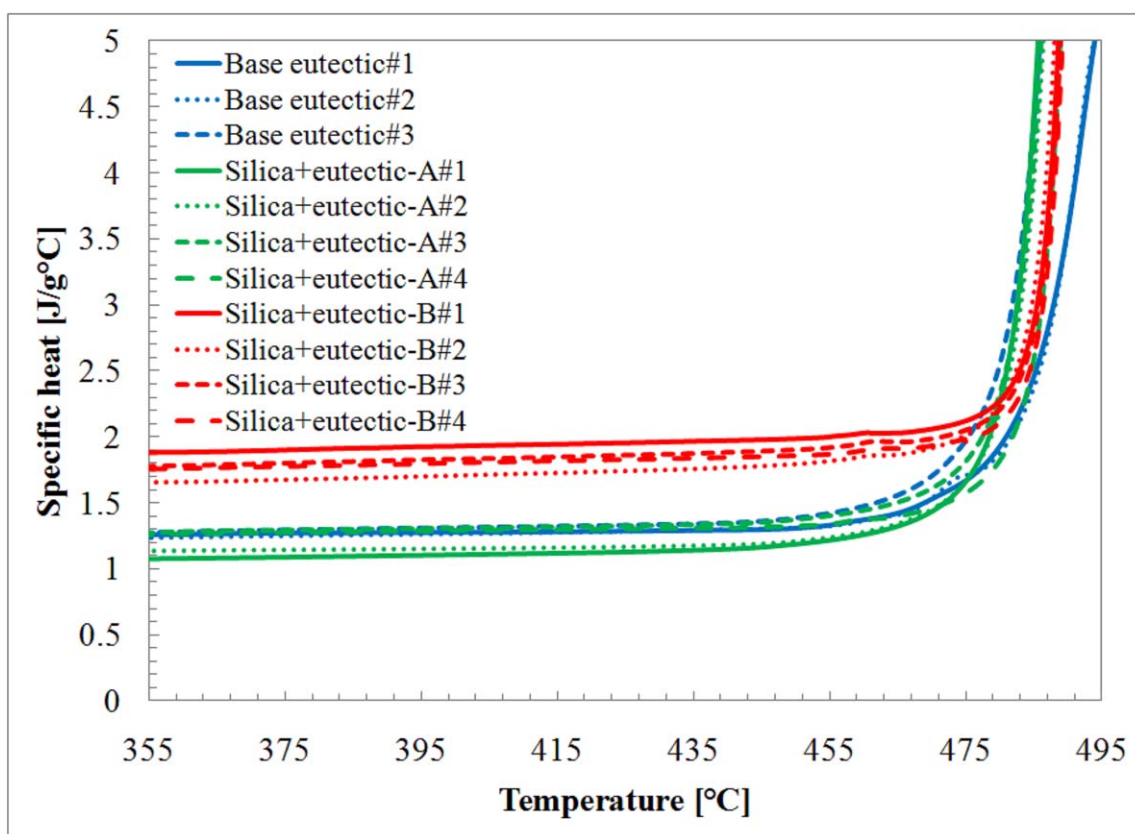


Figure 44. Variation of specific heat capacity with temperature (355 °C ~ 495 °C) for $\text{SiO}_2/\text{Li}_2\text{CO}_3\text{-K}_2\text{CO}_3$ nanocomposites.

Table 18. Specific heat capacity measurements (J /g-K) of Type-A $\text{SiO}_2/\text{Li}_2\text{CO}_3\text{-K}_2\text{CO}_3$ nanocomposites, which are obtained from the coarse powders of eutectics containing agglomerated nanoparticles. No significant change in the specific heat capacity values were observed – within the bounds of the measurement uncertainty (ϵ : standard deviation for all the thermo-cycle data for a sample).

C_p (J/g-K)	Pure Eutectic	Nano- composite type-A (#1)	Nano- composite type-A (#2)	Nano- composite type-A (#3)	Nano- composite type-A (#4)
1 st run	1.351	1.189	1.114	1.243	1.270
2 nd run	1.334	1.203	1.138	1.317	1.251
3 rd run	1.264	1.177	1.176	1.346	1.292
4 th run	1.229	1.144	1.225	1.347	1.352
Average	1.294	1.178	1.163	1.313	1.291
ϵ	0.060	0.025	0.048	0.049	0.044

Table 19. Specific heat capacity measurements (J /g-K) of Type-B $\text{SiO}_2/\text{Li}_2\text{CO}_3\text{-K}_2\text{CO}_3$ nanocomposites, that are obtained from fine amorphous powders of eutectics that contained uniformly dispersed nanoparticles with no (or minimal) agglomeration. (ϵ : standard deviations for all the thermo-cycle data for a given sample).

C_p (J/g-K)	Pure Eutectic	Type-B (#1)	Type-B (#2)	Type-B (#3)	Type-B (#4)
1 st run	1.351	1.880	1.669	1.762	1.706
2 nd run	1.334	1.913	1.720	1.793	1.764
3 rd run	1.264	1.919	1.741	1.830	1.799
4 th run	1.229	1.930	1.747	1.864	1.838
5 th run		1.967	1.721	1.910	1.877
6 th run		1.987	1.696	1.902	1.885
7 th run		2.007	1.703	1.902	1.912
8 th run		2.014	1.657	1.887	1.806
9 th run		2.025	1.603	1.838	1.719
10 th run		2.011	1.595	1.773	1.693
11 th run		1.993	1.639	1.684	1.634
12 th run		1.986	1.645	1.604	1.579
Average	1.294	1.969	1.678	1.812	1.769
ϵ	0.060	0.047	0.051	0.095	0.105

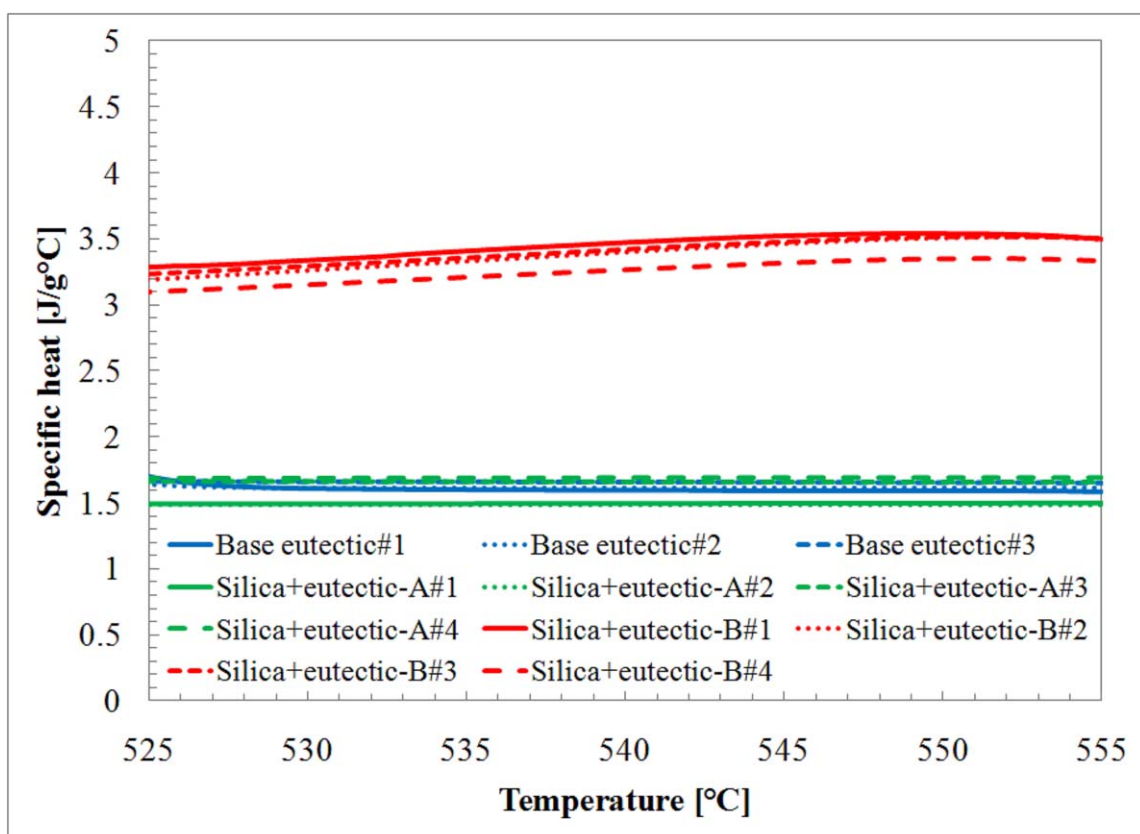


Figure 45. Variation of specific heat capacity of $\text{SiO}_2/\text{Li}_2\text{CO}_3\text{-K}_2\text{CO}_3$ nanofluids with temperature (525 °C ~ 555 °C). The average specific heat capacity of Type-B nanofluid was enhanced significantly over that of the pure molten salt eutectic, while no enhancement of specific heat capacity was observed for Type-A nanofluid.

Table 20. Specific heat capacity measurements (J /g-K) of Type-A $\text{SiO}_2/\text{Li}_2\text{CO}_3\text{-K}_2\text{CO}_3$ nanofluids, which are obtained from the coarse powders of eutectics containing agglomerated nanoparticles. No significant change in the specific heat capacity values were observed – within the bounds of the measurement uncertainty (ε : standard deviation for all the thermo-cycle data for a sample).

C_p (J/g-K)	Pure Eutectic	Nanofluid-A (#1)	Nanofluid-A (#2)	Nanofluid-A (#2)	Nanofluid-A (#4)
1 st run	1.692	1.567	1.420	1.545	1.644
2 nd run	1.674	1.593	1.456	1.652	1.637
3 rd run	1.581	1.574	1.502	1.701	1.701
4 th run	1.533	1.536	1.564	1.718	1.775
Average	1.620	1.567	1.486	1.654	1.689
Enhance- ment	-	-3 %	-8 %	2 %	4 %
ε	0.079	0.023	0.062	0.078	0.064

Table 21. Specific heat capacity measurements (J /g-K) of Type-B $\text{SiO}_2/\text{Li}_2\text{CO}_3\text{-K}_2\text{CO}_3$ nanofluids, that are obtained from fine amorphous powders of eutectics that contain uniformly dispersed nanoparticles with no (or minimal) agglomeration. (ε : standard deviations for all the thermo-cycle data for a given sample).

C_p (J/g-K)	Pure Eutectic	Nanofluid-B (#1)	Nanofluid-B (#2)	Nanofluid-B (#2)	Nanofluid-B (#4)
1 st run	1.692	3.405	3.429	3.414	3.184
2 nd run	1.674	3.435	3.484	3.455	3.232
3 rd run	1.581	3.500	3.521	3.498	3.316
4 th run	1.533	3.485	3.510	3.512	3.351
5 th run		3.540	3.497	3.561	3.450
6 th run		3.581	3.502	3.586	3.461
7 th run		3.602	3.527	3.655	3.510
8 th run		3.634	3.441	3.640	3.368
9 th run		3.623	3.377	3.578	3.232
10 th run		3.618	3.355	3.489	3.175
11 th run		3.646	3.421	3.343	3.109
12 th run		3.599	3.430	3.211	2.992
Average	1.620	3.556	3.458	3.495	3.282
ε	0.079	0.081	0.057	0.127	0.155

5.7.1.2 SEM / TEM analysis

SEM analyses were performed to observe the microstructure of Type-A and Type-B nanomaterials. Figure 46 shows images of Type-A nanomaterial sample, which did not show any enhancement in the specific heat capacity. Figure 47 shows the microstructure of Type-B nanomaterial sample, which showed the anomalous enhancement in the specific heat capacity. It was observed in Figure 47 that a special structure resembling a weave-shaped pattern was formed in the nanomaterial. These structures are only observed for Type-B nanomaterial and are expected to be responsible for the observed enhancements in the specific heat capacity of Type-B nanomaterial samples.

Furthermore, TEM analysis was performed to verify whether or not the nanoparticles were agglomerated when subjected to the repeated melting and solidification for implementing the thermal cycle protocols in the DSC. Figure 48 is the TEM image of the nanocomposite after the sample was subjected to the thermal cycling protocol in the DSC involving multiple cycles of melting and solidification (12 times). From the TEM image it was observed that the nanoparticles were not agglomerated, and remained well dispersed. The size distribution of the nanoparticles was found to range from 2 nm ~ 20 nm.

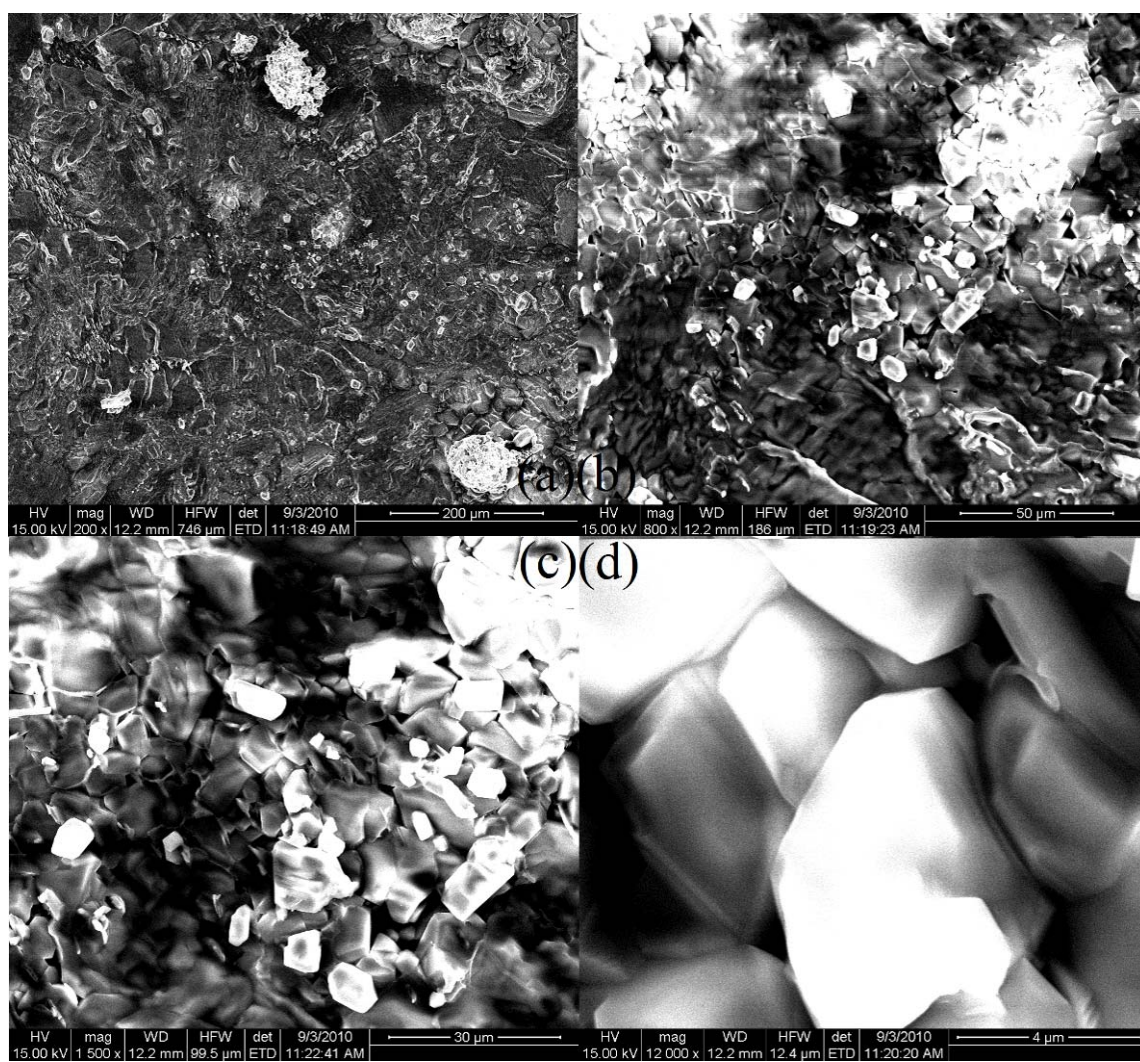


Figure 46. SEM images of Type-A $\text{SiO}_2/\text{Li}_2\text{CO}_3\text{-K}_2\text{CO}_3$ nanomaterial (coarse powder samples).

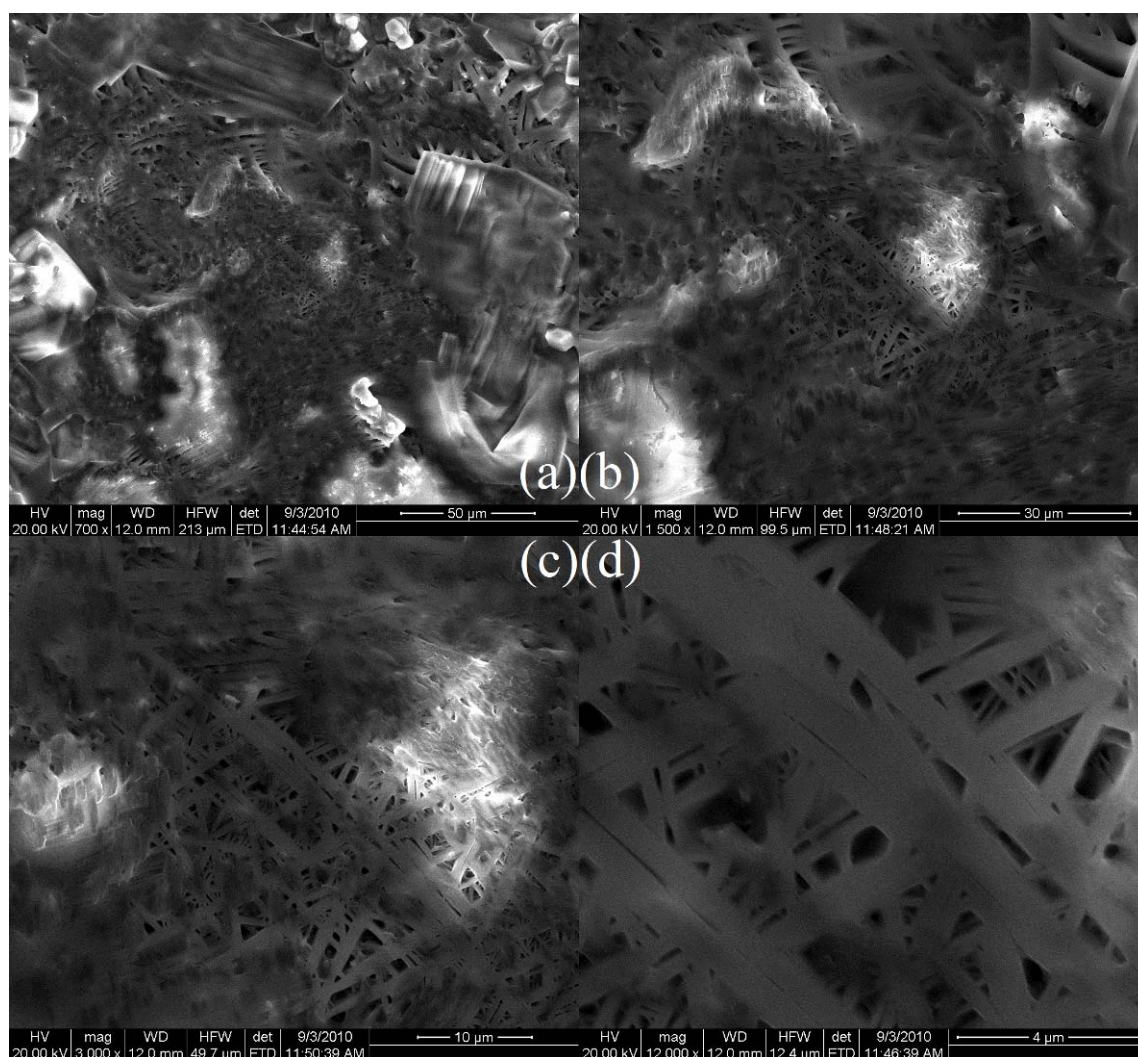


Figure 47. SEM images of Type-B $\text{SiO}_2/\text{Li}_2\text{CO}_3\text{-K}_2\text{CO}_3$ nanomaterial (fine powder samples), which showed the anomalously enhanced specific heat capacity at solid phase and at liquid phase. It was observed that the molten salt eutectic formed a very special structure resembling a weave-shaped pattern. This structure is potentially responsible for the anomalous enhancement of the specific heat capacity of Type-B nanomaterial, especially in the liquid phase (nanofluids).

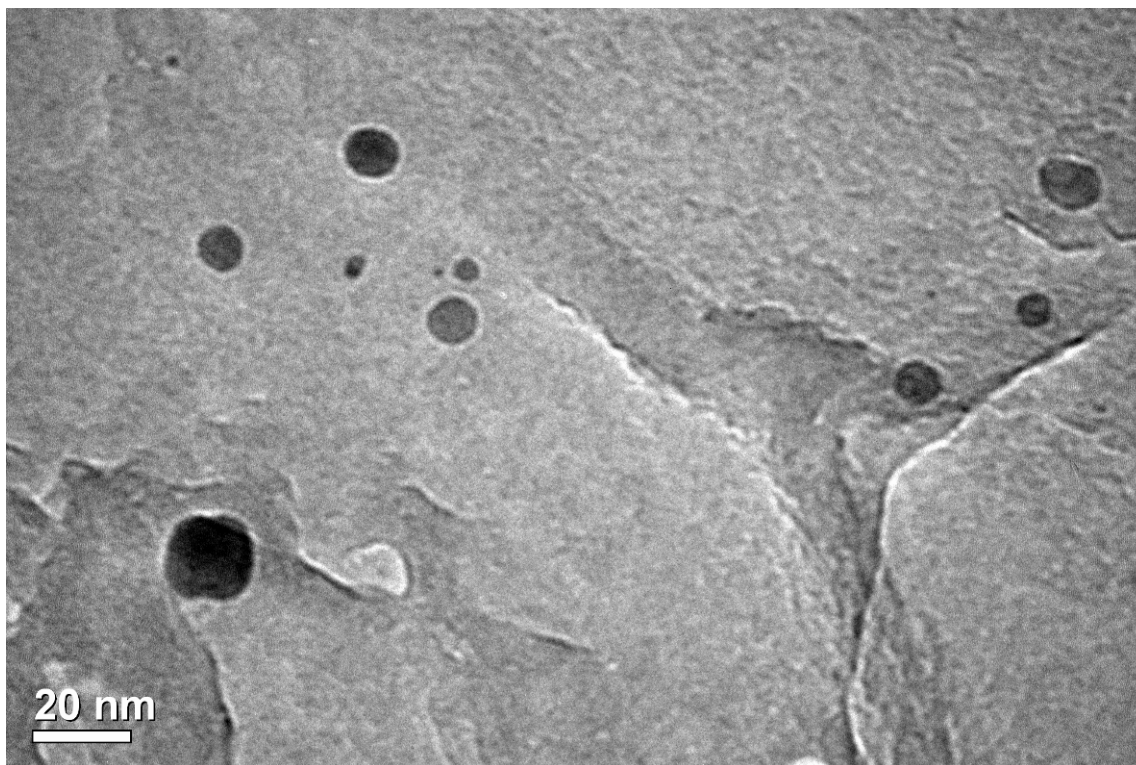


Figure 48. Transmission Electron Micrograph (TEM) of silica nanoparticles in the Type-B samples of $\text{SiO}_2/\text{Li}_2\text{CO}_3\text{-K}_2\text{CO}_3$ nanomaterial after thermal cycling in the DSC involving multiple melting and solidification. The image shows that the nanoparticles are not agglomerated and the nominal size of the nanoparticles is 2~20 nm.

5.7.2 $\text{MgO} / \text{Li}_2\text{CO}_3\text{-K}_2\text{CO}_3$ nanomaterial

Molten salt ($\text{Li}_2\text{CO}_3\text{-K}_2\text{CO}_3$)-based MgO nanomaterial was synthesized using the same method as that of the $\text{SiO}_2/\text{Li}_2\text{CO}_3\text{-K}_2\text{CO}_3$ nanomaterial (Section 5.7.1). MgO nanomaterial was observed to form two distinct types of amorphous powders. It is shown in Figure 49 that approximately half of the petri-dish was covered by very coarse amorphous powder (“Type-A nanomaterial”) and the rest was covered by fine amorphous powder (“Type-B nanomaterial”).

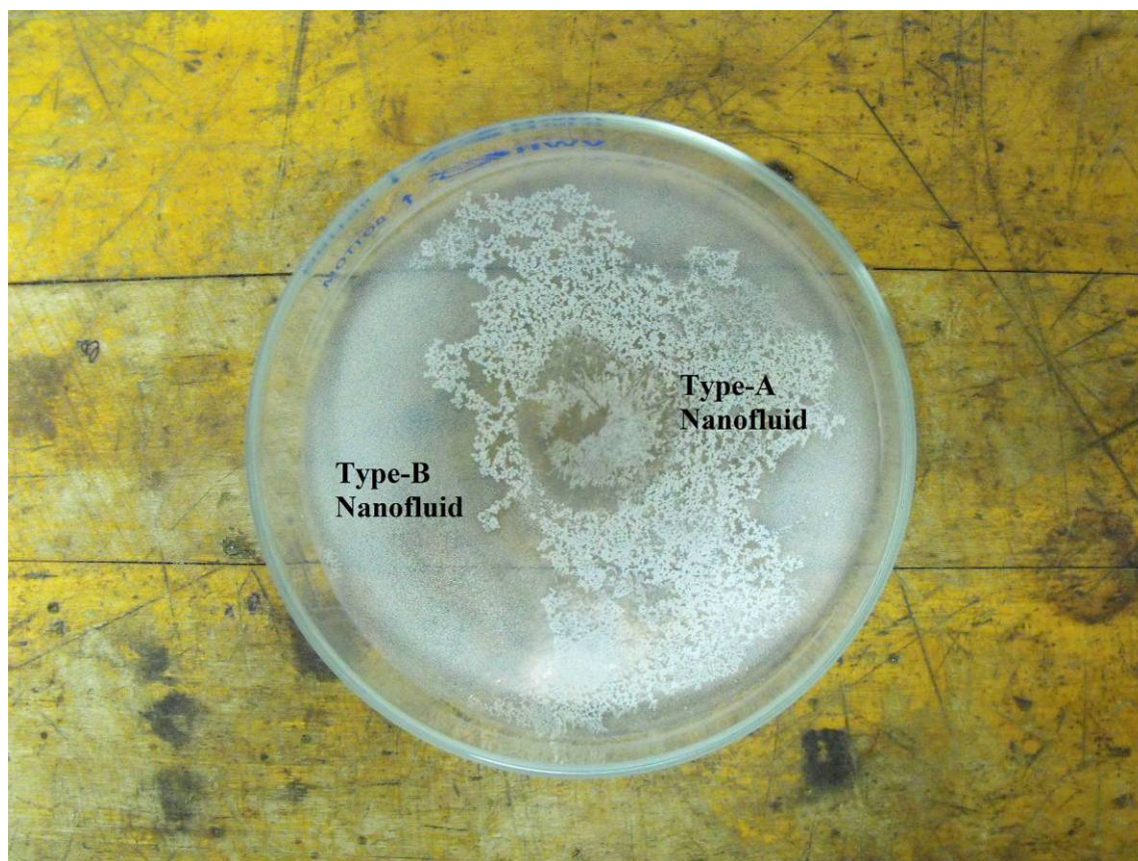


Figure 49. Image of dry amorphous powder of $\text{MgO/Li}_2\text{CO}_3\text{-K}_2\text{CO}_3$ nanomaterial (at mass concentration of 1.0 %) after complete evaporation during the drying process. The image shows the formation of coarse amorphous powder (Type-A) and fine amorphous powder (Type-B).

5.7.2.1 Specific heat capacity results

Four samples of Type-A nanomaterials and four samples of Type-B nanomaterials were synthesized and tested separately for measuring their specific heat capacity. The results from the measurements are shown in Figures 50-51 and Tables 22-25. Figure 50 shows the variation of specific heat capacity with temperature for Type-A and Type-B nanocomposites (solid phase). The peak at $\sim 500\text{ }^{\circ}\text{C}$ is the melting peak of the eutectic salt ($488\text{ }^{\circ}\text{C}$). Table 22 and Table 23 lists the measured value of the average specific heat capacity of Type-A and Type-B nanocomposites for the temperature range of $355\text{ }^{\circ}\text{C}$ - $455\text{ }^{\circ}\text{C}$. The average specific heat capacity of Type-A nanocomposites and Type-B nanocomposites did not show any significant variation yet were slightly enhanced ($2\% \sim 17\%$) compared with the pure eutectic. (The measurement uncertainty is estimated to be $1.1\% \sim 1.9\%$)

Figure 51 shows the variation of the specific heat capacity with temperature for Type-A and Type-B nanofluids (liquid phase). The average specific heat capacity of Type-A and Type-B nanofluids was measured for the temperature range of $525\text{ }^{\circ}\text{C}$ - $555\text{ }^{\circ}\text{C}$ and the results are listed in Tables 24 - 25. In contrast to the solid phase (nanocomposite) data, the average specific heat capacity of Type-B nanofluids was enhanced significantly, while the average specific heat capacity of Type-A nanofluids was enhanced by only $12 \sim 31\%$. The measurement uncertainty is estimated to be $2.7\% \sim 3.4\%$.

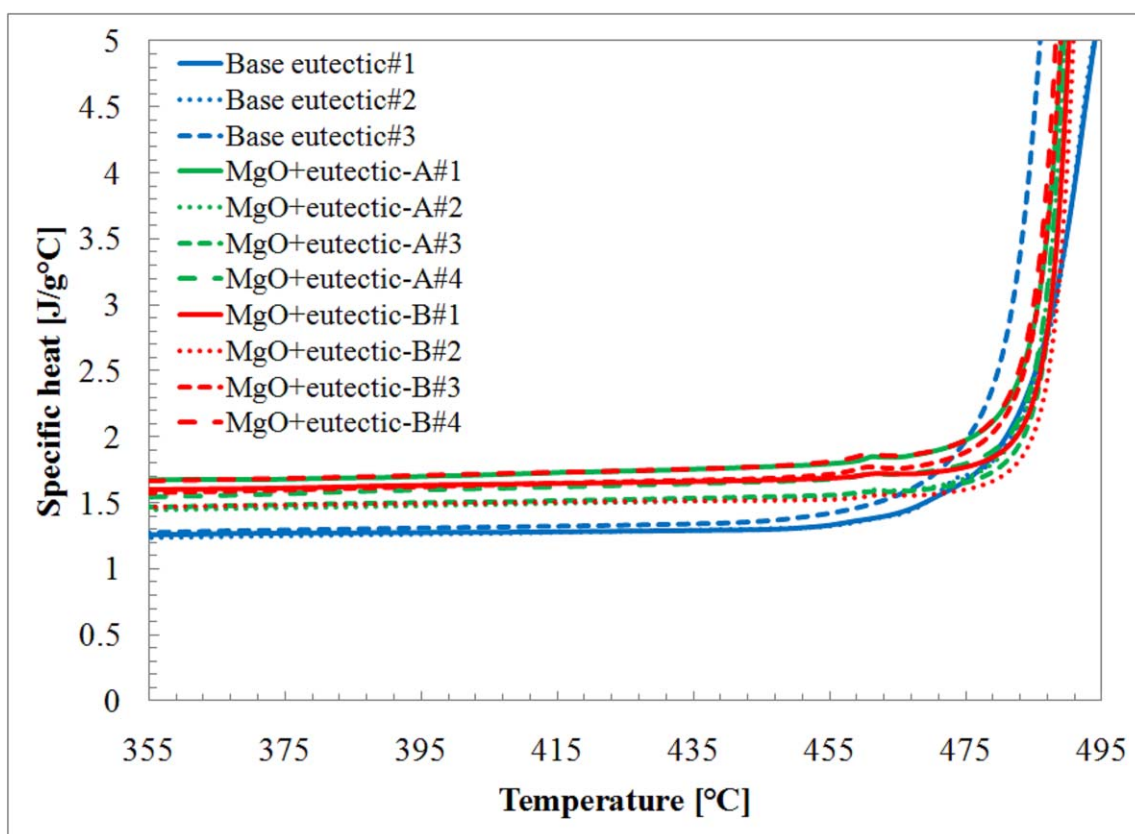


Figure 50. Variation of specific heat capacity with temperature (355 °C ~ 495 °C) for MgO/Li₂CO₃-K₂CO₃ nanocomposites. The average specific heat capacity of both nanocomposites were enhanced by 2 ~ 17 % over that of the pure molten salt eutectic.

Table 22. Specific heat capacity measurements (J /g-K) of Type-A MgO/Li₂CO₃-K₂CO₃ nanocomposites, which are obtained from the coarse powders of salts containing agglomerated nanoparticles. The average specific heat capacity of Type-A nanocomposites was enhanced by 2~16 % over that of the pure molten salt eutectic. (ϵ : standard deviation for all the thermo-cycle data for a sample).

C_p (J/g-K)	Pure Eutectic	Nano- composite type-A (#1)	Nano- composite type-A (#2)	Nano- composite type-A (#3)	Nano- composite type-A (#4)
1 st run	1.351	1.476	1.270	1.353	1.396
2 nd run	1.334	1.498	1.342	1.372	1.395
3 rd run	1.264	1.504	1.353	1.349	1.409
4 th run	1.229	1.514	1.340	1.272	1.427
Average	1.294	1.498	1.326	1.336	1.407
ϵ	0.060	0.016	0.038	0.044	0.015

Table 23. Specific heat capacity measurements (J /g-K) of Type-B nanocomposites of $\text{Li}_2\text{CO}_3\text{-K}_2\text{CO}_3$, that contain uniformly dispersed MgO nanoparticles with no (or minimal) agglomeration. (ε : standard deviations for all the thermo-cycle data for a given sample). Measurement uncertainty is 1.9 %.

C_p (J/g-K)	Pure Eutectic	Type-B (#1)	Type-B (#2)	Type-B (#3)	Type-B (#4)
1 st run	1.351	1.510	1.329	1.402	1.469
2 nd run	1.334	1.514	1.354	1.438	1.482
3 rd run	1.264	1.508	1.374	1.473	1.516
4 th run	1.229	1.480	1.392	1.511	1.510
5 th run			1.392		1.506
6 th run			1.399		1.503
7 th run			1.407		1.529
8 th run			1.413		1.530
9 th run			1.430		1.534
10 th run			1.431		1.539
11 th run			1.431		1.539
12 th run			1.434		1.505
Average	1.294	1.503	1.399	1.456	1.514
ε	0.060	0.015	0.033	0.047	0.022

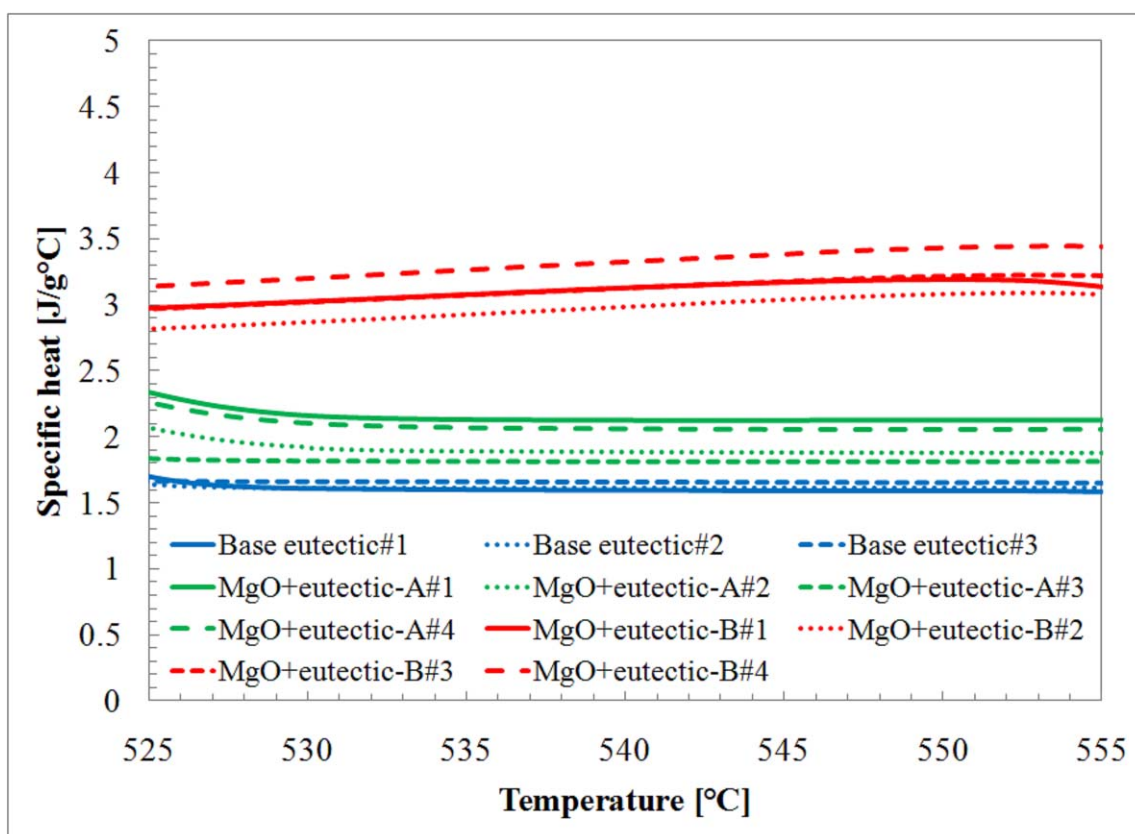


Figure 51. Variation of specific heat capacity temperature (525 °C ~ 555 °C) for MgO/ $\text{Li}_2\text{CO}_3\text{-K}_2\text{CO}_3$ nanofluids.

Table 24. Specific heat capacity measurements (J /g-K) of Type-A MgO/Li₂CO₃-K₂CO₃ nanofluids, which are obtained from the coarse powders of eutectics containing agglomerated nanoparticles. (ε : standard deviation for all the thermo-cycle data for a sample).

C _p (J/g-K)	Pure Eutectic	Nanofluid-A (#1)	Nanofluid-A (#2)	Nanofluid-A (#2)	Nanofluid-A (#4)
1 st run	1.692	2.110	1.797	1.809	2.037
2 nd run	1.674	2.118	1.883	1.835	2.036
3 rd run	1.581	2.130	1.923	1.842	2.059
4 th run	1.533	2.146	1.928	1.771	2.084
Average	1.620	2.126	1.883	1.814	2.054
ε	0.079	0.016	0.061	0.032	0.023

Table 25. Specific heat capacity measurements (J /g-K) of Type-B MgO/Li₂CO₃-K₂CO₃ nanofluids, that were obtained from the fine amorphous powders of eutectics that contain uniformly dispersed nanoparticles with no (or minimal) agglomeration. (ϵ : standard deviations for all the thermo-cycle data for a given sample).

C _p (J/g-K)	Pure Eutectic	Nanofluid-B (#1)	Nanofluid-B (#2)	Nanofluid-B (#2)	Nanofluid-B (#4)
1 st run	1.692	3.105	2.902	3.042	3.277
2 nd run	1.674	3.131	2.939	3.101	3.276
3 rd run	1.581	3.126	2.985	3.137	3.313
4 th run	1.533	3.104	3.022	3.197	3.335
5 th run			3.017		3.353
6 th run			3.037		3.362
7 th run			3.057		3.371
8 th run			3.068		3.377
9 th run			3.087		3.378
10 th run			3.085		3.381
11 th run			3.093		3.380
12 th run			3.094		3.355
Average	1.620	3.117	3.032	3.119	3.347
ϵ	0.079	0.014	0.063	0.065	0.038

5.7.2.2 SEM / TEM analysis

SEM analyses were performed to observe the microstructure of Type-A and Type-B nanomaterials. Figure 52 shows the images of Type-A nanomaterial, whose specific heat capacity was marginally enhanced for both solid phase and liquid phase (2 ~ 31 %). Figure 53 shows the microstructure of Type-B nanomaterial, which showed the anomalous enhancement of the specific heat capacity for the liquid phase (87 ~ 106 %). It was observed in Figure 53 that special needle-shaped micron-scale structures formed within the nanomaterial. These needle-like structures are only observed for Type-B nanomaterial samples and are expected to be responsible for the anomalously enhanced values of the specific heat capacity of Type-B nanomaterial, especially for the liquid phase data (nanofluid). Furthermore, TEM analysis was performed to verify whether or not the nanoparticles were agglomerated during the repeated melting and solidification in the DSC.

Figure 54 shows the TEM image of the nanomaterial after the subjecting the samples to repeated (12 times) melting and solidification for the thermal cycling protocol implemented in the DSC. On observing the samples in the electron microscope after subjecting them to thermal cycling - it was observed that the nanoparticles were not agglomerated and yet remained well dispersed. The nominal size of the MgO nanoparticles is ~ 20 nm.

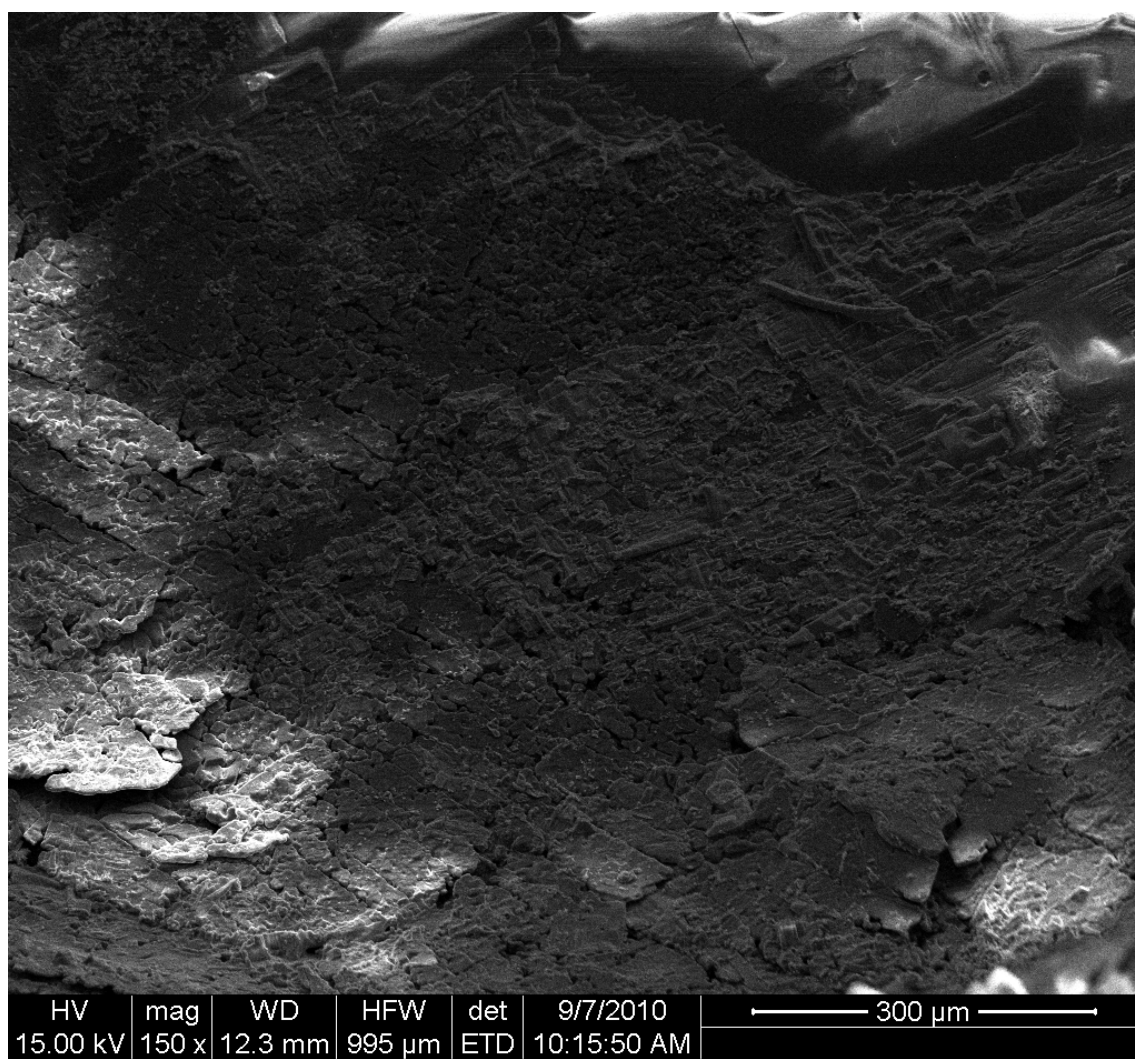


Figure 52. SEM images of Type-A MgO/ Li_2CO_3 - K_2CO_3 nanomaterial (coarse powder samples).

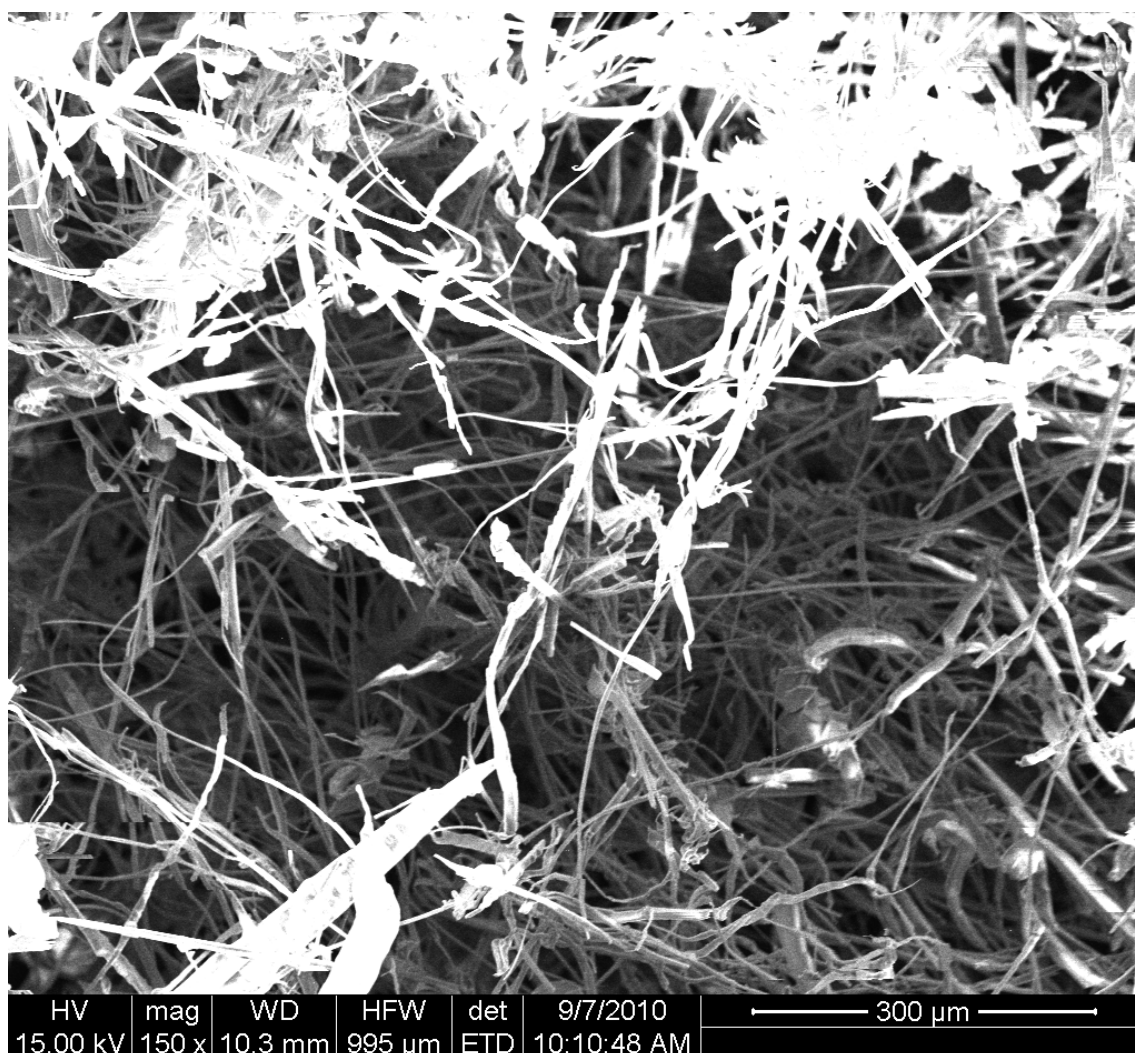


Figure 53. SEM images of Type-B samples of $\text{MgO}/\text{Li}_2\text{CO}_3\text{-K}_2\text{CO}_3$ nanomaterial (fine powder samples), which showed the anomalously enhanced specific heat capacity for the liquid phase. It was observed that the molten salt eutectic formed an interconnected network of needle-shaped micron-scale sub-structures (percolation network). This percolation network is expected to be responsible for the anomalous enhancement of the specific heat capacity of Type-B nanomaterial (nanofluid) samples.

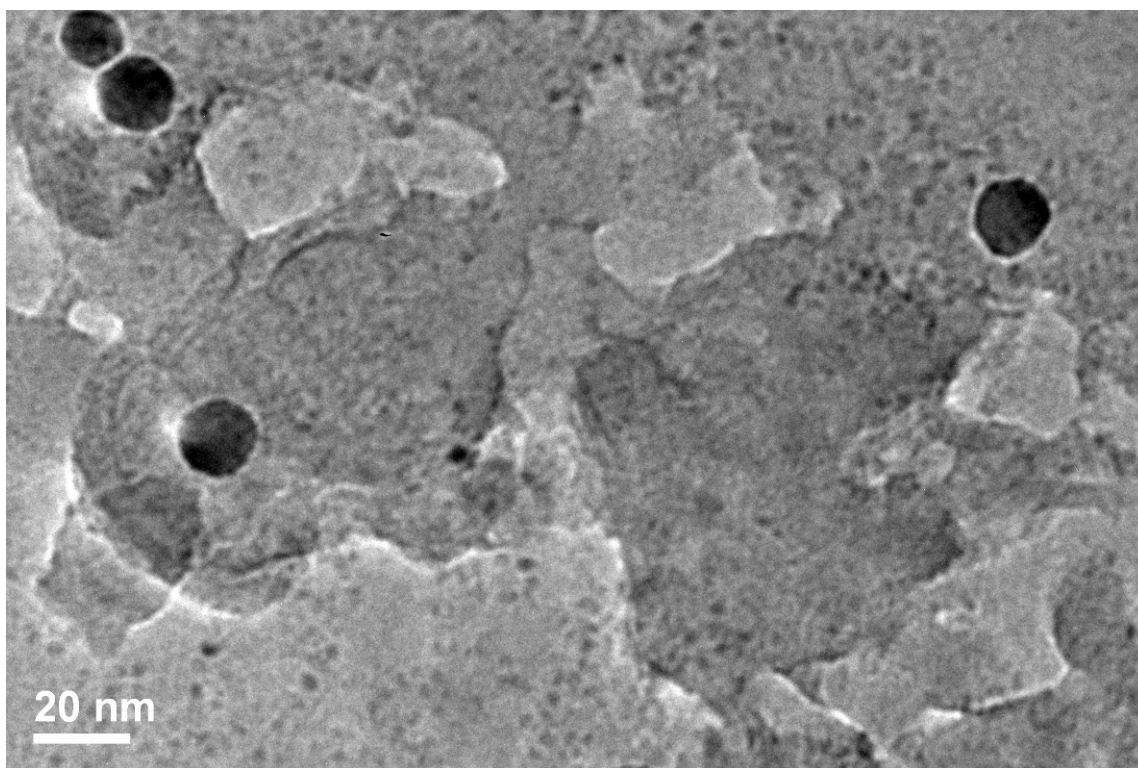


Figure 54. Transmission Electron Microscopy (TEM) image of MgO nanoparticles in the Type-B samples of $\text{MgO}/\text{Li}_2\text{CO}_3\text{-K}_2\text{CO}_3$ nanomaterial after thermal cycling in the DSC. It is observed that the nanoparticles were not agglomerated and the nominal size of the nanoparticles is ~ 20 nm.

5.7.3 Al_2O_3 / Li_2CO_3 - K_2CO_3 nanomaterial

Molten salt (Li_2CO_3 - K_2CO_3)-based Al_2O_3 nanomaterial was synthesized by the same liquid solution method as before (i.e., SiO_2 and MgO nanomaterials). Similar to the previous experiments, two distinct amorphous powders were observed to form after the drying process was completed by evaporation of water from the ultrasonicated aqueous salt solution with the dispersed nanoparticles (Figure 55). Approximately half of the petri-dish was covered by very coarse amorphous powder (“Type-A nanomaterial”) and the rest was covered by fine amorphous powder (“Type-B nanomaterial”). Due to the low water solubility of the alumina nanoparticles, the nanoparticles were separated and agglomerated at the end of the evaporation process, resulting in coarse amorphous powder. In contrast, the fine amorphous powder seems to have minimal agglomeration of the nanoparticles and they were also observed to be uniformly dispersed in the dried samples of the salt solution.

5.7.3.1 Specific heat capacity results

Two samples of Type-A nanomaterials and four samples of Type-B nanomaterials were synthesized and tested separately for measuring their specific heat capacity. The results are shown in Figures 56-57 and in Tables 26-29. Figure 56 shows the variation of specific heat capacity with temperature for Type-A and Type-B

nanocomposite (solid phase) samples. The peak at ~ 500 °C is the melting peak of the base eutectic (488 °C).

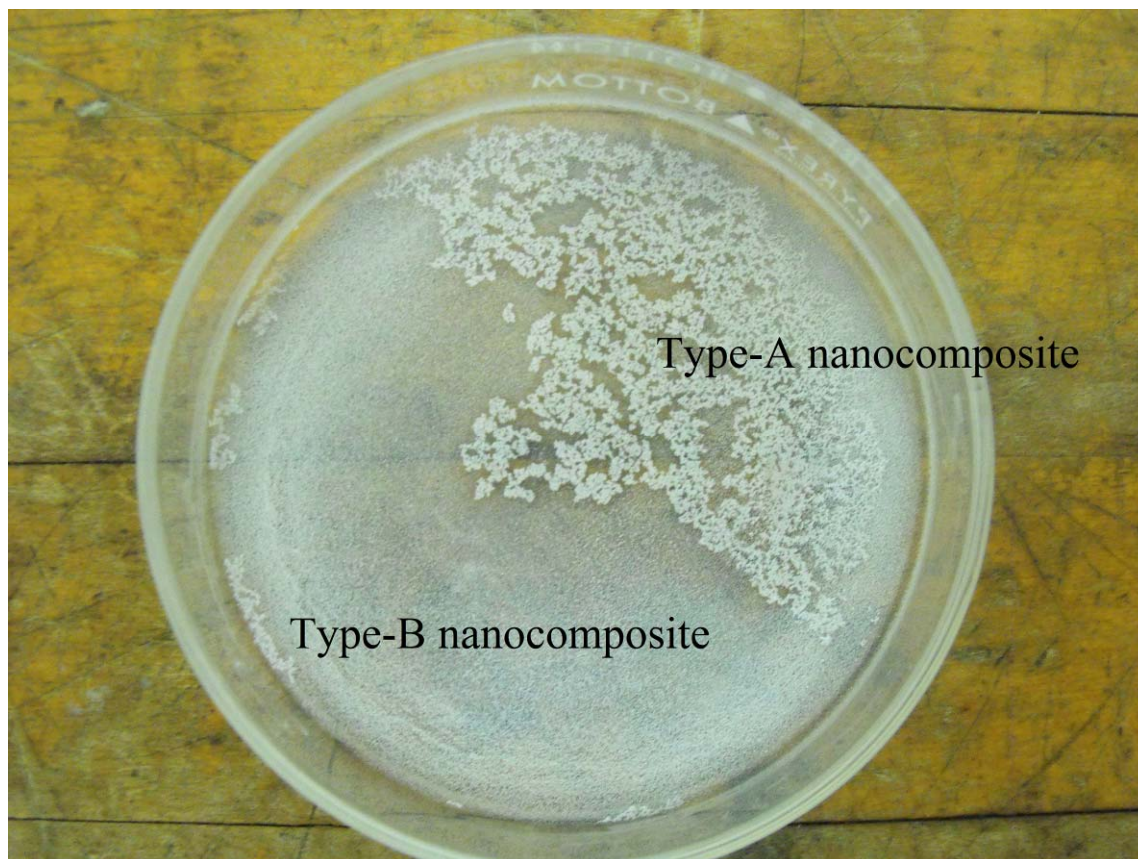


Figure 55. Image of dry amorphous powder of $\text{Al}_2\text{O}_3/\text{Li}_2\text{CO}_3\text{-K}_2\text{CO}_3$ (1.0 wt%) nanomaterial after the evaporation was completed. The image shows coarse amorphous powder (Type-A) and fine amorphous powder (Type-B).

Tables 26-27 lists the average specific heat capacity of Type-A and Type-B nanocomposite samples that were measured for the temperature range of 355 °C - 455 °C. The average specific heat capacity of Type-A nanocomposites and Type-B nanocomposites did not show any significant variation and were enhanced marginally (8 % ~ 37 %) compared with that of the pure eutectic. (The measurement uncertainty is 2.7 ~ 4.3 %). Figure 57 shows the variation of specific heat capacity with temperature for Type-A and Type-B nanofluids (liquid phase). The average specific heat capacity of Type-A and Type-B nanofluids for the temperature range of 525 °C - 555 °C are listed in Tables 28 - 29. In contrast to the solid phase (nanocomposite) data, the average specific heat capacity of Type-B nanofluids was enhanced by 101 ~ 119 % (compared to that of the eutectic salt), while the average specific heat capacity of Type-A nanofluids was enhanced by only 14 ~ 19 % (compared to that of the eutectic salt). The measurement uncertainty is 2.3 % ~ 7.6 %.

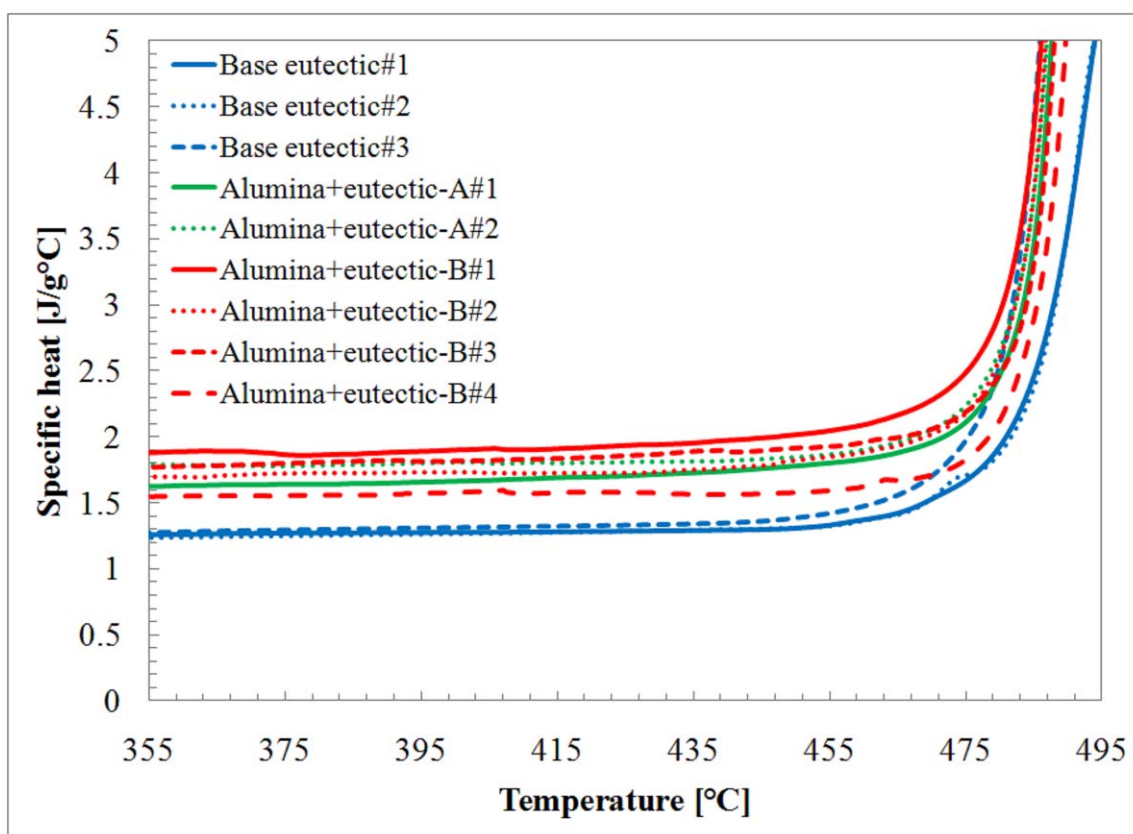


Figure 56. Variation of the specific heat capacity with temperature (355 °C ~ 495 °C) for $\text{Al}_2\text{O}_3/\text{Li}_2\text{CO}_3\text{-K}_2\text{CO}_3$ nanocomposites. The average specific heat capacity of both nanocomposites were enhanced by 8~37 % over the pure molten salt eutectic.

Table 26. Specific heat capacity measurements (J /g-K) of Type-A $\text{Al}_2\text{O}_3/\text{Li}_2\text{CO}_3\text{-K}_2\text{CO}_3$ nanocomposites, which are obtained from the coarse powders of eutectics containing agglomerated nanoparticles. (ε : standard deviation for all the thermo-cycle data for a sample).

C_p (J/g-K)	Pure Eutectic	Nano-composite Type-A (#1)	Nano-composite Type-A (#2)
1 st run	1.351	1.556	1.547
2 nd run	1.334	1.487	1.576
3 rd run	1.264	1.610	1.651
4 th run	1.229	1.577	1.692
5 th run		1.631	1.736
6 th run		1.458	1.610
7 th run		1.359	1.588
8 th run		1.612	1.347
9 th run		1.413	1.577
10 th run		1.066	1.569
11 th run		1.068	1.364
12 th run		0.967	1.148
Average	1.294	1.401	1.534
ε	0.060	0.237	0.167

Table 27. Specific heat capacity measurements (J /g-K) of Type-B $\text{Al}_2\text{O}_3/\text{Li}_2\text{CO}_3\text{-K}_2\text{CO}_3$ nanocomposites, that are obtained from fine amorphous powders of eutectics that contain uniformly dispersed nanoparticles with no (or minimal) agglomeration. (ϵ : standard deviations for all the thermo-cycle data for a given sample).

C_p (J/g-K)	Pure Eutectic	Type-B (#1)	Type-B (#2)	Type-B (#3)	Type-B (#4)
1 st run	1.351	1.698	1.464	1.459	1.410
2 nd run	1.334	1.741	1.628	1.571	1.422
3 rd run	1.264	1.824	1.750	1.621	1.436
4 th run	1.229	1.812	1.825	1.663	1.437
5 th run				1.729	1.432
6 th run				1.726	1.445
7 th run				1.767	1.436
8 th run				1.757	1.448
9 th run				1.766	1.459
10 th run				1.728	1.443
11 th run				1.727	1.437
12 th run				1.742	1.393
Average	1.294			1.688	1.433
ϵ	0.060	0.060	0.158	0.094	0.018

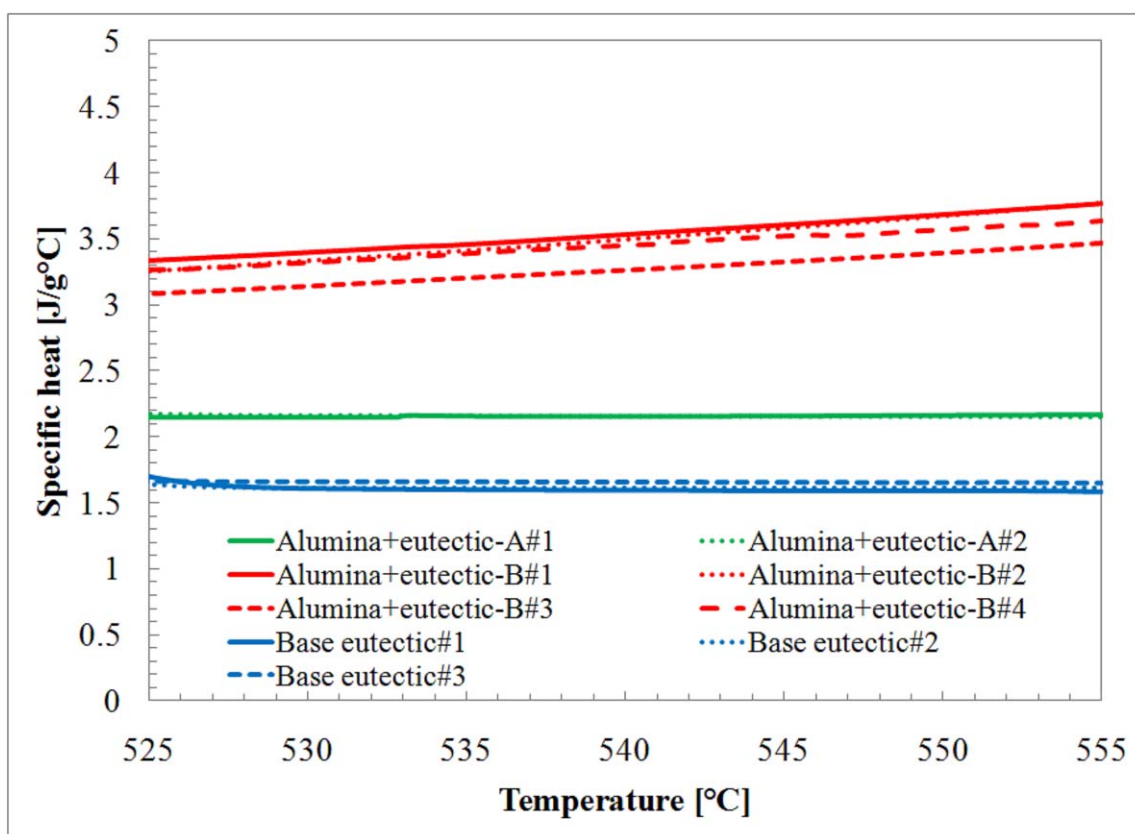


Figure 57. Variation of specific heat capacity with temperature (525 °C ~ 555 °C) for $\text{Al}_2\text{O}_3/\text{Li}_2\text{CO}_3\text{-K}_2\text{CO}_3$ nanofluids.

Table 28. Specific heat capacity measurements (J /g-K) of Type-A $\text{Al}_2\text{O}_3/\text{Li}_2\text{CO}_3\text{-K}_2\text{CO}_3$ nanofluids, which were obtained from the coarse powders of eutectics containing agglomerated nanoparticles. (ε : standard deviation for all the thermo-cycle data for a sample).

C_p (J/g-K)	Pure Eutectic	Nanofluid-A (#1)	Nanofluid-A (#2)
1 st run	1.692	2.239	2.122
2 nd run	1.674	2.135	2.111
3 rd run	1.581	2.230	2.197
4 th run	1.533	2.175	2.210
5 th run		2.163	2.234
6 th run		1.983	2.066
7 th run		1.821	2.023
8 th run		2.117	1.640
9 th run		1.809	1.797
10 th run		1.238	1.880
11 th run		1.204	1.578
12 th run		1.015	1.289
Average	1.620	1.844	1.929
ε	0.079	0.443	0.298

Table 29. Specific heat capacity measurements (J /g-K) of Type-B $\text{Al}_2\text{O}_3/\text{Li}_2\text{CO}_3\text{-K}_2\text{CO}_3$ nanofluids, that are obtained from fine amorphous powders of eutectics that contain uniformly dispersed nanoparticles with no (or minimal) agglomeration. (ε : standard deviations for all the thermo-cycle data for a given sample).

C_p (J/g-K)	Pure Eutectic	Nanofluid-B (#1)	Nanofluid-B (#2)	Nanofluid-B (#2)	Nanofluid-B (#4)
1 st run	1.692	3.509	3.335	3.224	3.441
2 nd run	1.674	3.544	3.466	3.261	3.471
3 rd run	1.581	3.565	3.579	3.263	3.465
4 th run	1.533	3.553	3.652	3.288	3.498
5 th run				3.291	3.457
6 th run				3.298	3.399
7 th run				3.290	3.421
8 th run				3.300	3.446
9 th run				3.302	3.428
10 th run				3.210	3.398
11 th run				3.167	3.331
12 th run				3.160	3.262
Average	1.620			3.254	3.418
ε	0.079	0.024	0.139	0.052	0.065

5.7.3.2 SEM / TEM analysis

SEM analyses were performed to observe the microstructure of Type-A and Type-B nanomaterials (Figure 58 and Figure 59). Characterization of the fine powders (Type-B) subsequently by SEM showed the existence of peculiar nanostructures (thread shaped nanostructures). However, the threadlike nanostructures were not observed in the coarse powder samples (Type-A). The fine grained amorphous eutectic powder (Type-B) was analyzed using transmission electron microscopy (TEM, Jeol JEM-2010). Figure 60 shows TEM image of Type-B nanomaterial powders after repeated melting/solidification (thermo-cycling) in the DSC. Figure 61 shows a representative TEM image of type-B powders after repeated thermo-cycling experiments - where no significant agglomeration of the individual nanoparticles was observed. Figure 61 shows that thread shaped nanostructures are formed in the bulk phase of the eutectic mixture – where each threadlike nanostructure has a diameter of 100 ~ 200 nm and the alumina nanoparticles are uniformly dispersed at the intersection of these threadlike nano-structures. From the SEM and TEM images it is apparent that the groups of the nanoparticles are located at the junction of the threadlike nano-structures. The nano-particles are found to be in the size range of 1~20 nm, with the size distribution of the nanoparticles being preferentially weighted in the range of 1~2 nm.

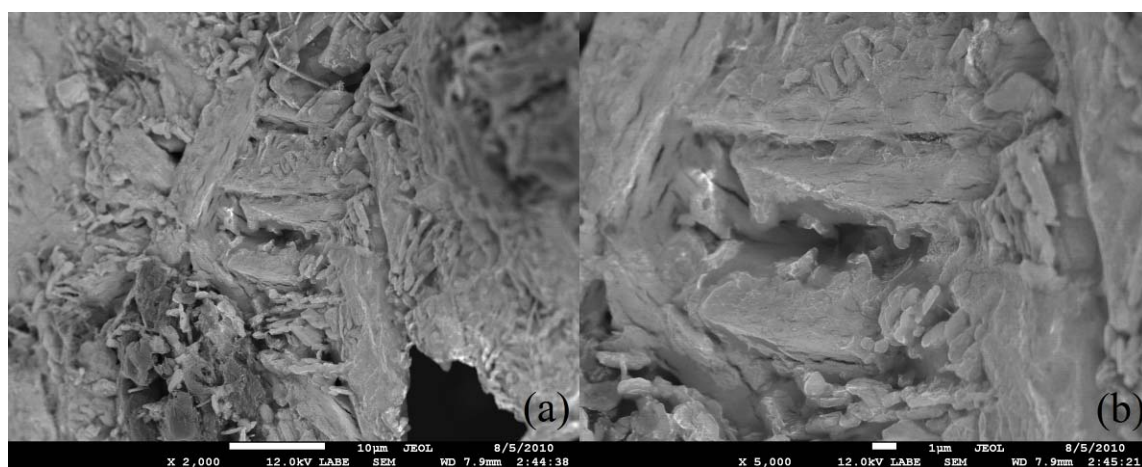


Figure 58. SEM images of Type-A $\text{Al}_2\text{O}_3/\text{Li}_2\text{CO}_3\text{-K}_2\text{CO}_3$ nanomaterial (coarse powder samples).

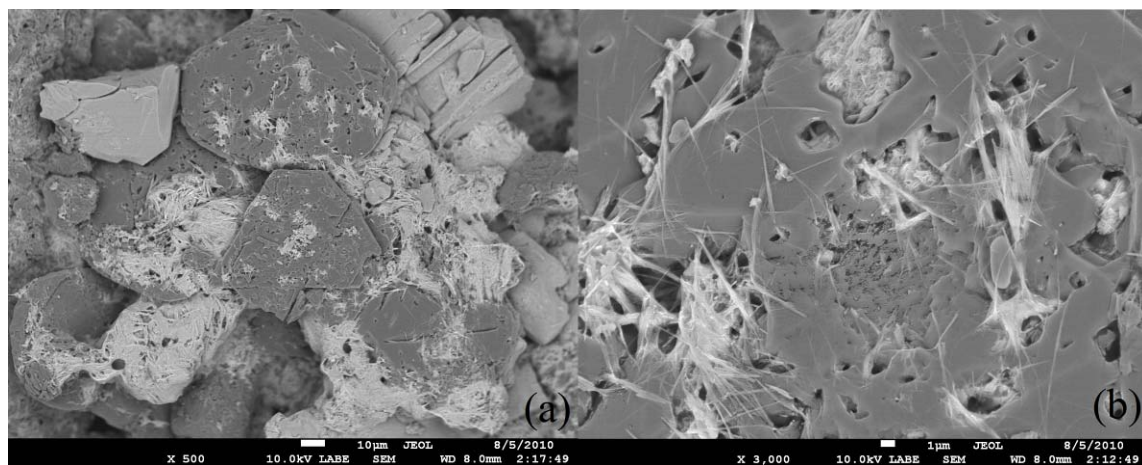


Figure 59. SEM images of Type-B $\text{Al}_2\text{O}_3/\text{Li}_2\text{CO}_3\text{-K}_2\text{CO}_3$ nanomaterial (coarse powder samples) showing nanoparticles with no (or minimal) agglomeration. Special threadlike nano-structures were observed.

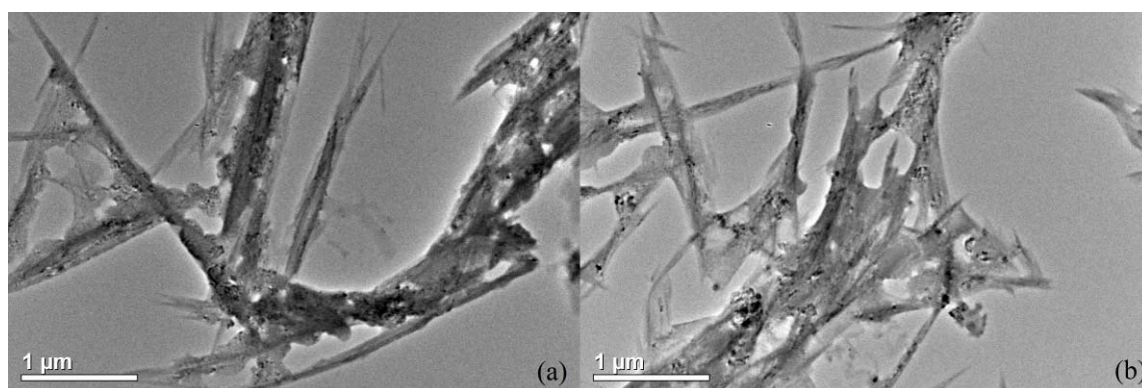


Figure 60. TEM images of Type-B $\text{Al}_2\text{O}_3/\text{Li}_2\text{CO}_3\text{-K}_2\text{CO}_3$ powders showing the formation of thread shaped nanostructures. The alumina nanoparticles were observed to be located at the intersection of the thread shaped nanostructures.

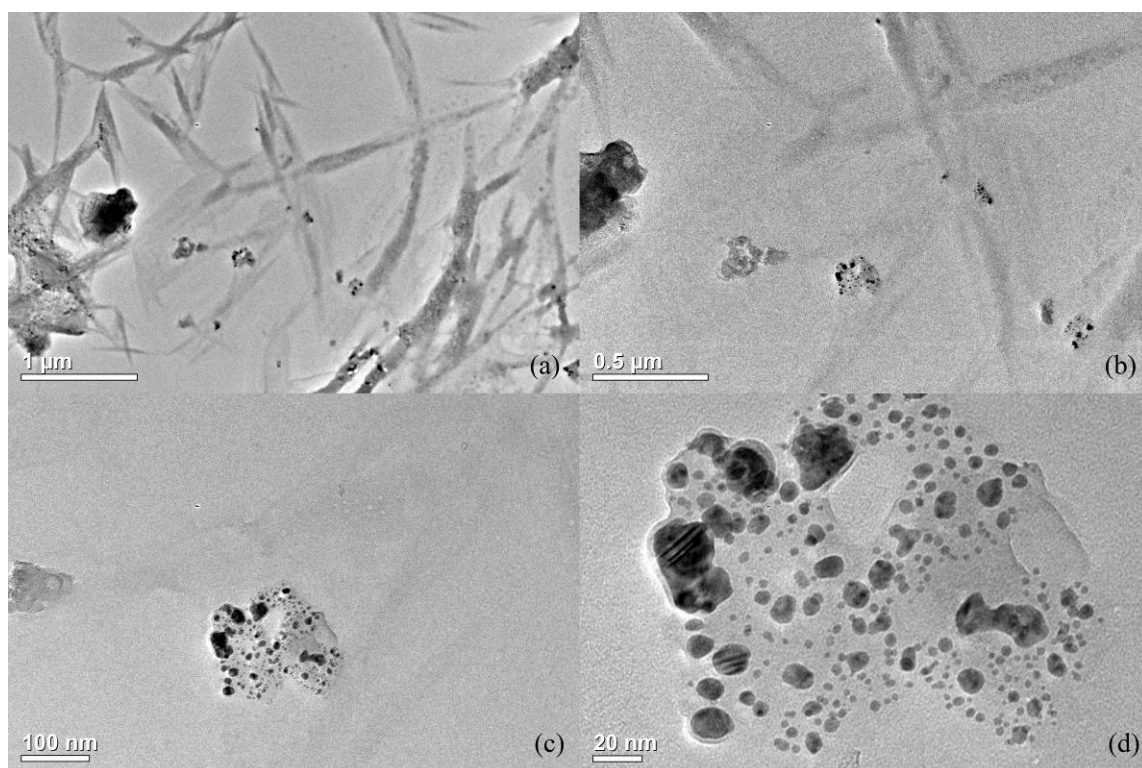


Figure 61. High resolution TEM images of the thread shaped nanostructures. It was observed that a group of alumina nanoparticles are located at the intersection of the thread shaped nano-structures. The group of nanoparticles therefore seems to induce the nucleation and germination of the threadlike nanostructures that mutually interconnect with each other. It was also observed that nanoparticles are not agglomerated and the nominal size of the nanoparticle is 1~20 nm.

5.7.4 ICP analysis

To verify the composition of the nanomaterials after the synthesis procedure (separation method), inductively coupled plasma mass spectrometry (ICP-MS) was performed. ICP-MS was performed to verify any change in the composition of the molten salt samples during the synthesis procedure involving the separation method. This step was necessary to investigate the large enhancements in the specific heat capacity of Type-B nanomaterials. For this test, two samples were synthesized by mixing Al_2O_3 nanoparticles (at mass concentration of 1%) with Li_2CO_3 - K_2CO_3 eutectic salts (62:38 by molar ratio) using the separation method to obtain the Type-A (coarse powder) and Type-B (fine powder) nanomaterials.

The samples were then prepared for testing on ICP-MS platform using different solvents (nitric acid and de-ionized water). Table 30 shows ICP test results of Type-A nanomaterials and Type-B nanomaterials. It was observed that the molten salt composition of Type-B nanomaterials, which showed very large enhancement in specific heat capacity at liquid phase ($\sim 120\%$), has higher content of Li_2CO_3 (73:27 Li_2CO_3 : K_2CO_3 by molar ratio) compared with that of the Type-A nanomaterials.

Based on the previous measurements of the specific heat capacity of the pure molten salt materials (Figure 25), the base line for comparison of the specific heat capacity of Type-B nanomaterials should be ~ 2.8 J/g-K. This implies that the large specific heat capacity enhancement of Type-B nanomaterials results from a combined effect of: (a) change in chemical composition of the molten salt (i.e., higher baseline for

the specific heat capacity of the molten salt material); and (b) existence of special sub-structure (percolation network) that is induced by the high surface area of the uniformly dispersed nanoparticles that are not agglomerated (or have minimal amount of agglomeration).

Table 30. ICP test results for Type-A nanomaterials and Type-B nanomaterials. SiO₂ nanoparticles at 1% mass concentration in molten salt of Li₂CO₃:K₂CO₃ (by molar ratio).

	ICP-MS (acid method)	ICP-MS (DIW method)
Type-A	64:36	63:37
Type-B	73:27	74:26

5.7.5 New specific heat capacity model (Equation 15)

This following section is a speculative exercise in trying to ascertain the source of the anomalous enhancements in specific heat capacity measured for some of the nanomaterials used in this study. In the section 5.3.2., specific heat capacity of special sub-structure was estimated using Equation 15 and imaging analysis. The same analysis was performed in this section to estimate the properties of special sub-structure in Type-

B nanomaterials. Similar to exercise performed in section 5.3.2., the density of the special sub-structure is assumed to be ~ 2.2 g/cc, which is the density of the base material at solid phase. The volume fraction of the special sub-structure was analytically estimated by digital image analyses. The SEM images of the nanomaterials were converted to binary images. The area fraction of the special sub-structure was calculated using histogram analyses of the pixels in the binary images. Figure 62 to 64 show the SEM images, the binary images, the histograms of the three carbonate eutectic-based nanofluids (silica, magnesia, and alumina). Based on the image analyses, the volume fraction of the special sub-structure for each nanofluid was computed. The volume fraction of the silica nanofluid, the magnesia nanofluid, and the alumina nanofluid is calculated to be 40.5 %, 28.9 %, and 35.6 %, respectively. Using the value of V_c in the new model (equation 15), the prediction of specific heat capacity of special sub-structure was obtained and shown in Table 31. Since ICP test showed the specific heat capacity of molten salt eutectic was changed during the separation method, the specific heat capacity of the micron-scale sub-structure (percolation network) was also corrected using the new values (or corrected values) of the specific heat capacity for the molten salt with the changed composition. Table 31 shows the estimated values for the specific heat capacity of the micron-scale sub-structures (percolation network) by using Equation 15. The result shows that the specific heat capacity of the sub-structure (percolation network) was 6.2~6.5 J/g-K without C_p correction (i.e., assuming the molten salt had the same composition as the eutectic composition of for base molten salt with the molar ratio of to be equal to 62:38). After correcting for the change in the composition of the molten

salt composition to that obtained by ICP-MS analyses, the value of the specific heat capacity of the sub-structure (percolation network) was estimated to be 3.8~4.1 J/gK (after C_p correction accounting for the change in chemical composition of the molten salt, cf. Table 30).

The observed enhancement in the specific heat capacity may result from another mechanism or a combination of the proposed model and alternate material transport mechanisms which are currently unknown (which can be the topic of future studies).

Table 31. Estimated specific heat capacity of the micron-scale sub-structures (percolation network) based on image analysis and using Equation 15.

	C_p (uncorrected)	C_p (corrected)
$\text{SiO}_2/\text{Li}_2\text{CO}_3\text{-K}_2\text{CO}_3$	6.5 J/gK	4.0 J/gK
$\text{MgO}/\text{Li}_2\text{CO}_3\text{-K}_2\text{CO}_3$	6.5 J/gK	3.8 J/gK
$\text{Al}_2\text{O}_3/\text{Li}_2\text{CO}_3\text{-K}_2\text{CO}_3$	6.2 J/gK	4.1 J/gK

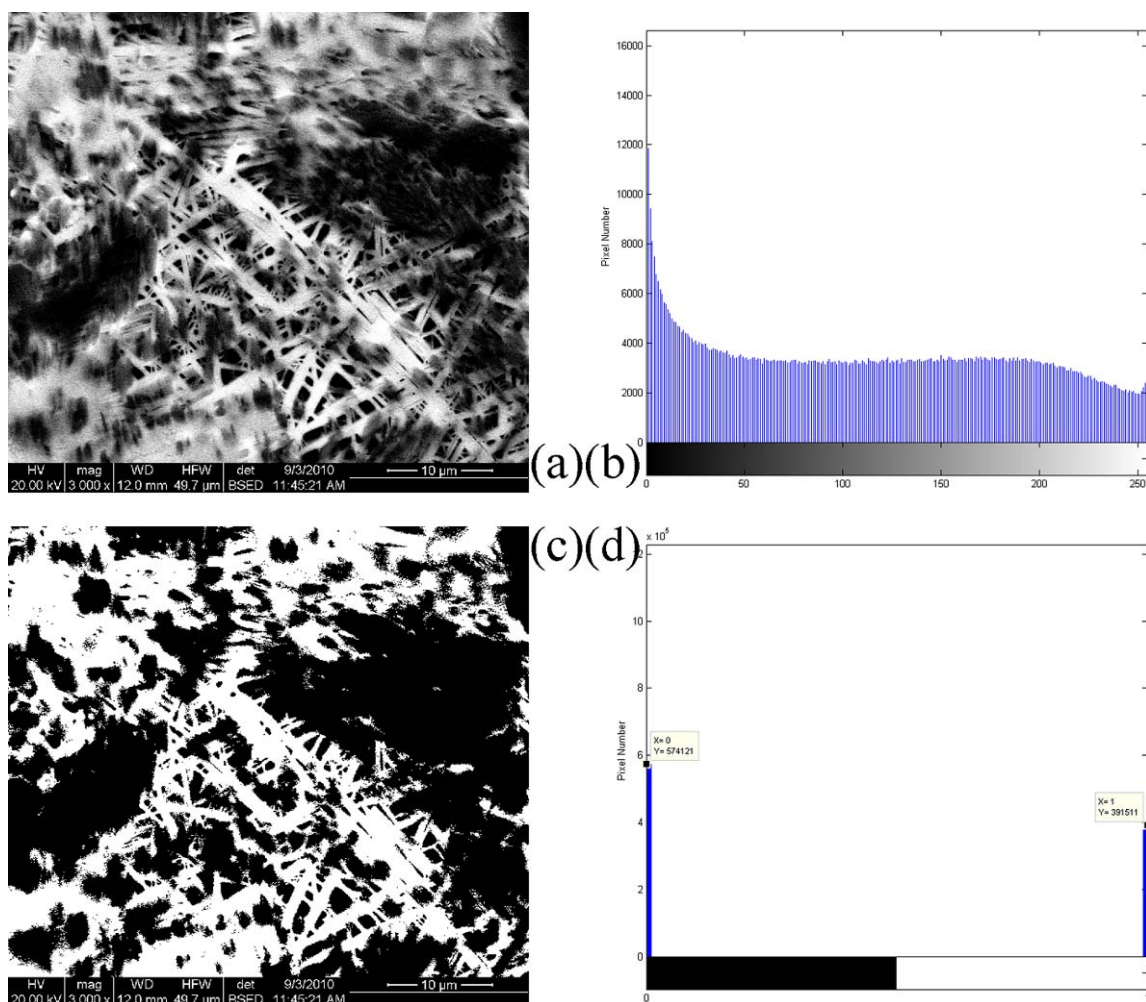


Figure 62. (a) SEM image of $\text{SiO}_2/\text{Li}_2\text{CO}_3\text{-K}_2\text{CO}_3$ nanomaterial. (b) Histogram plot of the pixel intensities obtained from the SEM image (a). (c) Binary image of the SEM image after setting a threshold intensity of 128. (d) Histogram plot of the binary image after image processing in (c). Based on the image histogram plot, 40.5 % of the image area is covered by the brighter pixels of the woven structures.

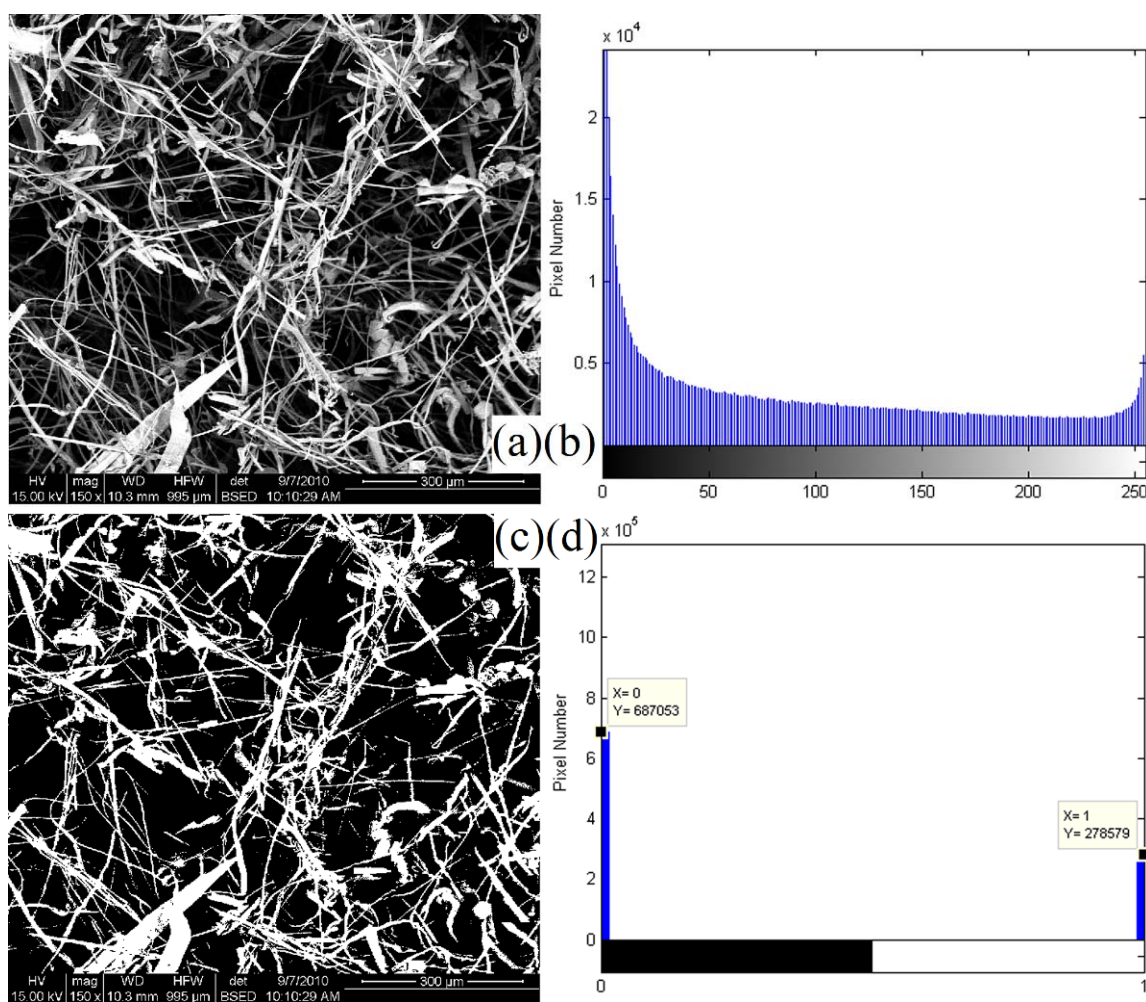


Figure 63. (a) SEM image of $\text{MgO/Li}_2\text{CO}_3\text{-K}_2\text{CO}_3$ nanomaterial. (b) Histogram plot of the pixel intensities obtained from the SEM image (a). (c) Binary image of the SEM image after setting a threshold intensity of 128. (d) Histogram plot of the binary image after image processing in (c). Based on the image histogram plot, 28.9 % of the image area is covered by the brighter pixels of the woven structures.

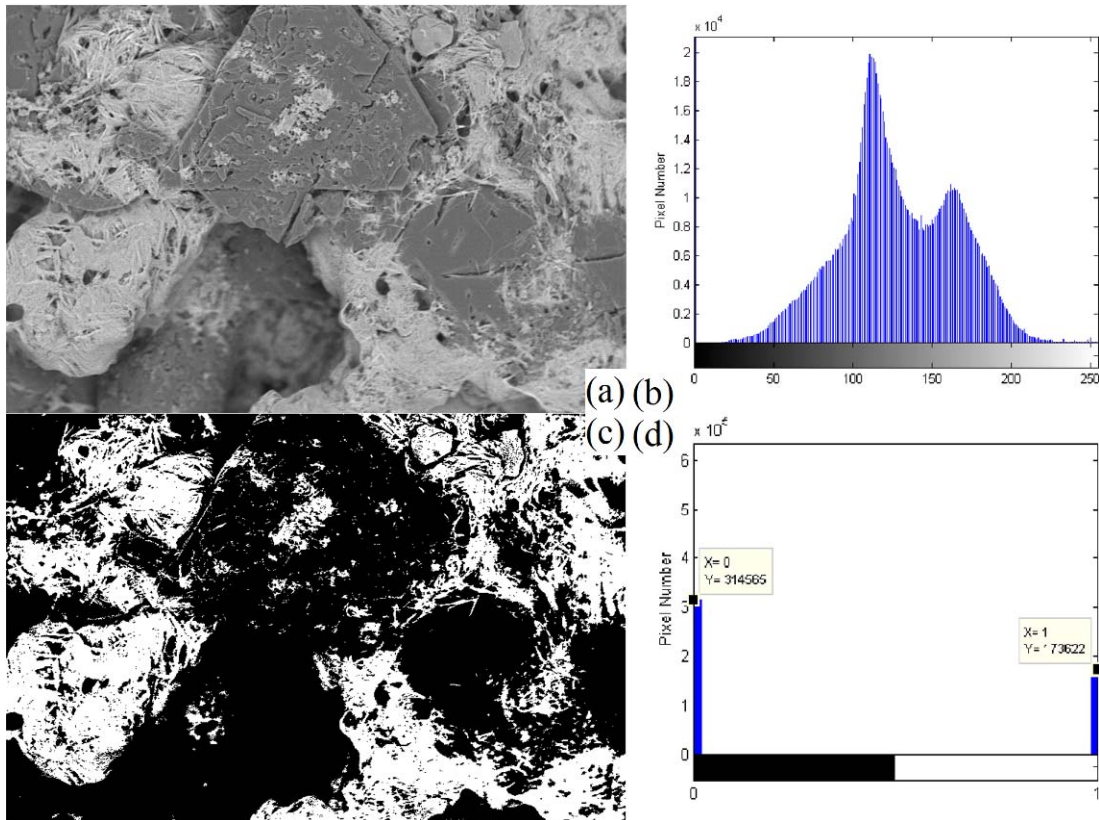


Figure 64. (a) SEM image of $\text{Al}_2\text{O}_3/\text{Li}_2\text{CO}_3\text{-K}_2\text{CO}_3$ nanomaterial. (b) Histogram plot of the pixel intensities obtained from the SEM image (a). (c) Binary image of the SEM image after setting a threshold intensity of 128. (d) Histogram plot of the binary image after image processing in (c). Based on the image histogram plot, 35.6 % of the image area is covered by the brighter pixels of the woven structures.

6. CONCLUSIONS

High-temperature nanomaterials were explored in order to enhance their thermal conductivity and the specific heat capacity for thermal-energy storage (TES) applications, particularly for concentrated solar power (CSP) platforms. In the computational simulations performed in this study, the lower bound (or optimal size) for the size of the nanoparticle was explored, since existing data in literature shows that the size of the nanoparticle in the nanofluid affects the enhancement of the thermal conductivity of the nanofluid. The effect of the carbon nanotube size and temperature on the interfacial thermal resistance and the lower bound of the size of the nano-particles were explored in this study for high temperature eutectic nanofluids, since these values are not available in the literature. Molecular Dynamics (MD) simulations were employed to calculate the interfacial thermal resistance between single walled carbon nanotube and eutectic of lithium carbonate and potassium carbonate (62:38 molar ratios). The interfacial thermal resistance between the CNT and the PCM was estimated to be $4.65 \times 10^{-8} \text{ m}^2\text{K/W}$. The lower bound of the size of the nanotube obtained in this study ranges from 60 nm to 78 nm, for an average temperature range spanning from 1050 K to 1200 K. In reality, some amount of agglomeration of the CNT is expected in the nanofluid. Hence, in designing the nanofluid, the size of the CNT should be selected to be in the range of 10~40 nm, such that the size of the agglomerated CNT cluster is expected to be ~70 nm.

Moreover, the computational models predicted the spatial variation of density of the solvent phase in the vicinity of the nanoparticles. This arises from the formation of a semi-solid “layer of the solvent material” due to ordering material of liquid molecules on a crystalline surface. It was observed that the thickness of the semi-solid layer of the liquid molecules is not affected by the size of the nanoparticles. Hence, the results from this study can be extended to estimating the interfacial thermal resistance between multi-walled carbon nanotubes and eutectic molecules, as well.

In experimental studies, two molten salt nanomaterials (nanocomposites and nanofluids) were synthesized and their specific heat capacity was measured using a differential scanning calorimeter (DSC) instrument. Initially, the eutectic of Li_2CO_3 - K_2CO_3 (62:38 by molar ratio) and eutectic of BaCl_2 - NaCl - CaCl_2 - LiCl (15.9:20.5:34.5:29.1 by molar ratio) were chosen as the solvents for synthesizing the nanomaterials. The silica nanoparticles were dispersed in these eutectic salts. The specific heat capacity measurements were performed using standardized (ASTM) thermo-cycling protocol that was implemented in the DSC instrument. The nanomaterial composed of SiO_2 nanoparticles in BaCl_2 - NaCl - CaCl_2 - LiCl eutectic (mass concentration of 1.0 %) showed 6 ~ 7 % enhancement for the solid phase and 13 ~ 16 % enhancement for the liquid phase. The nanomaterial composed of SiO_2 nanoparticle in Li_2CO_3 - K_2CO_3 eutectic (mass concentration of 1.0 %) showed 15 ~ 19 % enhancement for the solid phase and 19 ~ 26 % enhancement for the liquid phase. Since the specific heat capacity of the molten salt (Li_2CO_3 : K_2CO_3) can be classified to have three distinct values (low C_p region, transition region, and high C_p region) when the chemical composition of the

molten salt is changed. Hence, the effect of the change in chemical composition on the properties of the nanomaterials was also investigated in this study. The results show that the specific heat capacity enhancement was only observed for nanomaterials whose molten salt compositions (62:38 and 70:30 by molar ratio) are closer to that of the transition region (66:34 by molar ratio).

On the other hand, nanomaterials whose molten salt compositions (46:54, 54:46, and 78:22 by molar ratio), are distinctly different from that of the transition region (66:34 by molar ratio), did not show any significant enhancement in specific heat capacity. In these cases the measured values of the specific heat capacity were in good agreement with the predictions from the conventional specific heat capacity model (or “simple mixing model”, Equation 14).

SEM analyses showed that the nanomaterials, whose specific heat capacity did not change, had significant amounts of agglomerated nanoparticles. Hence these salt samples did not show any enhancement in the specific heat capacity.

On the other hand, the nanomaterial samples, whose specific heat capacity were enhanced, were observed from electron microscopy images to contain micron-scale sub-structures (percolation network) that were interconnected at the location of the nanoparticles. The nanoparticles in these samples, in turn, were found to be well dispersed with no (or minimal) agglomeration. The predictions for the specific heat capacity values by the conventional simple mixing model (Model 1, Equation 14) failed to predict the enhancement in the specific heat capacity for these nanomaterial samples. These micron-scale structures (percolation networks) that appear to form interconnected

network with neighboring nanoparticles are expected to play a very important role in enhancing the thermo-physical properties of the nanomaterials and are also expected to have a different chemical composition compared to that of the pure eutectic salts.

In a speculative exercise, it was assumed that the modified structure of molten salts has higher specific heat capacity than the eutectic and therefore to contribute a significant proportion to the enhancement of the specific heat capacity observed for the nanomaterials. Hence, a new model was derived by accounting for the contributions from the modified structure of molten salt that is nucleated in the solvent due to the presence of the nanoparticles.

Furthermore, the thermal diffusivity of the molten salt nanomaterial was measured experimentally. Eutectic of $\text{Li}_2\text{CO}_3\text{-K}_2\text{CO}_3$ was chosen as the base material and SiO_2 nanoparticles were dispersed at 1 % mass concentration. Due to the limitation of the operating temperature of the measurement instrument (LFA), only the solid phase thermal conductivity was measured in this study. From the measurements, the thermal conductivity of the nanocomposite was estimated to be enhanced by 37 ~ 47 % compared with that of the pure eutectic salt. The conventional thermal conductivity models (Hamilton-Crosser & Maxwell-Garnett [47,58]) failed to predict the enhancement in the thermal conductivity values. Similar to the specific heat capacity measurements, it is expected that the interconnected micron-scale sub-structures (percolation network) contributes to the enhancement in thermal conductivity values of the nanocomposite samples.

In addition, a new nanomaterial synthesis method (separation method) was developed in this study. This method results in the separation of the synthesized nanomaterial into powders of two distinct morphologies (Type-A and Type-B nanomaterials). Type-A nanomaterials (coarse powders) showed almost no enhancement in specific heat capacity, while Type-B nanomaterials (fine powders) showed significant enhancement in the specific heat capacity values, especially for the liquid phase. ICP analysis was performed to analyze material composition of each nanomaterial sample and the results showed that, in the new synthesis method, the nanoparticles induced changes in the chemical composition of each nanomaterial. Based on the change in chemical composition of the molten salts in which the nanoparticles were dispersed, the addition of nanoparticles was found to enhance the specific heat capacity by $\sim 20\%$. This is consistent with the measurements performed for the eutectic salt nanomaterials and the level of enhancements observed in these experiments.

These results can have significant impact for CSP applications. Using the nanomaterials as TES or HTF in CSP will decrease the amount of the material requirement and the size of TES platforms. This will also enable the operating temperature of the TES/ CSP units to be elevated to higher temperatures enabling higher thermodynamic efficiencies to be achieved. Preliminary calculations show that the enhancement of the specific heat capacity of the nanofluids by $25\% \sim 100\%$ (as shown in this study) can lead to a reduction in the cost of the solar thermal power generated by TES/ CSP units to be reduced by as much as $20\% \sim 50\%$. This conclusion is derived from cost-models and results previously reported in the literature [59, 60].

REFERENCES

- [1] Dincer, I., 2000, "Renew Energy and Sustainable Development: A Crucial Review," *Renew. Sust. Energy Rev.*, **4**, pp. 157–175.
- [2] Koroneos, C., Spachos, T., and Moussiopoulos, N., 2003, "Exergy Analysis of Renewable Energy Sources," *Renewable Energy*, **28**(2), pp. 295-310.
- [3] Janz, G.J., Allen, C.B., Bansal, N.P., Murphy, R.M., Tomkins, R.P.T., 1979, *Physical Properties Data Compilations Relevant to Energy Storage, II. Molten Salts: Data on Single and Multi-component Systems*, US Govt. Print. Off., Washington, DC.
- [4] Kearney, D., Herrmann, U., Nava, P., Kelly, B., Mahoney, R., and Pacheco, J., 2003, "Assessment of A Molten Salt Heat Transfer Fluid in A Parabolic Trough Solar Field," *ASME Journal of Solar Energy and Engineering*, **125**, pp. 170–176.
- [5] Araki, N., Matsuura, M., Makino, A., Hirata, T., and Kato, Y., 1988, "Measurement of Thermophysical Properties of Molten Salts: Mixtures of Alkaline Carbonate Salts", *Int. J. Thermophys.*, **9**, pp. 1071-1080.
- [6] Choi, S., 1995, *Enhancing Thermal Conductivity of Fluids With Nanoparticles*, D.A. Siginer, H.P. Wang (Eds.), *Developments and Applications of Non-Newtonian Flows*, ASME, FED-231/MD-66, pp. 99–105.
- [7] Song, Y.S., and Youn, J.R., 2005, "Influence of Dispersion States of Carbon Nanotubes on Physical Properties of Epoxy Nanocomposites," *Carbon*, **43**, pp. 1378-1385.

- [8] Haggemueller, R., Guthy, C., Lukes, J.R., Fischer, J.E., and Winey, K.I., 2007, "Single Wall Carbon Nanotube / Polyethylene Nanocomposites: Thermal and Electrical Conductivity," *Macromolecules*, **40**, pp. 2417-2421.
- [9] Wang, J., Xie, H., Xin, Z., Li, Y., and Chen, L., 2010, "Enhancing Thermal Conductivity of Palmitic Acid Based Phase Change Materials with Carbon Nanotubes as Fillers," *Solar Energy*, **84**, pp. 339-344.
- [10] Lee, S., Choi, S. U. S., Li, S., and Eastman, J. A., 1999, "Measuring Thermal Conductivity of Fluids Containing Oxide Nanoparticles," *Journal of Heat Transfer*, **121**, pp. 280–289.
- [11] Xie, H., Wang, J., Xi, T., and Liu, Y., 2002, "Thermal Conductivity of Suspensions Containing Nanosized SIC Particles," *International Journal of Thermophysics*, **23**(2), pp. 571–580.
- [12] Das, S.K., Putta, N., Thiesen, P., and Roetzel, W., 2003, "Temperature Dependence of Thermal Conductivity Enhancement for Nanofluids," *ASME Trans. J. Heat Transfer*, **125**, pp. 567–574.
- [13] Xuan, Y., and Li, Q., 2000, "Heat Transfer Enhancement of Nanofluids," *International Journal of Heat and Fluid Transfer*, **21**, pp. 58–64.
- [14] Patel, H.E., Das, S.K., Sundararagan, T., Nair, A.S., Geoge, B., and Pradeep, T., 2003, "Thermal Conductivities of Naked And Monolayer Protected Metal Nanoparticle Based Nanofluids: Manifestation of Anomalous Enhancement and Chemical Effects," *Applied Physics Letters*, **83**, pp. 2931–2933.

- [15] Wang, X., Xu, X., and Choi, S. U. S., 1999, "Thermal Conductivity of Nanoparticle–Fluid Mixture," *Journal of Thermophysics and Heat Transfer*, **13**(4), pp. 474–480.
- [16] Hong, T.-K., Yang, H.-S., and Choi, C.J., 2005, "Study of The Enhanced Thermal Conductivity of Fe Nanofluids," *Journal of Applied Physics*, **97**(6), pp. 1–4.
- [17] Eastman, J.A., Choi, S.U.S., Li, S., Yu, W., and Thompson, L.J., 2001, "Anomalous Increased Effective Thermal Conductivities of Ethylene Glycol-Based Nanofluids Containing Copper Nanoparticles," *Applied Physics Letters*, **78**(6), pp. 718–720.
- [18] Keblinski, P., Phillpot, S.R., Choi, S.U.S., and Eastman, J.A., 2002, "Mechanisms of Heat Flow in Suspensions of Nano-Sized Particles (Nanofluids)," *International Journal of Heat and Mass Transfer*, **45**, pp. 855–863.
- [19] Jang, S.P., and Choi, S.U.S., 2004, "Role of Brownian Motion in The Enhanced Thermal Conductivity of Nanofluids," *Applied Physics Letters*, **84**, pp. 4316–4318.
- [20] Prasher, R., Bhattacharya, P., and Phelan, P.E., 2005, "Thermal Conductivity of Nanoscale Colloidal Solutions (Nanofluids)," *Physical Review Letters*, **94**(2), pp. 025901.
- [21] Prasher, R., Bhattacharya, P., and Phelan, P.E., 2006, "Brownian-Motion-Based Convective-Conductive Model for The Effective Thermal Conductivity of Nanofluids," *ASME J. Heat Transfer*, **128**, pp. 588–595.
- [22] Singh, N., Shin, D., and Banerjee, D., 2010, "Nano-Scale Effects in Multi-Phase Flows and Heat Transfer" (Book Chapter), in *MEMS and Nanotechnologies: From*

Science-to-Electronic Systems, to be published by Bentham Science Publishers (Sep. 2010), Editor: Kaul, A.B. (Affiliation: Jet Propulsion Lab., Pasadena, CA).

[23] Wen, D. and Ding, Y., 2004, “Effective Thermal Conductivity of Aqueous Suspensions of Carbon Nanotubes (Carbon Nanotube Nanofluids),” *Journal of Thermophysics and Heat Transfer*, **18**, pp. 481–485.

[24] Chon, C.H., Kim, K.D., Lee, S.P., and Choi, S.U.S., 2005, “Empirical Correlation Finding The Role of Temperature and Particle Size for Nanofluid (Al_2O_3) Thermal Conductivity Enhancement,” *Appl. Phys. Lett.*, **87**, pp. 153107.

[25] Choi, S.U.S., Zhang, Z.G., Yu, W., Lockwood, F.E., and Grulke, E.A., 2001, “Anomalous Thermal Conductivity Enhancement in Nanotube Suspensions,” *Applied Physics Letters*, **79**, pp. 2252–2254.

[26] Xie, H., Lee, H., Youn, W., and Choi, M., 2003, “Nanofluids Containing Multiwalled Carbon Nanotubes and Their Enhanced Thermal Conductivities,” *Journal of Applied Physics*, **94**, pp. 4967–4971.

[27] Assael, M.J., Chen, C.F., Metaxa, I.N., and Wakeham, W.A., 2004, “Thermal Conductivity of Suspensions of Carbon Nanotubes in Water,” *International Journal of Thermophysics*, **25**, pp. 971–985.

[28] Assael, M.J., Metaxa, I.N., Arvanitidis, J., Christofilos, D., and Lioutas, C., 2005, “Thermal Conductivity Enhancement in Aqueous Suspensions of Carbon Multi-Walled and Double-Walled Nanotubes in The Presence of Two Different Dispersants,” *International Journal of Thermophysics*, **26**, pp. 647–664.

- [29] Evans, W., Prasher, R., Fish, J., Meakin, P., Phelan, P., and Keblinski, P., 2008, "Effect of Aggregation and Interfacial Thermal Resistance on Thermal Conductivity of Nanocomposites and Colloidal Nanofluids," *Int. J. Heat Mass Transfer*, **51**, pp. 1431–1438.
- [30] Keblinski, P., Prasher, R., and Eapen, J., 2008, "Thermal Conductance of Nanofluids: is The Controversy Over?," *Journal of Nanoparticle Research*, **10**(7), pp. 1089–1097.
- [31] Zhou, S.Q., and Ni, R., 2008, "Measurement of The Specific Heat Capacity of Water-Based Al_2O_3 Nanofluid," *Appl. Phys. Lett.*, **92**, pp. 093123.
- [32] Namburu, P.K., Kulkarni, D.P., Dandekar, A., and Das, D.K., 2007, "Experimental Investigation of Viscosity and Specific Heat and Silicon Dioxide Nanofluids," *Micro Nano Lett.*, **2**, pp. 67–71.
- [33] Vajjha, R.S., and Das, D.K., 2009, "Specific Heat Measurement of Three Nanofluids and Development of New Correlations," *ASME J. Heat Transfer*, **131**, pp. 071601.
- [34] Nelson, I. C., Banerjee, D., and Ponnappan, R., 2009, "Flow Loop Experiments Using Polyalphaolefin," *J. Thermophys. Heat Transfer*, **23**, pp. 752–761.
- [35] Shin, D., and Banerjee, D., 2010, "Effects of Silica Nanoparticles on Enhancing Eutectic Carbonate Salt Specific Heat (Work in Progress)," *The International Journal of Structural Changes in Solids*, **2**(2), pp. 25-31.
- [36] Shin, D., and Banerjee, D., 2011, "Enhanced Specific Heat of SiO_2 Nanofluid," *Journal of Heat Transfer*, **133**(2), pp. 024501.

- [37] Shin, D., and Banerjee, D, 2011, "Enhancement of Specific Heat Capacity of High-Temperature Silica-Nanofluids Synthesized in Alkali Chloride Salt Eutectics for Solar Thermal-Energy Storage Applications," *International Journal of Heat and Mass Transfer*, **54**(5-6), pp. 1064-1070.
- [38] Shin, D., Jo, B., Kwak, H., and Banerjee, D., 2010, "Investigation of High Temperature Nanofluids for Solar Thermal Power Conversion and Storage Applications," *Proceedings of International Heat Transfer Conference*, ASME, August 8-13, Washington D.C., USA.
- [39] Swartz, E.T., and Pohl, R.O., 1989, "Thermal Boundary Resistance," *Rev. Mod. Phys.*, **61**, pp. 605–668.
- [40] Allen, M.P., and Tildesley, D.J., 1987, *Computer Simulations of Liquids*, Clarendon Press, Oxford.
- [41] Maruyama, S., Igarashi, Y., Taniguchi, Y., and Shibuta, Y., 2004, "Molecular Dynamics Simulations of Heat Transfer Issues in Carbon Nanotubes," in: *The 1st International Symposium on Micro & Nano Technology Honolulu, Hawaii, USA*.
- [42] Shenogin, S., Xue, L., Ozisik, R., Keblinski, P., and Cahill, D.G., 2004, "Role of Thermal Boundary Resistance on The Heat Flow in Carbon-Nanotube Composites," *Journal of Applied Physics*, **95**(12), pp. 8136–8144.
- [43] Huxtable, S.T., Cahill, D.G., Shenogin, S., Xue, L., Ozisik, R., Barone, P., Usrey, M., Strano, M.S., Siddons, G., Shim, M., and Keblinski, P., 2003, "Interfacial Heat Flow in Carbon Nanotube Suspensions," *Nature of Materials*, **2**(11), pp. 731–734.

- [44] Costa, M.F., 2008, "Molecular Dynamics of Molten $\text{Li}_2\text{CO}_3\text{--K}_2\text{CO}_3$," *Journal of Molecular Liquids*, **138**, pp. 61-68.
- [45] Braybrook, A.L., Heywood, B.R., Jackson, R.A., and Pitt, K., 2002, "Parallel Computational and Experimental Studies of The Morphological Modification of Calcium Carbonate by Cobalt," *J. Cryst. Growth*, **243**, pp. 336– 344.
- [46] Hasselman, D.P.H., and Johnson, L.F., 1987, "Effective Thermal Conductivity of Composites with Interfacial Thermal Barrier Resistance," *J. Compos. Mater.* **21**, pp. 508–515.
- [47] Nan, C.-W., Birringer, R., Clarke, D.R., and Gleiter, H., 1997, "Effective Thermal Conductivity of Particulate Composites with Interfacial Thermal Resistance," *J. Appl. Phys.*, **81**, pp. 6692–6699.
- [48] Plimpton, S., 1995, "Fast Parallel Algorithms for Short-Range Molecular Dynamics," *J. Comp. Phys.*, **117**, pp. 1-19.
- [49] Tsuneyuki, S., Tsukada, M., Aoki, H., and Matsui, Y., 1988, "First-Principles Interatomic Potential of Silica Applied to Molecular Dynamics," *Physical Review Letters*, **61**, pp. 869-872.
- [50] Yu, W., and Choi, S.U.S., 2003, "The Role of Interfacial Layers in The Enhanced Thermal of Nanofluids: A Renovated Maxwell Model," *Journal of Nanoparticle Research*, **5**(1–2), pp. 167–171.
- [51] Lide, D.R., Ed. 2008, *CRC Handbook of Chemistry and Physics*, CRC Press Taylor & Francis Group: Boca Raton, FL.

- [52] Yu, C.-J., Richter, A.G., Datta, A., Durbin, M.K., and Dutta, P., 2000, "Molecular Layering in A Liquid on A Solid Substrate: An X-Ray Reflectivity Study," *Physica B: Condensed Matter*, **283**(1-3), pp. 27-31.
- [53] Oh, S.H., Kauffmann, Y., Scheu, C., Kaplan, W.D., and Rühle, M., 2005, "Ordered Liquid Aluminum at The Interface with Sapphire," *Science*, **310**, pp. 661–663.
- [54] Feibelman, P.J., 2010, "The First Wetting Layer on A Solid," *Physics Today*, **63**(2), pp. 34-39.
- [55] Ocko, B.M., Hlaing, H., Jepsen, P.N., Kewalramani, S., Tkachenko, A., Pontoni, D., Reichert, H., Deutsch, M., 2011, "Unifying Interfacial Self-Assembly and Surface Freezing," *Phys. Rev. Lett.*, **106**(13), pp. 137801.
- [56] Jung, S., Jo, B., Shin, D., and Banerjee, D., 2010, "Experimental Validation of A Simple Analytical Model for Specific Heat Capacity of Aqueous Nanofluids," *Proceedings of SAE 2010 Power Systems Conference*, SAE, November 2-4, Ft. Worth, Texas, USA.
- [57] Jung, S., and Banerjee, D., 2011, "A Simple Analytical Model for Specific Heat of Nanofluid with Tube Shaped and Disc Shaped Nanoparticles," *Proceedings of 8th Thermal Engineering Joint Conference*, ASME/JSME, March 13-17, Honolulu, Hawaii, USA.
- [58] Hamilton, R.L., and Crosser, O.K., 1962, "Thermal Conductivity of Heterogeneous Two-Component Systems," *I & EC Fundamentals*, **1**, pp. 187–191.

- [59] Malik, D., 2010, "Evaluation of Composite Alumina Nanoparticle and Nitrate Eutectic Materials for Use in Concentrating Solar Power Plants," MS Thesis, Texas A&M University, College Station, TX, USA.
- [60] Betts, M., 2011, "The Effects of Nanoparticle Augmentation of Nitrate Thermal Storage Materials for Use in Concentrating Solar Power Applications," MS Thesis, Texas A&M University, College Station, TX, USA.
- [61] Scientific Group Thermodata Europe, 2011, " K_2CO_3 - Li_2CO_3 ," http://www.sgte.org/fact/phase_diagram.php?file=K2CO3-Li2CO3.jpg&dir=FTsalt (accessed March 1, 2011).

APPENDIX A*

In this appendix A, the measurements obtained from the samples were related to the phase diagram reported in the literature. Figure 65 shows the phase diagram of molten salt ($\text{Li}_2\text{CO}_3\text{-K}_2\text{CO}_3$). According to the experimental results in this study, molten salt nanomaterials, whose molten salt compositions are 62 % and 70 % (Li_2CO_3 mol %), showed enhanced specific heat capacity (26 % and 12 %, respectively). According to the phase diagram (Figure 65), these samples form a solid + liquid region. Hence, samples with chemical composition of 61 % (Li_2CO_3 mol %) and the nanomaterial (whose molten salt composition is 70 %) have larger amount of solid Li_2CO_3 in the solid + liquid slurry that forms above the melting point. This indicates the modified structure in this nanomaterial will contain more Li_2CO_3 than the modified structure in another nanomaterial, whose composition is 62 mol %. It means that the modified structures formed in both cases will not have same chemical composition, structural shape, or thermo-physical properties. According to the experimental study in the section 5, it was shown in SEM images (Figures 21 and 38) that each modified structure has different shape (microstructure) and therefore the enhancements in specific heat capacity from these structures are not the same due to different size of the interfacial region between the modified structure and the bulk of the solvent phase. For the nanomaterial, whose composition is 62:38 (by molar ratio), the specific heat capacity was enhanced by ~

*Reprinted with permission from Centre for Research in Computational Thermochemistry (University of Montreal), Box 6079, Station Downtown Montreal, Quebec, CANADA [<http://www.factsage.com>].

25 %, and for the nanomaterials, whose composition is 70:30 (by molar ratio), the specific heat capacity was enhanced by 12 %. This may be due to difference in composition of the modified structure in each nanomaterial.

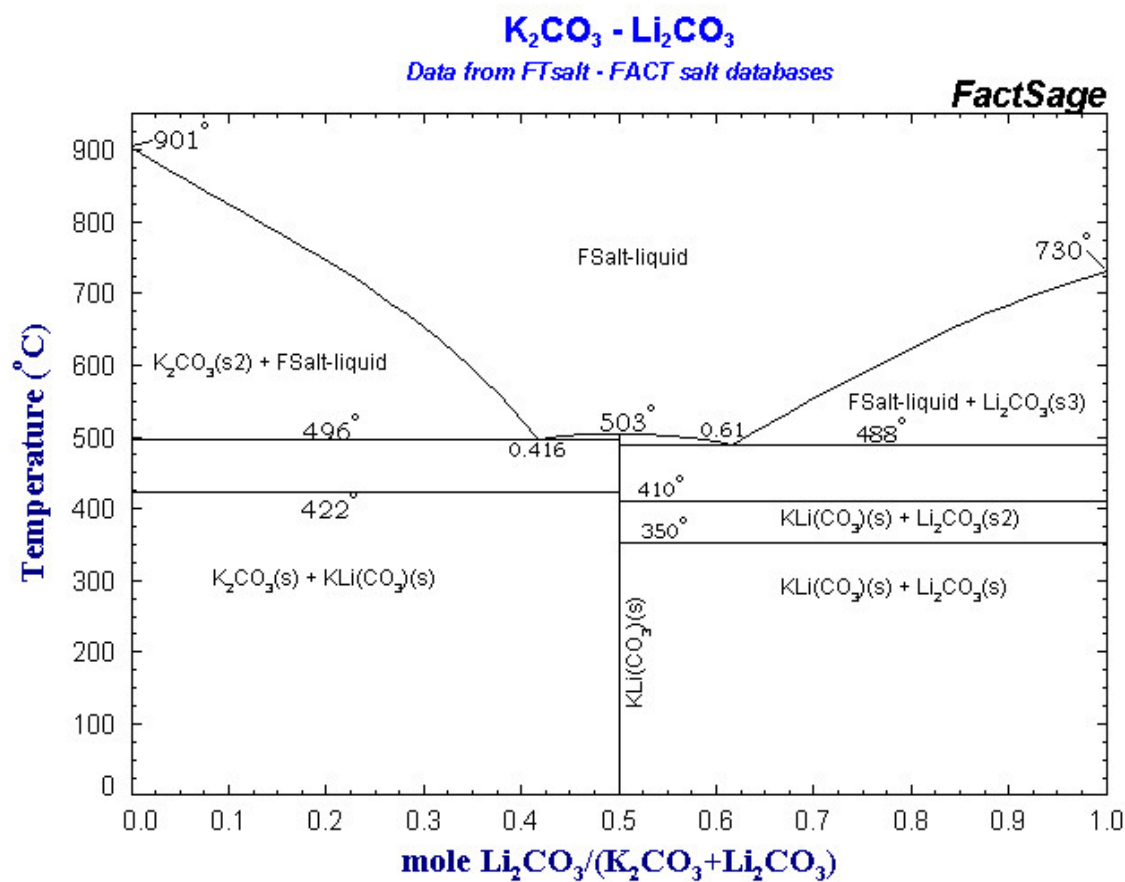


Figure 65. Phase diagram of molten salt (Li_2CO_3 - K_2CO_3) [61]

APPENDIX B

In this appendix B, experiments for nanomaterial samples, which did not demonstrate enhancement in specific heat capacity, are enhanced. According to section 5.4, three nanomaterial samples with salt compositions of 46:54, 54:46, and 78:22, did not show any enhancement in the specific heat capacity values.

Table 32 shows specific heat capacity values of molten salt samples and corresponding nanomaterial samples, for salt composition of 46:54 (by molar ratio). According to the results, no significant enhancement in specific heat capacity was observed. Figure 66 shows SEM images of the nanomaterial. It was observed that nanoparticles were significantly agglomerated.

Similarly, Table 33 shows specific heat capacity values of molten salt samples and the corresponding nanomaterial samples, whose salt composition is 54:46 (by molar ratio). According to the results, no significant enhancement in specific heat capacity was observed. Figure 67 shows SEM images of the nanomaterial. It was observed that nanoparticles were significantly agglomerated.

Table 34 shows specific heat capacity of molten salt samples and the corresponding nanomaterial samples, whose salt composition is 78:22 (by molar ratio). According to the results, no significant enhancement in specific heat capacity was observed. Figure 68 shows SEM images of the nanomaterial. It was observed that nanoparticles were significantly agglomerated.

Table 32. Specific heat capacity of molten salt and its nanomaterial, whose molten salt composition is 46:54 (by molar ratio).

C_p (J/g-K)	Solid salt	Nanocomposite	Liquid salt	Nanofluid
#1	1.245	1.202	1.778	1.600
#2	1.183	1.171	1.708	1.562
#3	1.091	1.158	1.647	1.554
#4	0.904	1.154	1.537	1.557
#5	1.099	1.003	1.262	1.304
#6	1.157	0.989	1.355	1.299
#7	1.138	1.014	1.340	1.328
#8	1.110	0.973	1.315	1.281
#9	1.369	-	1.726	-
#10	1.264	-	1.621	-
#11	1.192	-	1.564	-
#12	1.032	-	1.377	-
Average	1.149	1.083	1.572	1.436
Enhancement	-	-5.7 %	-	-5.5 %
ε	0.12	0.10	0.18	0.14

Table 33. Specific heat capacity of molten salt and its nanomaterial, whose molten salt composition is 54:46 (by molar ratio).

C_p (J/g-K)	Solid salt	Nanocomposite	Liquid salt	Nanofluid
#1	1.408	1.347	1.827	1.757
#2	1.363	1.350	1.760	1.744
#3	1.311	1.267	1.695	1.629
#4	1.145	1.155	1.500	1.502
#5	1.250	1.241	1.578	1.615
#6	1.195	1.291	1.516	1.678
#7	1.152	1.241	1.464	1.608
#8	1.112	1.198	1.420	1.550
#9	1.187	1.160	1.528	1.338
#10	1.150	1.158	1.487	1.334
#11	1.145	1.106	1.487	1.297
#12	1.196	1.126	1.562	1.325
Average	1.218	1.220	1.569	1.531
Enhancement	-	0 %	-	-2 %
ε	0.10	0.08	0.13	0.17

Table 34. Specific heat capacity of molten salt and its nanomaterial, whose molten salt composition is 78:22 (by molar ratio).

C_p (J/g-K)	Solid salt	Nanocomposite	Liquid salt	Nanofluid
#1	1.387	1.334	2.715	2.599
#2	1.425	1.350	2.752	2.638
#3	1.430	1.382	2.770	2.663
#4	1.433	1.404	2.790	2.691
#5	1.333	1.399	2.610	2.668
#6	1.350	1.399	2.645	2.673
#7	1.362	1.385	2.656	2.666
#8	1.342	1.386	2.628	2.670
Average	1.383	1.380	2.635	2.658
Enhancement	-	0 %	-	-1 %
ϵ	0.04	0.05	0.07	0.06

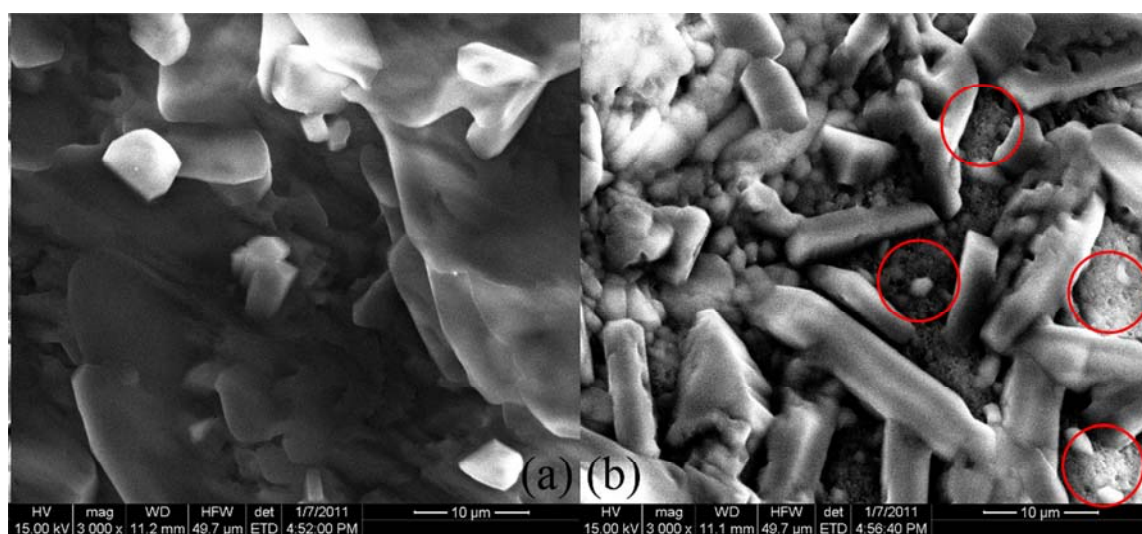


Figure 66. SEM image showing significant agglomeration of nanoparticles for salt composition of 46:54 (molar ratio) for $\text{Li}_2\text{CO}_3\text{:K}_2\text{CO}_3$.

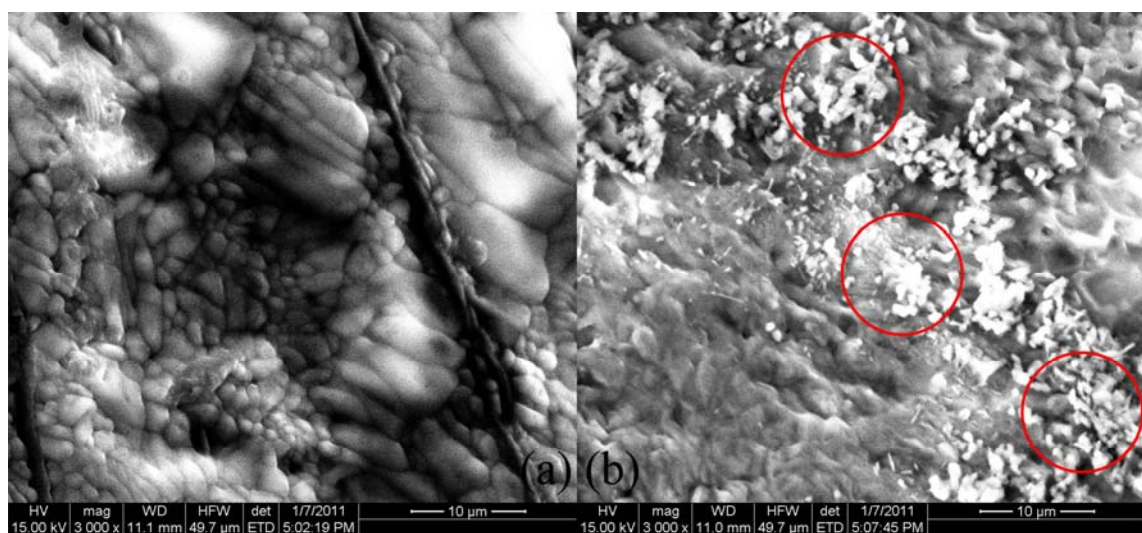


Figure 67. SEM image showing significant agglomeration of nanoparticles for salt composition of 54:46 (molar ratio) for $\text{Li}_2\text{CO}_3\text{:K}_2\text{CO}_3$.

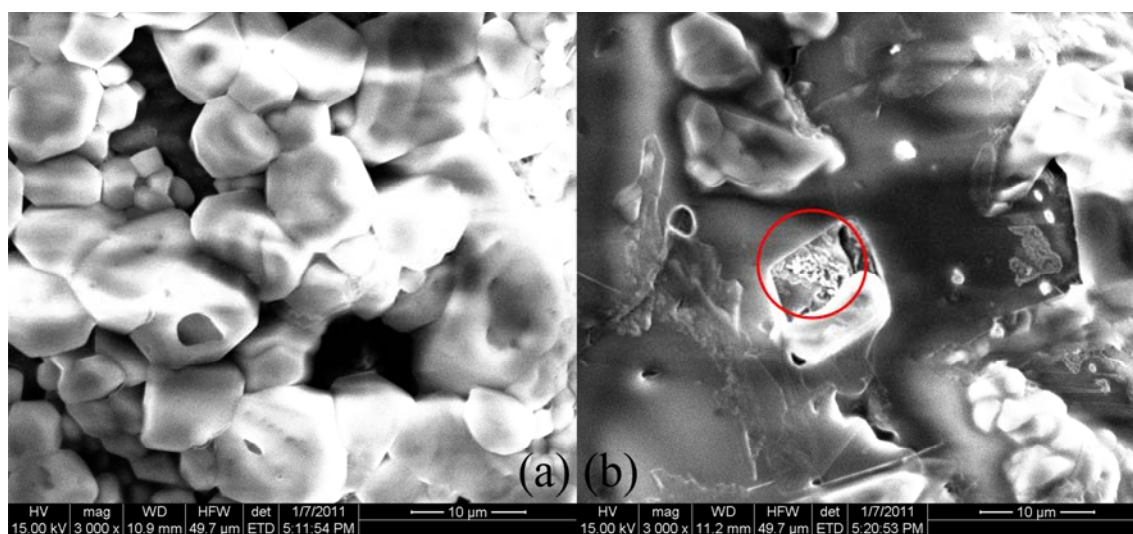


Figure 68. SEM image showing significant agglomeration of nanoparticles for salt composition of 78:22 (molar ratio) for $\text{Li}_2\text{CO}_3\text{:K}_2\text{CO}_3$.

From the specific heat capacity measurements and the material characterization analyses (Figures 66 ~ 68) above, it was concluded that all the nanomaterial samples, which did not show any enhancement in specific heat capacity, contain significant amounts of agglomerations of nanoparticles. This implies that the agglomerated nanoparticles failed to induce the distinct formation of the modified microstructure within the molten salts (with associated change in chemical composition and thermo-physical properties). Therefore, the specific heat capacity is not enhanced when nanoparticles agglomerate.

APPENDIX C

In this appendix C, T tests were performed to compare the specific heat capacity values of the pure molten salt samples and nanomaterial samples. Using a simple statistical analysis using MS-Excel, the P-values of molten salt and their nanomaterial data were obtained for the various salt compositions (46:54, 54:46, 62:38, 70:30, and 78:22) (Table 35). If a P-value is below 0.05, the data set is considered to be statistically significant and a P-value of 0.05 or greater implies there is no difference between two data sets. According to Table 35, the nanomaterials, whose specific heat capacity was enhanced, has P-values much lower than 0.05. This indicates the specific heat capacity of molten salt sample is significantly different from that of the nanomaterial sample. On the other hand, the nanomaterials, whose specific heat capacity did not change, has P-values greater than 0.05. This indicates that the values of specific heat capacity between the molten salt samples and the nanomaterial samples are not significantly different for these chemical compositions.

Table 35. P-values of each molten salt and its nanomaterial

Heat capacity	No enhanced			Enhanced	
Composition	46:54	54:46	78:22	62:38	70:30
P-value	0.0758192	0.3702811	0.2189305	0.0000056	0.0095844

APPENDIX D

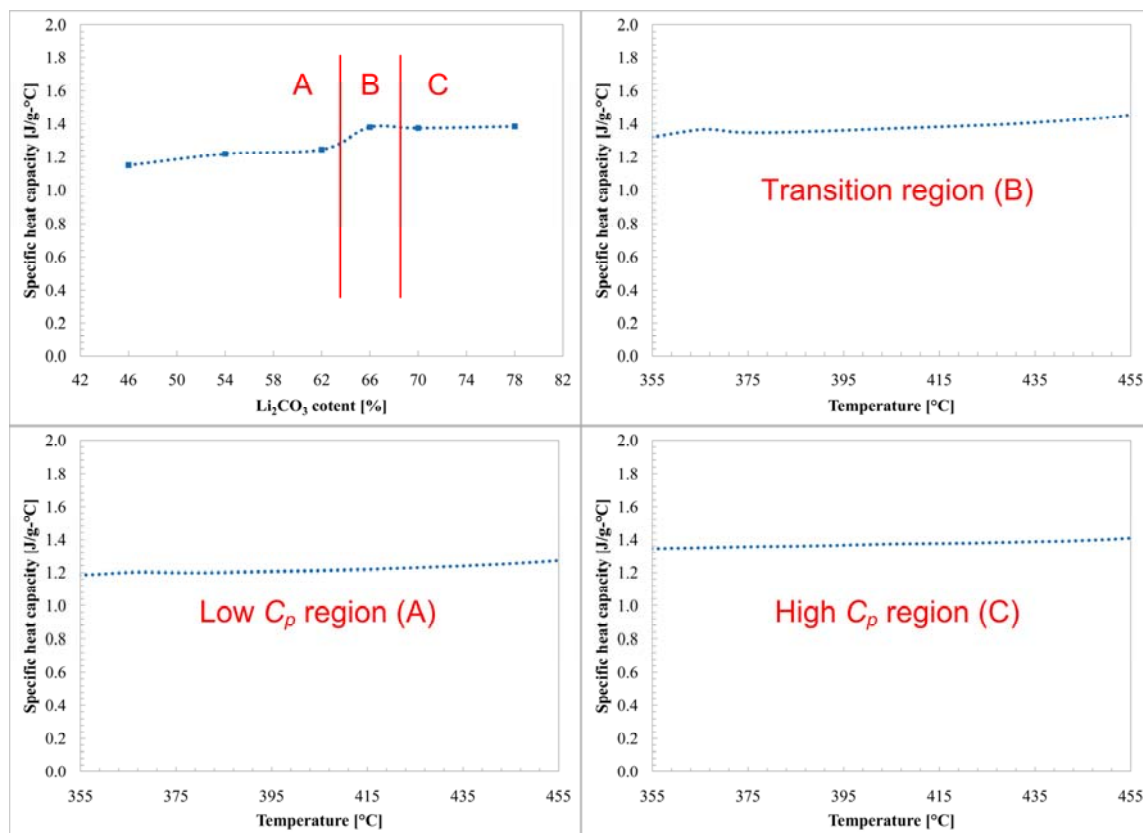


Figure 69. Specific heat capacity of molten salt at solid phase (Figure 25).

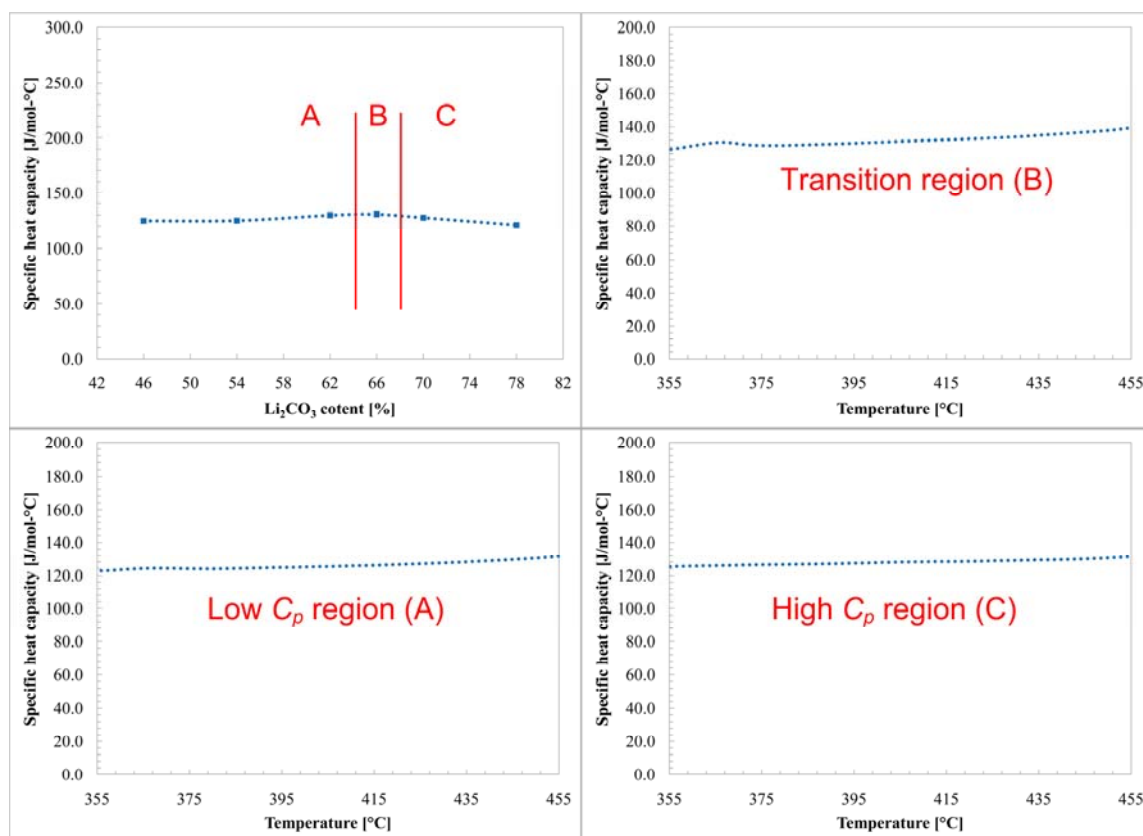


Figure 70. Molar specific heat capacity of molten salt at solid phase (Figure 26).

VITA

Name: Donghyun Shin

Address: Mechanical & Aerospace Engineering, Box 19018
University of Texas at Arlington
Arlington, TX 76019-0018

Email Address: shin@uta.edu

Education: B.S., Mechanical Engineering, Hanyang University, 2006
M.S., Mechanical Engineering, Ohio University, 2008
Ph.D., Mechanical Engineering, Texas A&M University, 2011